Abstract of "Photo-Patterning Studies for Liquid Crystal Alignment" by James N. Eakin, Ph.D., Brown University, May 2008.

This dissertation utilizes holographic exposure techniques to manipulate the periodic orientation of liquid crystal materials. Two different exposure techniques are investigated: a polarization holography interference method incident on a photo-responsive surface to induce a preferential ordering, and an amplitude holography interference method that relies on a phase separation and counter-diffusion reaction to create stratified regions of liquid crystal and polymer.

In the phase holography investigations, a linear photopolymerizable (LPP) layer is selectively polymerized permanently capturing phase information from the interference patterning and transferring it to align a liquid crystal material. The underlying periodic and frustrated alignment in the one- and two-dimensional alignment configurations is discussed, including the nature of their electro-optic switching transitions. A phenomenological model is presented to describe the Freedericksz transition, or lack thereof, for the registered planar-periodic boundary conditions resulting from the interference of two orthogonal circularly polarized beams.

In the amplitude holography investigations, the frustrated chiral and smectic ordering of ferroelectric liquid crystal domains encapsulated by a polymer binder were established. The refractive index modulation in these thin films is modelled as a phase grating that can be electrically addressed to erase the optical diffractive properties. A phenomenological model is developed to take into account a distribution of domain sizes and an effective field that stabilizes the ferroelectric liquid-crystal domains. A diffraction model successfully predicts changes in normalized intensities for first-order diffraction with applied field. These gratings demonstrate microsecond-scale response and relaxation times for various grating pitch sizes between ~ 3 and ~ 12 μm.

Photo-Patterning Studies for Liquid Crystal Alignment

by

James N. Eakin

B. S. Baldwin-Wallace College, 2001

Sc. M. Brown University, 2004

A dissertation submitted in partial fulfillment of the
requirements for the Degree of Doctor of Philosophy
in the Division of Engineering at Brown University

Providence, Rhode Island

May 2008

This dissertation by James N. Eakin is accepted in its present form by the Division of Engineering as satisfying the dissertation requirement for the degree of Doctor of Philosophy.

Date _____ _____
Gregory P. Crawford, Advisor

Recommended to the Graduate Council

Date _____ _____
Robert Hurt, Reader

Date _____ _____
Alexander Zaslavsky, Reader

Approved by the Graduate Council

Date _____ _____
Sheila Bonde
Dean of the Graduate School

Vita

James N. Eakin was born in Warren, Ohio on February 4, 1979. Upon completion of high school, he attended Baldwin-Wallace College and graduated in May 2001 with a B.S. in Physics, with minors in Chemistry and Mathematics. Shortly after graduation, James joined the Display & Photonics laboratory as a Research Assistant, advised by Professor Gregory Crawford. He completed the requirements for a Sc.M. in Engineering in 2004 at Brown with a Master's thesis titled: 'Electro-Optic Evaluation in Polarization Dependant Holographically Formed Polymer Dispersed Liquid Crystals.' During his tenure at Brown, James was an author or co-author on 27 publications and presented his work at conferences in Erice, Ischia, Taipei, Edinburgh, Ljubljana, San Diego, Seattle, Baltimore, San Francisco, Keystone, and Huntsville. James was also a visiting researcher at the University of Ljubljana (Slovenia) in the summer of 2003 and the Technical University of Eindhoven in the fall of 2003. His Ph.D. research was funded through a NASA GSRP fellowship from the Marshall Space Flight Center from 2004-2006, and was also awarded a SPIE educational scholarship to fund educational outreach projects and courses he co-developed.

Publications

1. B. Fan, S. D. Vartak, J. N. Eakin and S. M. Faris, "Broadband CLC polarizing films by photo-polymerization-induced phase separation and in-situ swelling," Applied Physics Letters (to appear), 2008.

2. B. Fan, S. D. Vartak, J. N. Eakin and S. M. Faris, "The surface anchoring effects of spectral broadening of CLC polarization films, Advanced Materials (submitted), 2007.

3. S. J. Woltman, J. N. Eakin, S. Zumer and G. P. Crawford, "Electro-Optical Investigations of Holographic Polymer Dispersed Ferroelectric Liquid Crystals," Journal of the Optical Society of America A, 24, 12, 3789-3799 (2007).

4. S. J. Woltman, J. N. Eakin and G. P. Crawford, "Laser emission from dye-doped liquid crystal gratings formed by polarization holography," Molecular Crystals and Liquid Crystals 477, 235-244 (2007).

5. J. N. Eakin, S. J. Woltman, S. Zumer and G. P. Crawford, "Holographic polymer dispersed ferroelectric liquid crystals for diffractive optical elements," Proceedings of the 26th Society for Information Display International Display Research Conference, 1, pp. 379-382 2006.

6. S. J. Woltman, J. N. Eakin, S. Zumer, and G. P. Crawford, "Holographic diffraction gratings using polymer dispersed ferroelectric liquid crystals," Optics Letters 31 number 22, pp. 3273-3275, November 2006.

7. J. N. Eakin and G. P. Crawford, "2-D Liquid crystal patterning using holographically exposed alignment layers," Proceedings from the 22nd International Liquid Crystal Conference (submitted), 2006.

8. S. J. Woltman, J. N. Eakin and G. P. Crawford, "Lasing from a liquid crystal grating formed by polarization holography," Proceedings from the 22nd International Liquid Crystal Conference (to appear), 2006.

9. J. W. McMurdy, J. N. Eakin and G. P. Crawford, "Microspectrometer based on vertically aligned deformed helix ferroelectric liquid crystal," Proceedings from the 22nd International Liquid Crystal Conference (to appear), 2006.

10. S. G. Cloutier, J. N. Eakin, R. S. Guico, M. E. Sousa, G. P. Crawford, and J. M. Xu, "Molecular self-organization in cylindrical nanocavities," Physical Review E 73, number 5, pp. 051703, May 2006.

11. J. N. Eakin and G. P. Crawford, "Single Step Surface Alignment Patterning in Liquid Crystals Using Polarization Holography Exposure, Society for Information Display Digest of Technical Papers XXXVII, (accepted), 2006.

12. J. W. McMurdy, J. N. Eakin and G. P. Crawford, "Vertically Aligned Deformed Helix Ferroelectric Liquid Crystal Configuration for Reflective Display Device," Society for Information Display Digest of Technical Papers XXXVII, pp. 677-681, 2006.

13. G. P. Crawford, J. N. Eakin, M. D. Radcliffe, A. Callan-Jones, and R. A. Pelcovits. "Liquid Crystal Diffraction Gratings using Polarization Holography Alignment Techniques," Journal of Applied Physics 98, number 12, pp. 123102-123111, December 2005.

14. K. Jian, H. Xianyu, J. N. Eakin, Y. Gao, G. P. Crawford, R. H. Hurt. "Orientationally Ordered and Patterned Discotic Films and Carbon Films from Liquid Crystalline Precursors," Carbon 43, number 2, pp. 407-415, November 2004.

15. J. N. Eakin, M. D. Radcliffe, Y. Xie, R. A. Pelcovits, and G. P. Crawford, "Vanishing Freedericksz Threshold Voltage in Periodically Aligned Liquid Crystals," Applied Physics Letters 85, number 10 pp. 1671-1673, September 2004.

16. I. Amimori, J. N. Eakin, J. Qi, G. Skacej, S. Zumer, and G. P. Crawford, "Surface Induced Orientational Order in Nanoscale-Sized Polymer Dispersed Liquid Crystal Droplets," Physical Review E 71, number 3, 031702, March 2005.

17. J. N. Eakin, Marc D. Radcliffe, Y. Xie, R. A. Pelcovits, and G. P. Crawford, "Photoalignment of Liquid Crystals Using Polarization Holography" Proceedings from the 20th International Liquid Crystal Conference Molecular Crystals and Liquid Crystals 438 pp. 1749, 2005.

18. J. N. Eakin, Marc D. Radcliffe, and G. P. Crawford, "Morphological studies of Holographically formed Polymer Dispersed Ferroelectric Liquid Crystals using elevated temperature exposure" Proceedings from the 20th International Liquid Crystal Conference, Molecular Crystals and Liquid Crystals 439 pp. 1885, 2005.

19. J. N. Eakin, Marc D. Radcliffe, Y. Xie, R. A. Pelcovits, and G. P. Crawford, "Morphological Studies of Holographically Formed Polymer Dispersed Ferroelectric Liquid Crystals," Proceedings from the 6th Italian Liquid Crystal Conference, Molecular Crystals and Liquid Crystals 429, pp. 277, 2005.

20. J. N. Eakin, Y. Xie, R. A. Pelcovits, and G. P. Crawford, "Patterned Alignment Layers Using Holographic Exposure Technique," SID Digest of Technical Papers XXXV, pp 578-581, May 2004.

21. J. N. Eakin, I. Amimori, and G. P. Crawford, "Ordering in Liquid Crystal Droplets for Scattering Polarizer Applications," SPIE International Symposium - Optical Science and Technology, Liquid Crystals VII 5213, pp 283-281, August 2003.

22. J. N. Eakin, I. Amimori, and G. P. Crawford "Ordering in Highly Anisotropic Liquid Crystal Nano-Droplets: Scattering Polarizer Applications," SID Digest of Technical Papers XXXIV, pp 672-674, May 2003.

23. M. E. Sousa, J. N. Eakin, and G. P. Crawford, "Robust Polymer Stabilization for Cholesteric Liquid Crystal Reflective Displays," SID Digest of Technical Papers SID Digest of Technical Papers XXXIV, pp 636-638, May 2003.

24. I. Amimori J. N. Eakin, and G. P. Crawford, "The Mechanism of Liquid Crystal Alignment in Stretched PDLC Films for Scattering Polarizers" Proceeding of the International Display Manufacturing Conference 2003, pp. 619-622, February 2003.

25. K. K. Vardanyan, J. Qi, J. N. Eakin, M. DeSarkar and G. P. Crawford, "Polymer Scaffolding Model for Holographic Polymer Dispersed Liquid Crystals," Applied Physics Letters, 81 number 25, pp.4736-4738, 16 December 2002.

26. Y. Boiko, J. N. Eakin, J. Vedrine and G.P. Crawford, "Polarization -selective switching in holographically formed polymer dispersed liquid crystals," Optics Letters, 27, number 19, pp. 1717-1719, 1 October 2002.

27. I. Amimori, J. N. Eakin, N. V. Priezjev, R. A. Pelcovits and G. P. Crawford, "Optical and Mechanical Properties of Stretched PDLC films for Scattering Polarizers," SID Digest of Technical Papers XXXIII, pp 834-837, May 2002.

Acknowledgements

What a journey this has been! I would first like to thank all of the past and present members of the Display and Photonics laboratory for the camaraderie and friendships that have developed through this unique experience. It has truly been a pleasure working with all of them during my tenure at Brown. A special thanks goes to Dr. Scott Woltman for his amazing scientific and editing abilities that have helped me assemble this body of work and Dr. Matthew Sousa for the companionship in our many travels.

To Professor James McCargar at Baldwin-Wallace College for being instrumental in my decision making process to pursue a Ph.D. and the introduction to Greg. He was right about Greg! His scientific creativity, enthusiasm, and persistence are second to none.

To my advisor, Greg Crawford, I extend my thanks for providing me with an amazing opportunity to be a part of his group and mature as a researcher. It has been a privilege to work alongside him and to experience his creativity and brilliance first hand. I owe a debt of gratitude to him for seeing the raw potential in me, long before I saw it and enabling me to see the big picture.

Additionally, a very special thanks goes to Elif Alpaslan and my parents, Jim and Diane Eakin, who have been by my side through this ongoing process providing never ending love, support and encouragement. I couldn't accomplish any of this without them in my life.

Lastly, this thesis is dedicated in loving memory to Carl A. Chance III (Uncle Cork) and Sophie C. Eakin (Nana) who passed away before this body of work was completed.

Contents

List of Tables

List of Figures

Chapter 1

Introduction to Liquid Crystals

In 1888, an Austrian botonist, Friedrich Reinitzer, observed two distinct melting temperatures for cholesteryl benzoate [2,3]. When the material heated to 145.5 °C, it transformed from a crystalline solid to a cloudy liquid; and, upon further heating, he noted the material underwent an additional clearing transition at 178.5 °C. In 1889, Otto Lehmann confirmed these earlier findings to be an actual phase of matter, and began referring to this cloudy liquid phase as soft crystals (later to be known as liquid crystals) – as they shared properties with both crystalline solids and isotropic fluids. Liquid crystals (LCs) have a viscosity similar to those of a liquid, but also possess a degree of ordered molecular arrangement like that of a crystal. Additionally their optical and electrical properties make them very attractive for numerous applications in flat panel displays, telecommunications and optical security.

1.1 Classes of Liquid Crystals

Liquid crystals are broadly categorized as either lyotropic or thermotropic, depending on how the liquid crystal phase transition occurs. For lyotropics, a stable LC phase is present in a solution for optimum concentrations; for thermotropics, a stable LC phase occurs over an optimum temperature

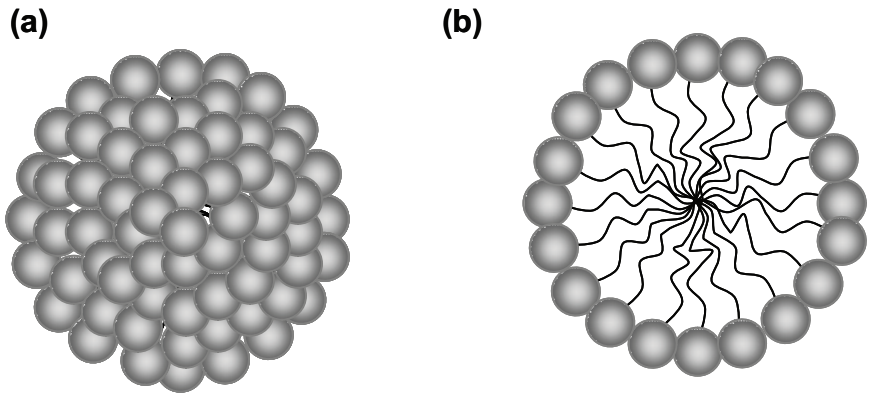

Figure 1.1: (a) Schematic illustration of a micelle and (b) cross-sectional view of a micelle.

range. The following section provides a brief overview of both classifications; however, this thesis will focus on thermotropics and their applications.

1.1.1 Lyotropics and Thermotropics

A lyotropic liquid crystal phase is formed from molecules having a hydrophilic group at one end and a hydrophobic group at the other. These types of molecules are commonly referred to as amphiphilic molecules, and include soaps and phospholipids [4]. When dispersed in a solvent, they can form ordered two- and three-dimensional structures. The shape of the structure formed from these molecules depends on both the solvent type and the solvent concentration. When amphiphilic molecules are dispersed in a polar solvent, the hydrophobic tails of the molecules self-assemble, presenting the hydrophilic heads to the solvent. An example of soap molecules forming a micelle is shown in Figure 1.1(a); a cross-sectional view of the micelle is shown in Figure 1.1(b). Some phospholipids form similar structures known as vesicles, which are bilayers of self assembled amphiphiles, where the hydrophobic carbon tails are shielded from the polar solvent by a hydrophilic shell.

When a non-polar solvent is used, the hydrophilic heads will self-assemble to present the hydrophobic tails to the solvent. In this case the soap molecules, for instance, will self-assemble to form a reverse micelle, schematically shown in Figure 1.2.

Thermotropic liquid crystals are single component systems forming LC phases over a stable

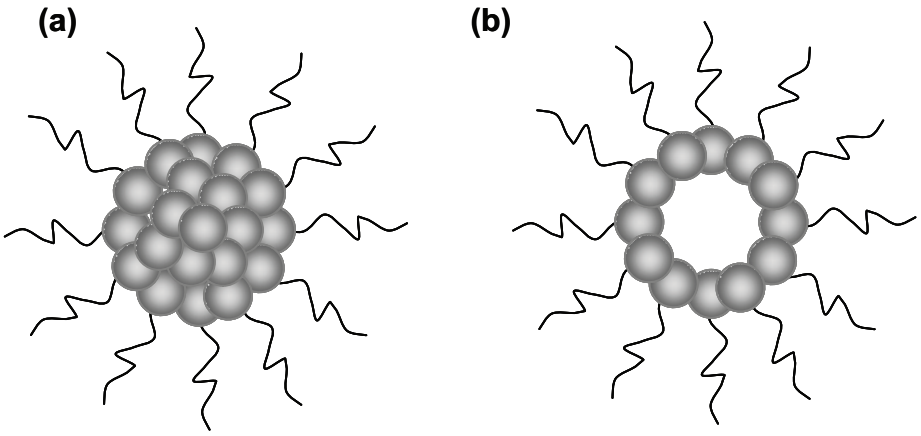

Figure 1.2: (a) Schematic illustration of a reverse micelle and (b) cross-sectional view of a reverse-micelle.

temperature regime, rather than through a change in solvent concentration. This is particularly useful in electro-optic applications, in which a material can exhibit a liquid crystal phase over a broad temperature regime. A typical phase sequence for a thermotropic LC is illustrated in Figure 1.3.

In a crystalline solid phase, molecules exhibit three-dimensional positional and orientational ordering – meaning there is a direct correlation between their centers of mass as they remain on fixed lattice points, in addition to being aligned along a common direction.

In the nematic liquid crystal phase, the least ordered LC phase, molecules exhibit orientational ordering in one dimension, but lack positional ordering. The average orientation for the long axis of an ensemble of molecules is denoted by the unit vector **n**, also referred to as the nematic director. Since these molecules exhibit a head-and-tail equivalency, there is no distinction between **n** and **-n**.

In contrast to the ordered and semi-ordered phases of the crystalline solid and nematic LC, the isotropic fluid is completely disordered. This phase lacks both orientational and positional ordering, making it a completely random ensemble of molecules.

A quantitative discussion on determining the degree of ordering in these three phases will be presented in Section 1.2.1.

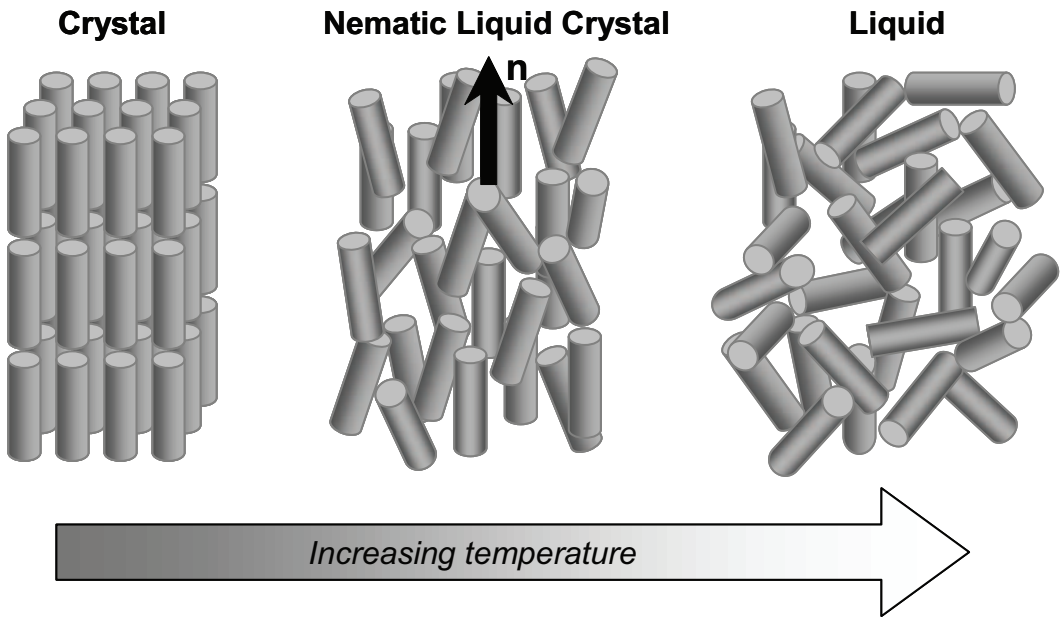

Figure 1.3: Schematic illustration of a phase sequence for a calamitic thermotropic liquid crystal material. With increasing temperature, the material transitions from the crystalline solid, to the nematic LC, to the isotropic fluid.

Nematics and Chiral Nematics

As mentioned, the nematic LC phase is the simplest liquid crystal phase, having only orientational ordering in one-dimension.

In contrast, the chiral nematic LC phase – materials also often referred to as cholesteric liquid crystals (CLCs) – possess a non-inversion symmetry, brought upon by a chiral carbon center. The chirality generates a steric hindrance between the close packing of the molecules and causes the liquid crystal molecules to twist with respect to one another. In this phase, the nematic director rotates in a helical fashion about an axis perpendicular to the nematic director. The distance for this helical twist to rotate 2π is defined as the pitch, P. The cholesteric pitch length can be increased or decreased through chemical dopants, electro-magnetic fields and temperature. Since the pitch length is typically on the order of the wavelength of visible light, CLCs produce a coherent Bragg reflection because of the periodic modulation in the refractive index propagating through the depth of the material.

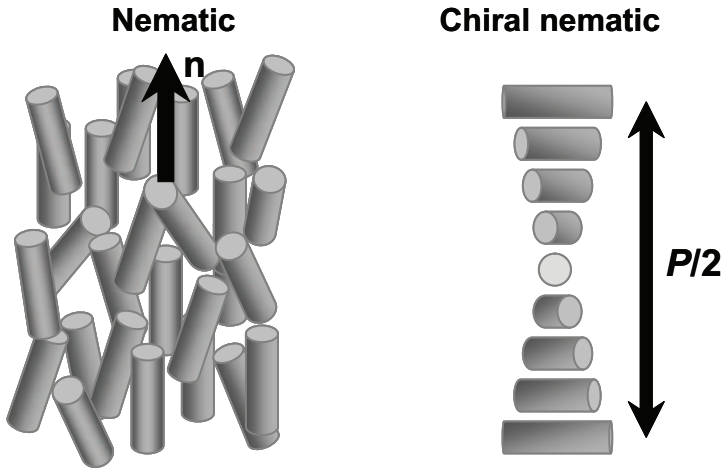

Figure 1.4: A schematic illustration of a nematic as compared to a chiral nematic (cholesteric liquid crystal).

Smectics and Chiral Smectics

The smectic LC phases exhibit a higher degree of ordering than nematics as they possess both some positional and orientational order. These materials share the same orientational ordering as the nematic liquid crystal phase, but have an additional ordering term in the form of a molecular density modulation in one direction. This positional orientation is sometimes referred to as a bookshelf symmetry. As its name suggests, molecules are aligned in a single direction and form a lamellar structure perpendicular to that direction. The smectic phase can be further subdivided into phases that are non-tilted and tilted. A non-tilted smectic phase, called the smectic-A phase (SmA), has an average molecular director aligned perpendicular to the smectic layers. If the average molecular director is aligned at an angle other than 90° with respect to the smectic layers, the phase is referred to as a tilted smectic, or smectic-C (SmC) phase.

The SmC phase also has a chiral phase analogous to the chiral nematic phase. In the chiral SmC phase, also known as the SmC* or ferroelectric liquid crystal (FLC) phase, the molecules remain tilted at an angle θ with respect to the layer normal in the bookshelf geometry, but continuously rotate along a cone angle from layer to layer. This creates a helical structure where again the pitch (P) is defined as the distance it takes the molecules to rotate 2π. As with CLCs, this pitch length

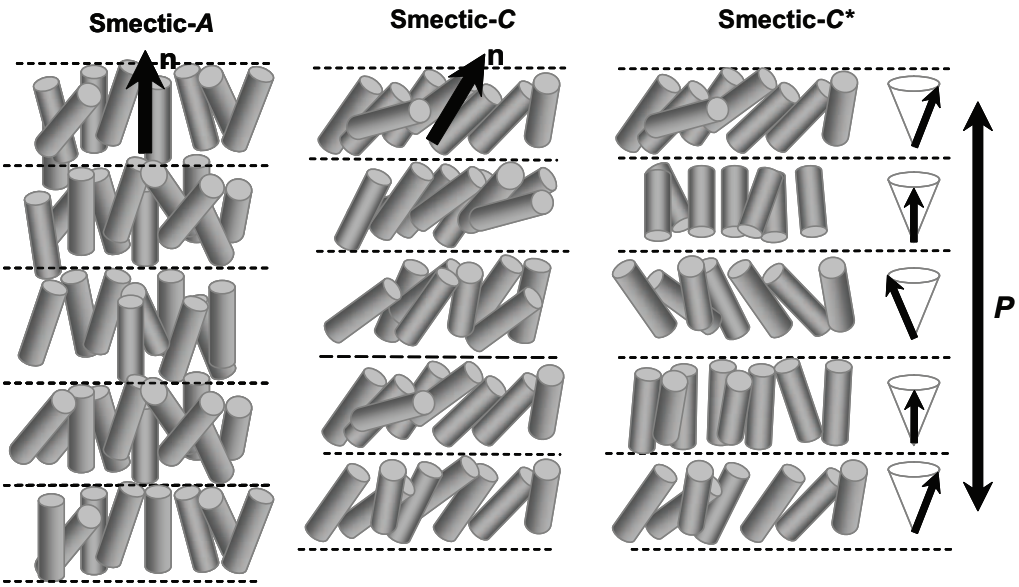

Figure 1.5: A schematic illustration of the smectic-A (SmA), smectic-C (SmC), and chiral smectic-C (SmC*) phases.

can also be increased or decreased by chemical dopants, electro-magnetic fields and temperatures. A schematic illustration showing the differences between the SmA, SmC, and SmC* phases is shown in Figure 1.5.

1.2 Physical Properties of Liquid Crystals

1.2.1 Order Parameter

In the previous section, the LC phase was introduced as a semi-ordered phase existing between the crystalline solid and isotropic fluid phases. These three phases were described qualitatively in the context of a presence or absence of orientational or positional orders. The degree to which these phases are ordered can be represented using the Maier-Saupe formalism first introduced in 1959 [5]. In this approach, the amount of order in a nematic LC phase is quantified by the order parameter, S, which is defined by the average of a second Legendre polynomial shown as:

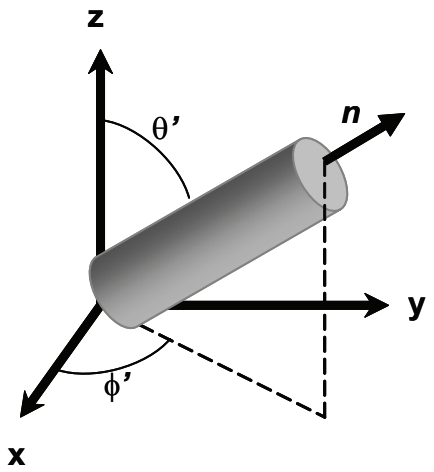

Figure 1.6: The coordinate system labeling the polar (θ'), and azimuthal (ϕ') angles.

$$S = \langle P_2(\cos\theta')\rangle = \left\langle \frac{3}{2}\cos^2\theta' - \frac{1}{2} \right\rangle, \tag{1.1}$$

where the brackets are used to represent either a time average for a single molecule or a snapshot in time for the ensemble of molecules; and θ' is the average angular deviation of the molecules. In the perfectly ordered crystalline solid $\theta' = 0$, to give an order parameter of $S = 1$.

In the isotropic liquid case, the order parameter S is calculated by averaging over a distribution function $f(\theta')$ and integrating over the solid angle as shown:

$$S = \frac{\int_0^{2\pi} \mathrm{f}(\theta')\left(\frac{3}{2}\cos^2\theta' - \frac{1}{2}\right)\sin\theta' \mathrm{d}\theta' \int_0^{2\pi} \mathrm{d}\phi'}{\int_0^{\pi} \mathrm{f}(\theta')\sin\theta' \mathrm{d}\theta' \int_0^{2\pi} \mathrm{d}\phi'} \propto \frac{\int_{-1}^{1} \left(\frac{3}{2}x^2 - \frac{1}{2}\right)\mathrm{dx}}{\int_{-1}^{1} \mathrm{dx}} = 0, \tag{1.2}$$

using $x = \cos^2\theta'$ as a substitution. The coordinate system for the solid angle is shown in Figure 1.6, where θ' and ϕ' represent the polar and azimuthal angles, respectively.

The orientational order parameter for a liquid crystal phase can also be calculated in the same manner; that is, using a distribution function and integrating over the solid angle. Because the liquid crystal phase still has the thermal diffusion properties of a liquid, the order parameter, S, is a function of temperature. Deep in the nematic phase, the order parameter typically ranges from

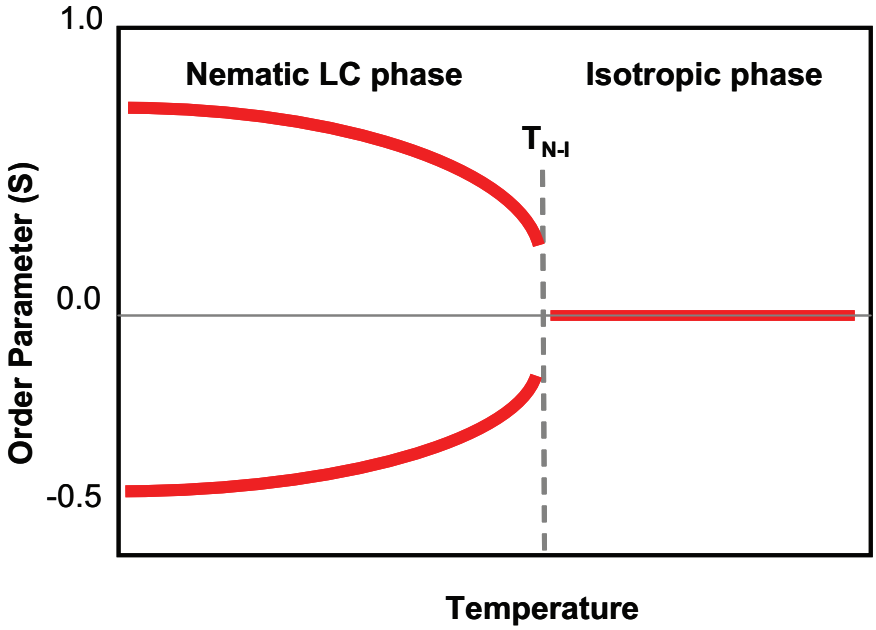

Figure 1.7: The order parameter as a function of temperature.

$0.6 - 0.8$, and can decrease to values from $0.25 - 0.3$ near the isotropic phase. The order parameter for a nematic liquid crystal is plotted as a function of temperature in Figure 1.7.

The nematic phase order parameter undergoes a weakly discontinuous first order phase transition at the nematic-isotropic transition temperature, T_{N-I}, as depicted in the temperature profile plot in Figure 1.7.

The nematic liquid crystal can exhibit either a positive order parameter, $S > 0$, or a negative order parameter, $S < 0$, as shown in Figure 1.7. The positive order parameter is the most energetically favorable, but there also exist rare circumstances in which a negative order parameter occurs; in this case the molecules are randomly oriented in the plane of a surface with the nematic director perpendicular to this surface.

The approach above describes the foundations of the liquid crystal order parameter from a statistical standpoint. From an experimentalist's point of view, the order parameter can be determined using X-ray diffraction, Raman scattering, or nuclear magnetic resonance (NMR), among other techniques.

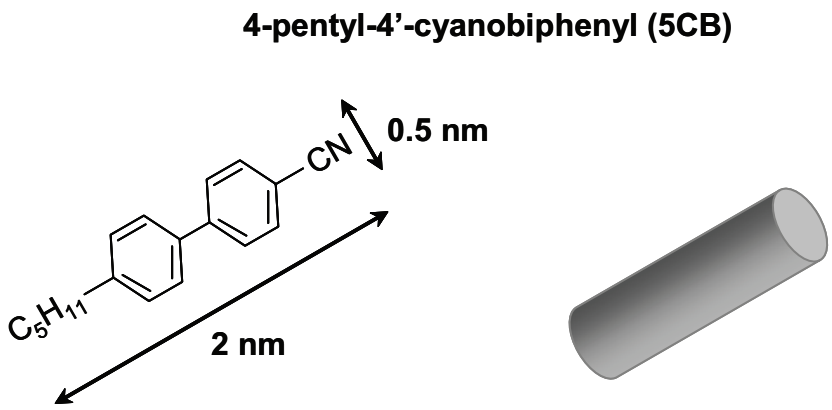

Figure 1.8: The chemical structure and anisotropic shape representation for 4-pentyl-4'-cyanobiphenyl (5CB), a commonly used calamitic LC material in electro-optic applications.

1.2.2 Shape Anisotropy

All liquid crystal materials exhibit a shape anisotropy and can be broadly categorized as either calamitic (rod-like) or discotic (disc-like). This shape anisotropy, defined by the aspect ratio between the lengths of the molecule along its distinct molecular axes (typically $2-4$:1), distinguishes LCs from isotropic fluids and enables the molecules to align along a preferential direction. For calamitics, the shape anisotropy is attributed to a rigid and elongated core typically comprised of a series of phenyl rings. The addition of terminal groups, such as flexible hydrocarbon chains, affects the thermal properties of the material, and polar groups (e.g., cyano or fluorinated groups) affect the electrical properties. The molecular structure, and rod-like shape representation of 4-pentyl-4'-cyanobiphenyl (5CB), which is a commonly used calamitic thermotropic liquid crystal, is illustrated in Figure 1.8.

An example of a common discotic LC is shown in Figure 1.9. Like calamitics, discotics can also exhibit both nematic and smectic phases. For the purpose of this thesis, only calamitics will be discussed.

The anisotropy introduced by the calamitic shape of molecules, like the one shown in Figure 1.8, is manifested in its dielectric and optical properties, which will be discussed in the following sections.

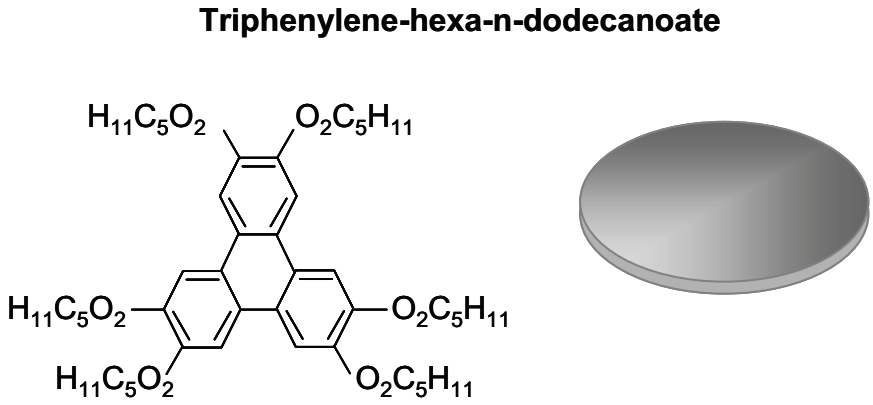

Figure 1.9: The chemical structure and anisotropic shape representation of Triphenylene-hexa-n-dodecanoate, a commonly used discotic LC material.

1.2.3 Dielectric Anisotropy

Most liquid crystals are dielectric materials – they remain electrically neutral until an electric field is applied. Assuming the field is not too strong, a dipole moment $\mathbf{P}$ can be induced in the liquid crystal material and is written as:

$$\mathbf{P} = \varepsilon_{\mathbf{0}}\chi_{\mathbf{0}}\mathbf{E}, \tag{1.3}$$

where $\varepsilon_0 = 8.85 \times 10^{-12}$ C^2/Nm^2 is the permittivity of free space; and χ_0 is the electric susceptibility. Once the field is removed, the induced dipole disappears and the system once again becomes electrically neutral. The exception to this case is the ferroelectric liquid crystal phase, which has a permanent dipole perpendicular to the long axis of each molecule. This phase will be described in greater detail in Chapter 5.

The dielectric anisotropy, $\Delta\varepsilon$, is defined as the difference between the dielectric constant parallel, $\epsilon_{||}$, and perpendicular, $\varepsilon_\perp$, to the long axis of the molecule. It creates a preferential charge migration when an electric field is applied across the system:

$$\Delta\varepsilon = \varepsilon_{||} - \varepsilon_\perp. \tag{1.4}$$

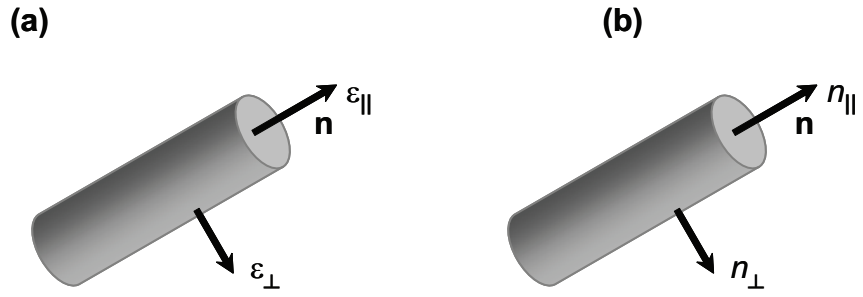

Figure 1.10: A schematic illustration of the dielectric and optical anisotropy of a liquid crystal.

If the system possesses a positive dielectric anisotropy ($\varepsilon_{||} > 0$), the electric field will induce a charge migration to opposite ends of the long axis of the molecules and result in a dipole moment. This in turn induces a torque on the molecules in the direction of the electric field, with the long axis of the molecules aligning parallel to the field lines.

If the system possesses a negative dielectric anisotropy ($\varepsilon_{||} < 0$) charge migration will occur perpendicular to the long axis of the molecule, and will align the molecules perpendicular to the field lines. The dielectric anisotropy values for commercially available liquid crystals are typically on the order of $2 - 20$.

1.2.4 Optical Anisotropy

The speed of light propagating through an isotropic material is governed by the following equation: $v = c/n$; where c is the speed of light in a vacuum and n is the refractive index of the material. This value is also related to the square of the dielectric constant at optical frequencies: $n^2 = \varepsilon$. In the case of an isotropic material, incident light will only experience one index of refraction, independent of the molecular orientation.

For materials possessing a dielectric anisotropy, light will propagate through the material at different velocities. This phenomenon, known as optical anisotropy or birefringence (Δn), is also introduced into the liquid crystal phase by the molecular shape anisotropy.The optical anisotropy is defined as the difference in the index of refraction for incident light polarized parallel to and

perpendicular to the direction of the long molecular axis:

$$\Delta n = n_e - n_o. \tag{1.5}$$

Since calamitic liquid crystals have a shape anisotropy, light propagates through the material at different velocities relative to the molecular orientation and incident polarization. The ordinary index of refraction, n_o, is defined as the direction in which the incident polarization is perpendicular to the long axis of the molecule. Likewise, the extraordinary index of refraction, n_e, is defined as the direction in which the incident polarization is parallel to the long axis of the molecule. A schematic illustration of the optical anisotropy, depicting both n_o and n_e is shown in Figure 1.10.

The general form for calculating the refractive index of an arbitrary orientation is:

$$n(\theta) = \left[\frac{\cos^2\theta}{n_e^2} + \frac{\sin^2\theta}{n_o^2}\right]^{-1/2}, \tag{1.6}$$

where θ represents the angle between the direction of the incident polarization and the long axis of the molecule.

Typical birefringence values for commercially available liquid crystal materials are on the order of $0.05 - 0.3$. Because liquid crystals are a birefringent material, they appear optically active between crossed polarizers, showing a rich panoply of colors and textures corresponding to varying molecular orientations. As they are heated to temperatures approaching the nematic-isotropic temperature transition (T_{N-I}) the birefringence decreases. Once a material reaches T_{N-I}, all birefringence is lost in the isotropic state.

This phase transition process from liquid crystal to isotropic fluid is a reversible process. The ensemble of molecules can return to the nematic liquid crystal phase as the temperature of the system is decreased below T_{N-I}. This method is commonly used by researchers to experimentally determine the phase transition temperatures of a material, as indicated by Reitizer's early findings [2].

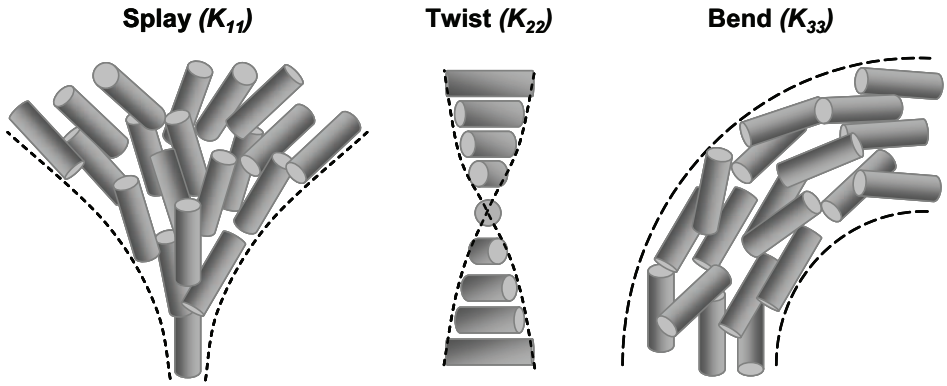

Figure 1.11: Elastic constants of (a) K_{11} splay, (b) K_{22} twist, and (c) K_{33} bend deformations.

1.2.5 Elastic Energy

The configurations of liquid crystals described so far have assumed a uniform director profile, which is the simplest configuration and is an equilibrium state. When the director profile is spatially modulated or varied, a non-equilibrium state is formed. Variations in this non-equilibrium state are observed on the macroscopic levels and create only small variances on the microscopic level. Because of this, one can assume the order parameters will remain constant, and examine only the elastic energy of the liquid crystal system. The static free elastic energy density of a volume can be written according to the Oseen-Frank theory:

$$F_{elastic} = \frac{1}{2}\int_{vol}\Big[K_{11}\left(\nabla\cdot\mathbf{n}\right)^2 + K_{22}\left(\mathbf{n}\cdot\nabla\times\mathbf{n}\right)^2 + K_{33}\left(\mathbf{n}\times\nabla\times\mathbf{n}\right)^2\Big]d^3x, \tag{1.7}$$

where n is the nematic director; and K_{11}, K_{22}, and K_{33} represent the elastic constants of splay, twist and bend shown, respectively, in Figure 1.11.

Using a single constant approximation ($K = K_{11} = K_{22} = K_{33}$) the elastic free energy can be written as:

$$F_{elastic} = \frac{1}{2}\int_{vol}\Big[K\left(\nabla\cdot\mathbf{n}\right)^2 + K\left(\nabla\times\mathbf{n}\right)^2\Big]d^3x. \tag{1.8}$$

Typical values for these elastic constants are on the order of 10^{-11} N, and are approximated by

taking the ratios of the intermolecular interaction energies to the average molecular distances for these configurations. By taking into account the free elastic energy described above, along with the surface and electric field energies, it becomes possible to determine the equilibrium states, as well as the electro-optic properties (such as critical fields and response times) for complex configurations of liquid crystals. Understanding the physical properties and constraints of these complex configurations allow researchers to develop optimized device applications that take full advantage of the optical and electrical properties of liquid crystals.

Taking into account the application of an external field, the change in free energy can be expressed as:

$$F_{field} = -\frac{1}{2}\varepsilon_0 \Delta\varepsilon \left[\mathbf{E} \cdot \mathbf{n}\right]^2 . \tag{1.9}$$

For molecules possessing a positive dielectric anisotropy, the free energy of the system will be reduced as the nematic director aligns parallel to the applied electric field.

1.3 Liquid Crystal Alignment

The previous sections provided a condensed overview of the liquid crystal phase from an isolated perspective. It is through the interaction with solid surfaces that this unique phase can be used in electro-optic applications. This section will begin with the most common alignment configurations – planar alignment and homeotropic alignment, and conclude with recent advances in liquid crystal alignment technology, highlighting novel methods and materials to create hybrid alignment configurations. The impact of this groundwork plays a major role in the theme of this thesis.

1.3.1 Planar Alignment

In a planar aligned system, the LC molecules are manipulated to align uniformly with the director parallel to the surface. This can be accomplished using a number of chemical, mechanical or optical

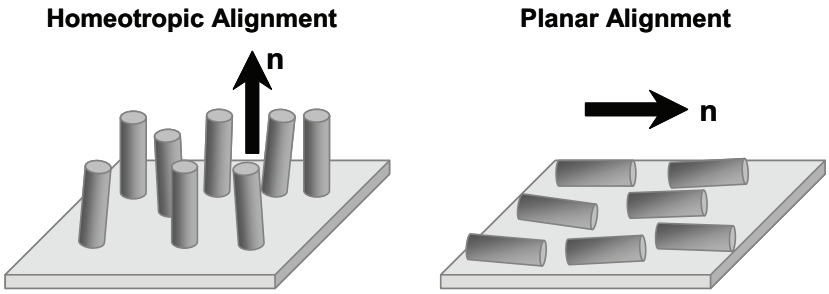

Figure 1.12: Illustrations of homeotropic and planar liquid crystal alignments.

treatments that induce a preferential ordering directly on the surface. The most common method today uses a soft, short fiber cloth that comes in direct contact to mechanically rub a polymer coated surface. This rubbing technique, discovered by Charles Mauguin in 1911, creates microgrooves in the polymer film surface and induces an alignment propagating to a depth of several micrometers. The long axis of the LC molecules align parallel to the microgrooves created by the rubbing process in order to minimize the free energy, as illustrated in Figure 1.12.

While this rubbing process has been seamlessly integrated in the liquid crystal display (LCD) manufacturing process it is not without limitations. The process of mechanically rubbing a polymer (polyimide) film inherently creates static charge and dust contaminants that can destroy sensitive thin film transistors (TFTs) and other electric components below the polyimide layer. Additionally, this alignment process can only create a mono-domain alignment configuration, which limits the optical viewing angle for large area displays. For this reason, research has intensified on developing novel non-contact, photo-alignment methods that exhibit multi-domain patterning to promote large viewing angles while eliminating static charge and dust contaminants.

1.3.2 Homeotropic Alignment

In a homeotropic alignment, the LC molecules uniformly align perpendicular to the surface, as shown in Figure 1.12. This is typically accomplished through chemical treatment methods on the surface using surfactants, or detergents (lecithin). As a result, the polar head groups of the surfactants

are chemically bonded to the surface, allowing the aliphatic tails to align perpendicular to the surface. When the liquid crystal comes into contact with this surface treatment, the long axis of the LC molecules preferentially align parallel to the direction of the aliphatic tails, perpendicular to the surface of the substrate. In addition to surfactants, certain polyimide materials also induce homeotropic alignments.

1.3.3 Anchoring Energy

The presence of aligning surfaces also plays a key role in the free energy of the system as expressed by:

$$F_{surface} = \frac{1}{2} W_0 \sin^2 (\theta'' - \theta_0), \tag{1.10}$$

where W_0 represents the surface anchoring energy strength, and $\theta'' - \theta_0$ is the angular deviation of the LC director from its preferred orientation. Anchoring energy strengths can be classified as weak anchoring ($\sim 10^{-7}$ N/m^2) or strong anchoring ($\sim 10^{-5}$ N/m^2), depending on the interaction between the surface (alignment material) and the liquid crystal. Typically, polyimide films promote strong anchoring, while photo-alignment methods promote weak anchoring.

1.3.4 Hybrid Alignment

In the previous section, the principles of planar and homeotropic liquid crystal alignment were introduced as uniform, mono-domain alignment geometries. A hybrid alignment is a combination of multiple, mono-domain alignment configurations that spatially vary across the surface. Examples of hybrid geometries include periodic domains of homeotropic and planar alignment, and periodic domains of orthogonal planar alignment. When these periodic alignment configurations are combined with a top alignment surface promoting either mono-domain or registered multi-domain alignment a number of LC splay, twist and bend configurations can be achieved.

Hybrid alignment methods are classified as either contact methods or non-contact methods. In the contact methods, mechanical apparatuses (such as buffing cloths, atomic force microscopy (AFM) tips, micro ball bearings, etc.) directly contact and modify the surface morphology through the creation of grooves. In comparison, non-contact methods typically use photoactive materials that, under the proper irradiation conditions, selectively change the orientation of the alignment material.

Contact Methods

Rubbed polyimide materials are known to be excellent candidates for promoting planar alignments. Chen and coworkers expanded on this idea to create two and four domain twist configurations using multiple rubbings [6]. In this approach, a polyimide material was first coated and rubbed by conventional buffing, then patterned with a photoresist material and rubbed in the orthogonal direction. Upon the removal of the photoresist, the LC exhibited periodic regions of orthogonal and reverse twist configurations.

Varghese and coworkers [7,8] and Honma and coworkers [9,10] have created periodic, and hybrid domains using a μ-rubbing technique. In this method, a millimeter-sized ball bearing is brought into contact with the polyimide surface. The amount of load on the ball bearing modifies the surface morphology and has been demonstrated with both homeotropic and planar polyimides. The end result is a multi-domain configuration with high pre-tilt angles and significant viewing angle improvements over conventional mono-domain LCD configurations.

Rosenblatt and co-workers have also manipulated polyimide coated surfaces to produce multi-domain planar alignment configurations using atomic force microscopy (AFM) scribing [11]. In this embodiment, an AFM tip is used as a stylus to scribe gratings, grooves, and complex patterns, thus enabling multi-domain planar alignment configurations with high resolution. While this method is extremely attractive for creating complex patterns and shapes, it is extremely time consuming and not appropriate for large area displays requiring hybrid alignment configurations.

Non-contact Methods

Non-contact, or photoalignment methods, are alternative approaches to the direct-contact methods for creating hybrid LC configurations. In these cases, a surface is coated with a photo-sensitive material and irradiated with light to induce a chemical change in the material at the surface, which in turn affects the alignment properties of the LC. Independent of the underlying chemistries, these processes are commonly referred to as photo-buffing techniques.

The seminal publication on photobuffed LC alignment layers was presented by Gibbons and coworkers in 1991 [12]. Using a polyimide mixed with an azo-benzene dye, they demonstrated a reorientation of LC in the presence of linearly-polarized ultraviolet (UV) light. During the UV illumination, the LC director twisted in the azimuthal plane to align perpendicular to the incident polarization direction. In the absence of the UV illumination, the LC director untwisted to its original configuration. This photoalignment chemical process, known as photoisomerization, is a reversible process that induces a reorientation of the azo-benzene molecules and will be discussed in detail in Chapter 2. Since this publication, many groups have focused their research efforts on investigating new materials for the preferential alignment of liquid crystals.

Schadt and coworkers at ROLIC, Inc. developed a photo-buffing material that relies on a photodimerization process [13]. This material, like Gibbons', can be coated on a substrate and exposed to linearly polarized UV light to induce a planar liquid crystal alignment perpendicular to the direction of the incident polarization. Unlike Gibbons' material, this photo-buffing process is irreversible after UV illumination. The LC alignment orientation at the surface is preserved as a stable configuration. This process will also be further described in detail in Chapter 2. Since their first publication, Schadt and ROLIC, Inc. have published results on other photo-sensitive alignment materials that align in the presence of polarized UV irradiation. In particular, the photo-alignment materials used in Chapters 3 and 4 were a commercially available material from ROLIC that produced planar alignment parallel to the direction of incident UV polarization.

In addition to photoisomerization and photodimerization materials, other materials can undergo a depolymerization process in the presence of UV irradiation. Wen and coworkers have demonstrated a hybrid alignment configuration using octadecyltriethxysilane self assembled monolayers (SAMs) [14]. In the absence of unpolarized UV irratiation, the SAMs promote homeotropic alignment for LC materials. As the SAM is irradiated with UV light, a photo-induced depolymerization occurs to transform the alignment from homeotropic to planar.

All of the above mentioned hybrid alignment surface treatments are fascinating in terms of their underlying chemistry, physics, optics, and materials science. The non-contact alignment materials are optically active with linearly polarized ultraviolet light and can be used in conjunction with lithographic or holographic recording techniques. Holographic exposures can employ two or more beams to create complex one-, two-, and three-dimensional interference patterns. These interference patterns, which modulate both amplitude and polarization, will be discussed in Chapter 2. The application of polarization holography for photoalignment will be described in Chapters 3 and 4. Holographic-polymer dispersed ferroelectric liquid crystals will be discussed in Chapter 5.

1.4 Summary

In this chapter, the basic classifications of liquid crystals have been introduced, along with their intrinsic optical, mechanical, and chemical properties. Additionally, the framework has been laid to understand the interaction of solid surfaces with the LC molecules to promote micro- and macroscopic alignments. An introduction to holography and gratings will be discussed in Chapter 2, as the topic relates to the periodic alignment LC configurations demonstrated in Chapters $3-5$.

Chapter 2

Holography and Gratings

The following section introduces mathematical relations to explain the wavelike nature of all electromagnetic (EM) radiation. While the EM spectrum encompasses gamma, X, ultraviolet (UV), visible, infrared (IR), micro and radio waves, only the (UV) and visible portions will be discussed in this thesis. The concepts discussed in this chapter provide merely a brief overview of the subject matter and serve as an introduction to the holographically patterned liquid crystal studies and applications that follow in the remaining chapters. For a more mathematically rigorous approach to this introduction, a number of references are available [15, 16].

2.1 The Propagation of Light in Matter

Maxwell's theory proved light can be described as an electromagnetic wave. The propagation of light can be described by Maxwell's equations in their differential form:

$$\nabla \times \mathbf{E} = -\frac{\partial \mathbf{B}}{\partial t} \tag{2.1}$$

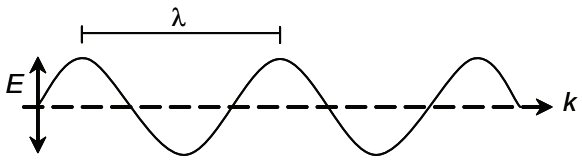

Figure 2.1: The plane wave propagation of light is often defined by its wavevector **k**, wavelength λ, and its oscillating electric field **E**.

$$\nabla \times \mathbf{H} = \mathbf{J} + \frac{\partial \mathbf{D}}{\partial t} \tag{2.2}$$

$$\nabla \cdot \mathbf{D} = \rho \tag{2.3}$$

$$\nabla \cdot \mathbf{B} = 0, \tag{2.4}$$

where $\mathbf{E}(\mathbf{r})$ and $\mathbf{H}(\mathbf{r})$ are the respective electric and magnetic fields, whose values depend on a spatial position $\mathbf{r}$. The displacement, $\mathbf{D}$, and magnetic flux, $\mathbf{B}$, are related, respectively, to the electric and magnetic fields through the following relations:

$$\mathbf{D}(\mathbf{r}) = \varepsilon_0 \varepsilon(\mathbf{r}) \mathbf{E}(\mathbf{r}) \tag{2.5}$$

and

$$\mathbf{B}(\mathbf{r}) = \mu_0 \mu \mathbf{H}(\mathbf{r}), \tag{2.6}$$

where μ and ε are the dielectric permittivity and magnetic permeability of the material through which the light passes through.

The electric field term for an electromagnetic wave propagating through a uniform dielectric medium is expressed by the wave equation:

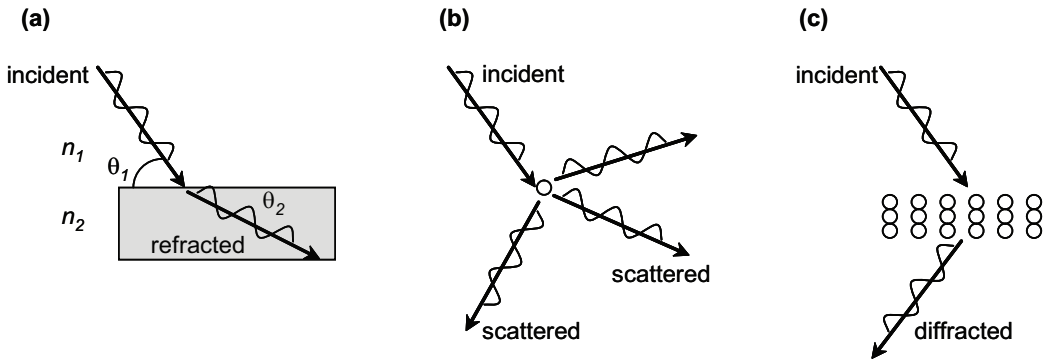

Figure 2.2: Schematic illustrations of (a) refraction (Snell's law), (b) incoherent scattering from a single defect, and (c) optical diffraction (coherent scattering) from a periodic arrangement of defects commensurate with the wavelength of light.

$$\mathbf{E}(r, \omega, t) = E_0 \exp\left[i(kr - \omega t + \delta\right], \tag{2.7}$$

where E_0 is the the amplitude of the transverse electric field for a linearly polarized wave; k is the wave number; ω is the angular frequency; and δ is the phase of light. The wave number $k = 2\pi/\lambda$ is related to the wavelength λ; the angular frequency $\omega = \frac{|k|c}{n}$ is related to the speed of light though a material where c is the speed of light in a vacuum and n is the material's index of refraction.

It is the interaction of EM radiation propagating through both isotropic and anisotropic media that is of particular importance in this thesis. The general principles of refraction (Snell's law), incoherent scattering, and diffraction (coherent scattering) as illustrated in Figure 2.2(a-c), respectively, are all relevant to the work to be discussed.

2.2 Holography

Holograms are often represented in popular culture as three-dimensional free-standing images that appear to hover in space. As the observer's relative orientation changes with respect to the hologram, so too does the perspective of the projected holographic image.

In photography, only the relative intensities of a scene or object are captured on a two-dimensional

photo-sensitive recording film. As a result, all information pertaining to the relative phase of light from one reference point to the next is lost in the photograph.

In contrast, holography captures both the relative intensity and phase of a scene or object on a two-dimensional photo-sensitive recording film. Since most recording media only respond to intensity variations, optical interference from a coherent, monochromatic light source (typically a laser) is used to convert the relative phase information into variations of intensity. The optical interference is created by combining a reference beam having a plane or spherical wavefront along with an object beam scattered from an object to be incident on the photo-sensitive (holographic) recording film, as shown in Figure 2.3(a). The intensity profile at any point on the recorded film is the result of the phase and amplitude information scattered from the object, as represented in Figure 2.3(b). Once the hologram is 'developed,' the interference pattern is permanently recorded in the film. When a reference beam re-illuminates the holographic film, a virtual object is created at the position of the original object with the same characteristics of the original, as shown in Figure 2.3(c).

The two common modes of operation for holographic recording are reflection mode and transmission mode. For the context of this introduction, both modes are introduced; however, this thesis will focus exclusively on transmission mode diffraction gratings recorded using an Ar^+ laser ($\lambda = 351$ nm) on UV photo-sensitive polymers.

2.2.1 Reflection Mode

In reflection mode holography, the object beam and reference beams are split into equal intensity beams and illuminate the holographic recording film from opposite sides at equal angles of incidence. This recording configuration produces a sinusoidal intensity modulation parallel to the surface of the recording medium as a result of the constructive and destructive interference of the reference and object plane wavefronts. The fringe spacing, or grating pitch Λ, is dictated by the Bragg equation:

$$\Lambda = \frac{\lambda}{2n \sin \varphi_w}, \tag{2.8}$$

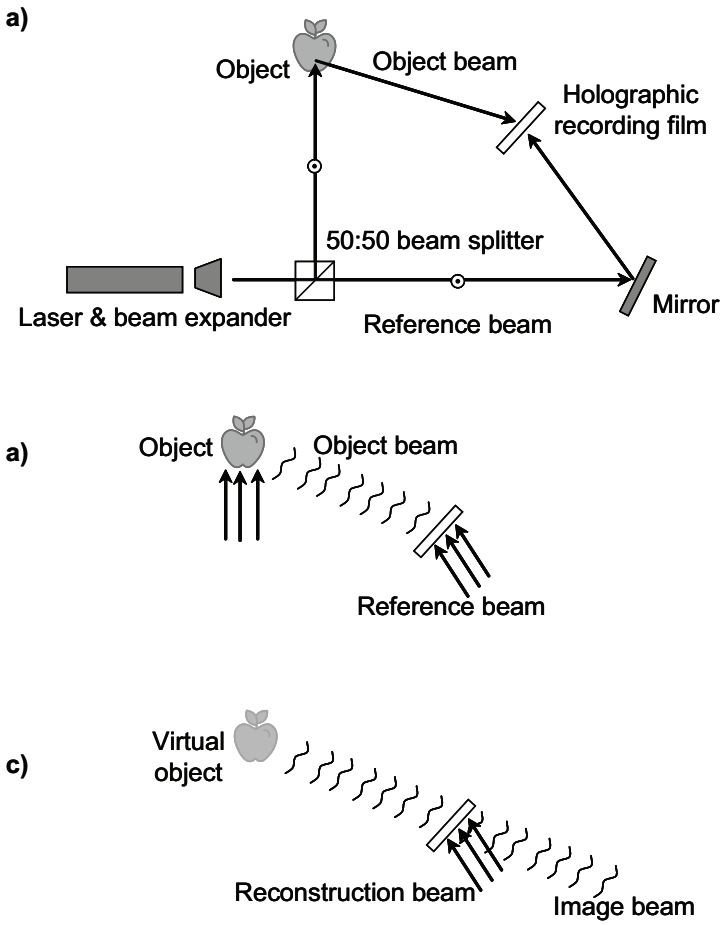

Figure 2.3: (a) A schematic illustration of a two-beam reflection hologram setup, and (b) the corresponding wavefronts for the reference and object beams. (c) In reading the hologram, a virtual image of the original object is reconstructed.

where n is the average refractive index of the holographic recording film; and φ_w is the angle of incidence for the object and reference beam away from the surface normal. A schematic illustration of a reflection mode exposure and interference pattern are shown in Figure 2.4(a).

In this configuration, the holographic recording will Bragg reflect a narrow band of incident light centered around a wavelength, λ_r:

$$\lambda_r = 2n\Lambda \cos\theta_r, \tag{2.9}$$

where θ_r is the reading angle of the grating.

2.2.2 Transmission Mode

In transmission holography, both the object and reference beam recombine on the same side of the holographic recording film to produce a sinusoidal modulation in amplitude (intensity) perpendicular to the surface, as shown as shown in Figure 2.4(b). The spacing of the fringes, or pitch Λ, is also dictated by the Bragg equation. Instead of a narrow band of reflected light, as observed with the reflection mode, the transmission mode creates a visible diffraction pattern with incident light.

2.2.3 Amplitude Modulation

The above mentioned recording modes used two beams having the same polarization state (phase) to create an intensity modulation through the depth of a recording medium. In a two beam exposure, the intensity modulation of a system can be represented by the following equation:

$$I = I_1 + I_2 + 2\sqrt{(I_1 I_2)}\cos\Theta' \cos\left[(k_1 - k_2)\cdot r + \delta\right], \tag{2.10}$$

where I_1, k_1, I_2 and k_2 are the respective intensities and wave numbers for the two beams; Θ' is the angle between the polarization directions; and δ is a phase term. The contrast ratio of the fringes (intensity between brightest and darkest points) can be expressed as:

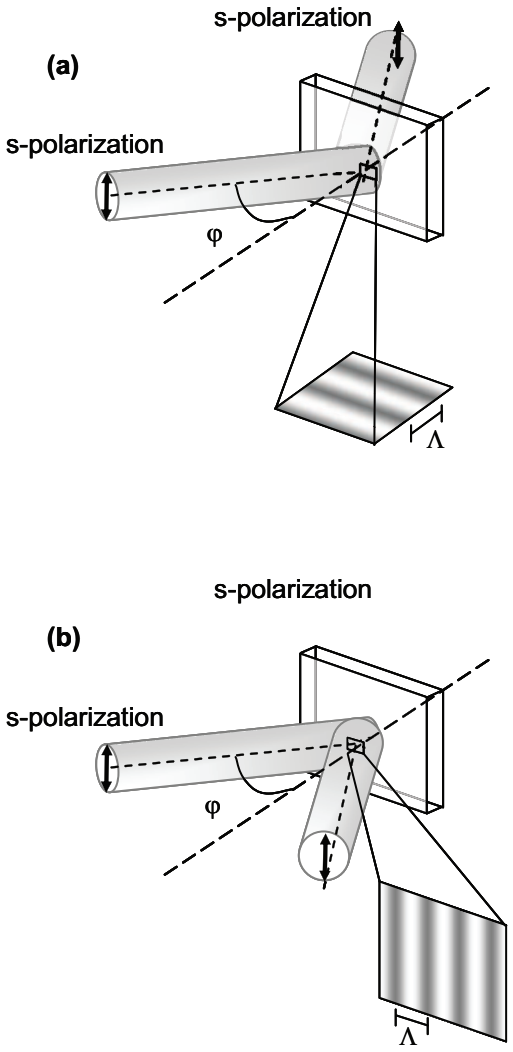

Figure 2.4: Illustration of (a) reflection mode holography and (b) transmission mode holography.

$$\upsilon = \frac{2\cos\Theta'\left(\sqrt{I_1 I_2}\right)}{I_1 + I_2}. \tag{2.11}$$

Thus, a maximum contrast ratio appears when the two beams have equal intensities and $\Theta' = 0$.

2.2.4 Phase Modulation

In addition to amplitude modulations, polarization modulation can also occur in a holographic recording when the reference beam and object beam have orthogonal polarization states. The effects of the phase modulation are most prominent when the beams have orthogonal polarization states – as in the case with orthogonal linear (s- and p-) and orthogonal circular (right- and left-handed) polarizations. Phase modulation can be demonstrated for both transmission and reflection modes, but again for the purposes of this thesis, only the transmission mode will be discussed.

Nikolova and Todorov first recorded a polarization interference pattern from two coherent beams having opposite polarizations on a photo-recordable material [17]. In their first experiment, a polarization interference pattern was recorded using two equal intensity, orthogonal linearly polarized beams with the resulting light field E described by:

$$E = \left| \frac{E\cos\delta}{iE\cos\delta} \right|, \tag{2.12}$$

where δ represents the phase shift between the two beams:

$$\delta = 2(\xi/\lambda)\sin\varphi, \tag{2.13}$$

and is periodic along $\xi; \lambda$ is the wavelength; and φ is the half angle between the two interfering beams. This interference pattern resulted in a uniform intensity with a periodic polarization pattern that varied spatially from $2\delta = 0 \rightarrow 2\pi$ to create linear, elliptical, and circular polarization regions, as shown in Figure 2.5(a).

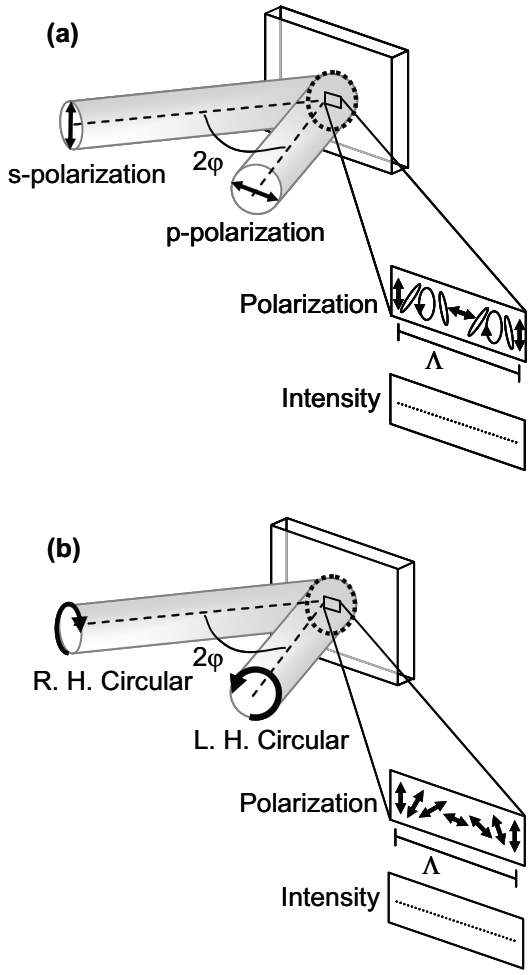

Figure 2.5: Phase modulation resulting from the interference of (a) orthogonal linear and (b) orthogonal circular polarization states.

A second example of polarization holography recorded the interference pattern generated from right- and left-handed circular polarized light with the light field E described by:

$$E = \left| \frac{E\cos\delta}{E\sin\delta} \right|. \tag{2.14}$$

This type of polarization interference generated a uniform intensity with a spatially rotating and periodic linear polarization pattern from $2\delta = 0 \rightarrow 2\pi$, as shown in Figure 2.5(b). It is this polarization grating configuration that will be exploited in Chapters 3 and 4 to establish a periodic alignment of liquid crystal.

2.2.5 Diffraction Grating Regimes

There are two distinct diffraction regimes for one-dimensional gratings, depending on the relationship between the fringe spacing (or pitch Λ) and the thickness of the holographic recording film. The distinction between these two regimes – Bragg and Raman-Nath – can be quantified by a dimensionless parameter Q [18]:

$$Q = \frac{2\pi\lambda_0 d}{n_0\Lambda^2}, \tag{2.15}$$

where λ_0 is the wavelength of light in free space; n_0 is the average refractive index of the film; Λ is the grating pitch; and d is the grating thickness.

The Bragg regime assumes a thick grating where the fringe spacing is much smaller than the thickness of the holographic recording film ($Q \gg 1$). Here, in principle, 100% diffraction efficiency can occur in the first diffracted order.

In contrast, the Raman-Nath regime assumes a thin grating where the fringe spacing is greater than the thickness of the holographic recording film ($Q \ll 1$). For this grating configuration many diffracted orders are present, and a diffraction efficiency of, at best, 33% is achievable.

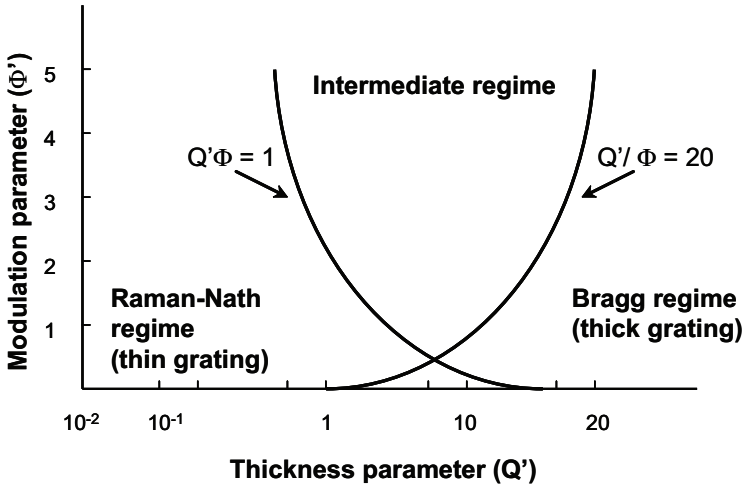

Figure 2.6: Raman-Nath, intermediate and Bragg diffraction regimes for phase holograms. Adapted from Gaylord and Magnusson, 1980.

In cases where a large refractive index modulation occurs in the holographic film, the differentiation between the Bragg and Raman-Nath is not obvious and an intermediate regime appears. To account for the amplitude of the refractive index modulation, an additional dimensionless parameter P' is introduced and defined as:

$$P' = \frac{\lambda_0}{\Lambda^2 n_0 n_1} \tag{2.16}$$

where n_1 is the index modulation. The boundary between the Raman-Nath and intermediate regime corresponds to the curve: $Q'\Phi = 1$, as shown in Figure 2.6, where $Q' = Q/\cos\varphi$ (φ is the angle of incidence within the grating) and the modulation parameter Φ is given by:

$$\Phi = \frac{\pi n_1 d}{\lambda \cos\theta}. \tag{2.17}$$

The boundary between the intermediate and Bragg regime follows the curve $Q'/\Phi = 20$.

2.3 Holographic Recording Materials

A number of holographic recording materials, both organic and inorganic, have been demonstrated for transmission and reflection mode operation – responding to amplitude and/or phase modulation. This section serves as an introduction to only some of the organic (polymeric) materials useful in holographic gratings.

2.3.1 Holographic Polymer Dispersed Liquid Crystals

In order to fully describe the embodiments of holographic polymer dispersed liquid crystals (H-PDLCs) it is necessary to first describe the formation and operation of 'conventional' polymer dispersed liquid crystals (PDLCs).

The chemistry of PDLC systems typically involves an emulsification or photo-induced phase separation (PIPS) process of a homogeneous mixture of liquid crystal and curable monomer sandwiched between two pieces of indium tin oxide (ITO) coated glass. The uniform thickness of the mixture is maintained though the use of glass fiber spaces, while the ITO coatings on the inner glass surfaces serve as transparent conducting electrodes.

In photo-curable PDLC systems a blanket exposure illuminates a homogeneous mixture and initiates a polymerization reaction to induce a photo-induced phase separation process. During this process, the reactive monomeric units begin to polymerize, forcing the liquid crystal to counter-diffuse into micrometer-sized droplets embedded in the polymer network. The size of the droplets is controlled by the rate of polymerization.

The basic operation of a PDLC relies on a refractive index mismatch between the polymer n_p, and the liquid crystal (n_{LC}). The index of refraction for the liquid crystal droplets is a combination of the ordinary (n_o) and extraordinary (n_e) indices of refraction, often estimated by:

$$n_{LC} = \left[\frac{n_e^2 + 2n_o^2}{3}\right]^{\frac{1}{2}}. \tag{2.18}$$

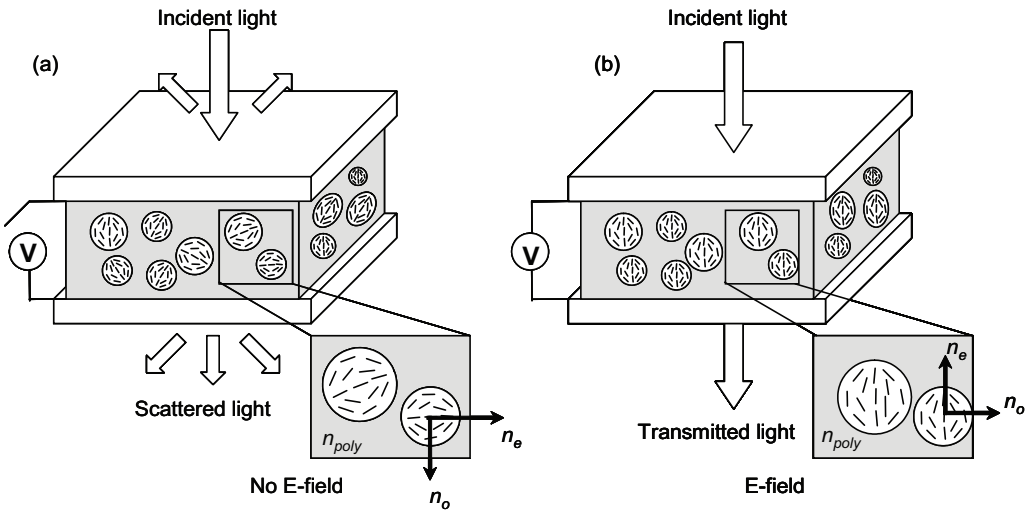

Figure 2.7: A PDLC in (a) the scattering state at $V = 0$, and (b) the transparent state $V > V_c$.

These thin films will respond to an electric field applied across the transparent conducting electrodes. Without the application of an electric field, incident light is scattered as it passes through the PDLC film, due to the index mismatch between n_p and n_{LC}; the film appears milky-white to the observer. This scattering state at $V = 0$ is illustrated in Figure 2.7(a). When an electric field is applied across the PLDC film, the liquid crystal droplets will align parallel to the electric field, due to the positive dielectric anisotropy ($\varepsilon > 0$) of the molecules. In this state, incident light experiences an index matching between n_p and n_o, making the film optically transparent above some critical voltage $V > V_c$, as depicted in Figure 2.7(b).

Holographically formed polymer dispersed liquid crystals (H-PDLCs) are the successors to conventional PDLCs, and are created through a photopolymerization-counter diffusion process initiated by interfering coherent laser beams. By exposing the prepolymer and liquid crystal mixture to an amplitude interference pattern, the intensity modulation induces a rapid polymerization of the monomer in the high intensity regions and forces out the liquid crystal to the lower intensity regions, producing stratified dispersions of alternating polymer rich and liquid crystal rich planes. The spacing (or pitch Λ) of these alternating planes is determined by the Bragg equation, shown previously in Equation 2.8.

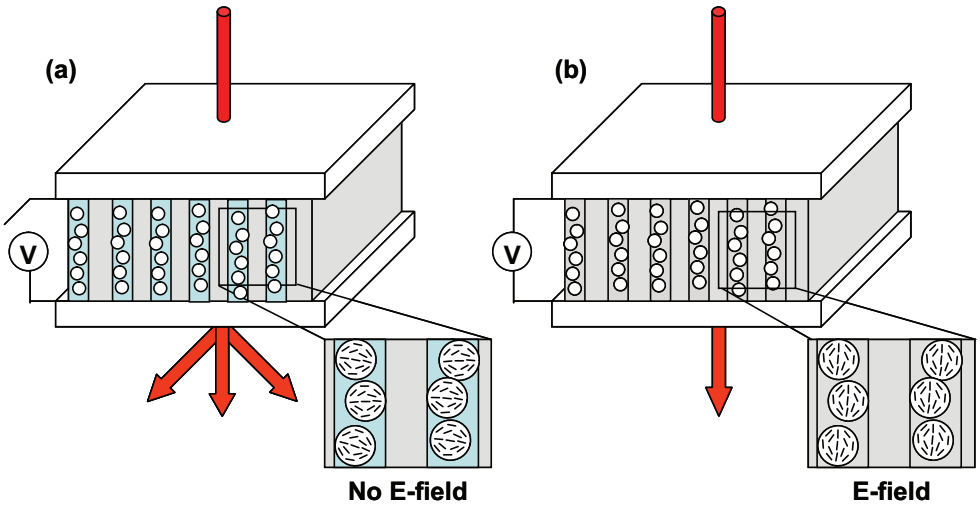

Figure 2.8: A transmission mode H-PDLC grating at (a) $V = 0$, and (b) $V > V_c$.

The operation of a transmission mode H-PDLC film with alternating planes perpendicular to the glass substrates is shown in Figure 2.8(a). With a laser source incident on the periodic variation in the refractive index from that of the liquid crystal to the polymer, a visible diffraction grating is created, as shown in Figure 2.8(a). Upon application of an electric field to this same film, as shown in Figure 2.8(b), the liquid crystal droplets align parallel to the electric field direction (assuming $\varepsilon > 0$). In this case, $n_p \sim n_o$, and both polarizations propagate directly through the now optically equivalent regions, without experiencing a diffraction pattern.

Reflection mode H-PDLCs are formed through the same photopolymerization and counter diffusion mechanisms as transmission mode H-PDLCs. By using an amplitude interference pattern where the beams interfere from opposite sides of the sample (as opposed to the same side as in the transmission mode), the alternating planes of liquid crystal and polymer are formed parallel to the glass substrates in the reflection mode. Illuminating a reflection mode H-PDLC with a broadband white light source induces a coherent Bragg reflection that is rejected due to the index mismatch between n_{LC} and n_p at $V = 0$. A schematic illustration of a reflection mode H-PDLC at $V = 0$, depicting a green reflection notch is shown in Figure 2.9(a). By a applying sufficiently strong electric field across the film, the liquid crystal molecules align parallel to the direction of the electric field

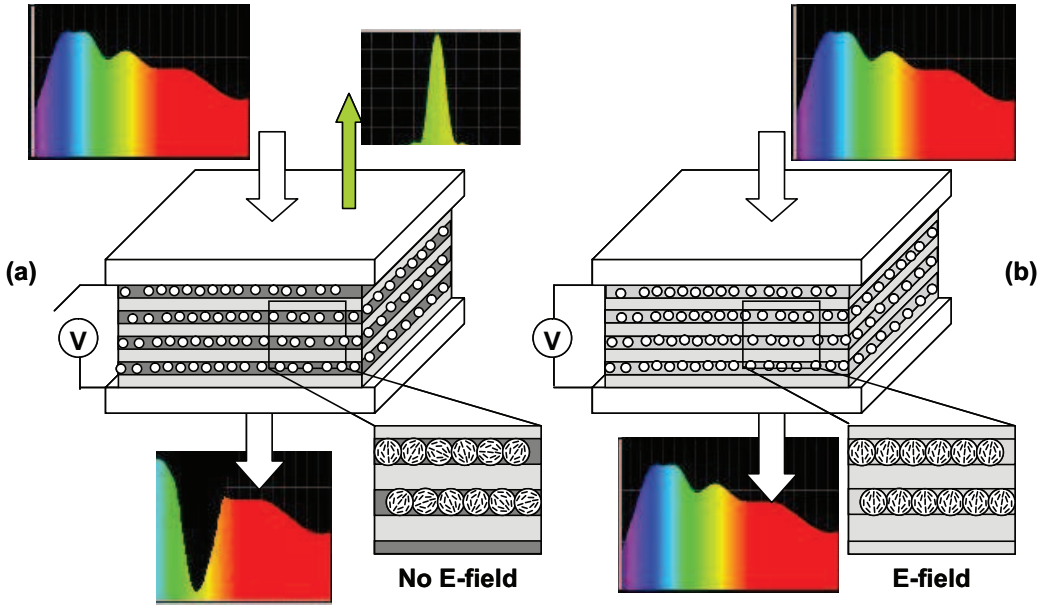

Figure 2.9: A reflection mode H-PDLC grating at (a) $V = 0$, and (b) $V > V_c$.

(assuming $\varepsilon > 0$), and create a refractive index match between the liquid crystal (n_{LC}) and the polymer (n_p), making the film optically transparent for all wavelengths, as shown in Figure 2.9(b). Typical bandwidths ($\Delta\lambda$) for the reflection notch at $V = 0$ are around $15 - 30$ nm depending on the film thickness, birefringence of the liquid crystal (Δn) and index of refraction of the polymer (n_p).

In addition to one-dimensional reflection and transmission mode H-PDLCs, more complicated LC and polymer grating structures can be fabricated using three or more coherent beams incident on the sample, including two- and three-dimensional square lattices, face centered cubic lattices, diamond lattices, and five-, seven-, and nine-fold quasi-crystal structures.

2.3.2 Azo-dyes

Azo-benzene dye molecules selectively respond to both the amplitude and phase of incident light and undergo photo-isomerization and reorientation in the presence of linearly polarized light. Depending on the wavelength sensitivity of the azo-dye molecules, the functional units can undergo a reversible conformation change from a transoid longitudinal state to a cisoid state, in UV or visible light,

due to the material's selective absorption along the molecular axes. These types of molecules are attractive as temporary holographic recording media for amplitude or phase holography, since the isomerization and reorientation are energetically stable only in the presence of the illumination.

By using azo-dyes as dopants in liquid crystal-based systems, the isomerization and reorientation directs a liquid crystal alignment parallel to the long axis of the azo dye. In the example of phase holography, using orthogonal circular polarizations to generate the interference pattern, the polarization modulation is captured during illumination, which causes the azo-dye and liquid crystal to align perpendicular to the incident polarization direction. Through material optimization, including the addition of surface alignment treatments, the stability of these configurations have been prolonged to create semi-permanent one- and two-dimensional grating structures.

2.3.3 Photopolymerizable Polymers

Linear photopolymerizable polymer (LPP) materials are useful as alternative, non-contact approaches for creating pattered liquid crystal alignment using lithographic exposure techniques. This material, which undergoes a dimerization of two coumarin molecules 'responds' to both the phase and amplitude of incident UV light sources and selectively induces a planar alignment parallel to the incident linear polarization direction. The molecular structures before and after the dimerization are shown in Figure 2.10. For this reason, it is a natural transition to also consider these materials for use in amplitude and phase holographic exposures. In the example of an amplitude interference, the high intensity regions will selectively polymerize the LPP material parallel to the direction of the incident polarization and induce a planar LC alignment in the same direction. Consequently, the low intensity regions of the amplitude interference pattern will not polymerize, causing the LC to be randomly oriented in these regions. The resulting grating structure is a planar-random alignment [19].

Instead of using amplitude modulation to selectively polymerize the LPP layer, polarization modulation can also be used – in particular the interference pattern created from orthogonal circular

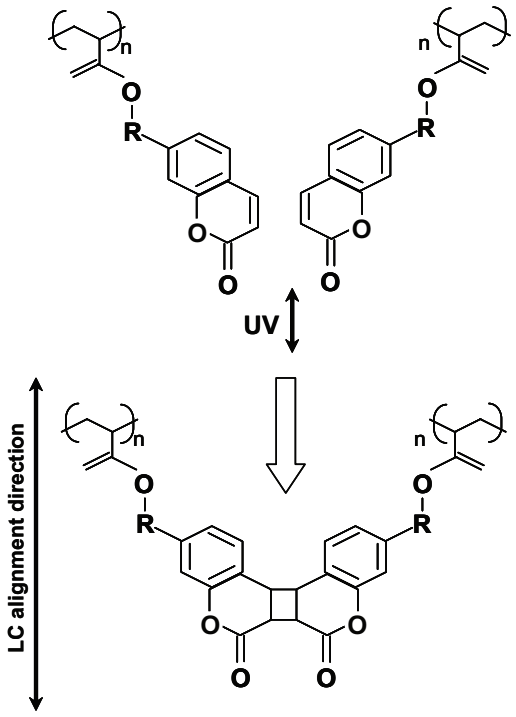

Figure 2.10: Molecular structure of two coumarin molecules and the dimerization reaction that occurs during irradiation with UV light. The director of the induced LC planar alignment is also shown.

polarizations. Gratings of this type will be described in detail in Chapters 3 and 4.

2.4 Summary

An introduction to electromagnetic radiation in isotropic and periodic media was presented in the context of holography and diffraction gratings. The different recording modes and diffraction regimes were also introduced, along with examples of holographic recording materials. Chapters 3 and 4 will present studies on pattered liquid crystal diffraction gratings using a linear photopolymerizable polymer alignment layer exposed to orthogonal right-handed and left-handed circular polarizations. Amplitude transmission mode H-PDLCs using ferroelectric liquid crystals will be presented in Chapter 5.

Chapter 3

One-dimensional Photoalignment Gratings

The patterning of surfaces for aligning liquid crystal materials has received a significant degree of attention by scientists and engineers, driving the creation of a plethora of hybrid geometries and multi-domain configurations for wide angle viewing liquid crystal displays, projection displays and photonic devices for optical communications. A number of materials and techniques have been employed using polyimide alignment layers or photosensitive materials to create multi-domain configurations for liquid crystal systems exhibiting unique electro-optic behavior compared to the well-described single domain liquid crystal alignment typically imposed by a polyimide layer. Here, we focus on planar-periodic boundary conditions used to create various types of optical gratings, including polarization gratings, which are diffractive optical elements with an anisotropic periodic index profile [11, 14, 20–23]. The disclosed polarization gratings are 'thin' gratings and the thin screen approximation predicts complete diffraction into the first diffraction orders, thus making them attractive for optical devices [23, 24]. These gratings have numerous applications in photonic systems and displays, including highly efficient projection displays, wide viewing and direct view

displays, polarized beam splitting devices, multiplexing and polarization dispersion applications. The structure of a number of gratings formed using polarization holography for liquid crystal alignment are here investigated.

The field of patterning surface alignment layers for liquid crystals is vast. Varghese and co-workers have demonstrated a four-domain liquid crystal alignment using a micro-rubbing technique on homeotropic polyimide that allows for expanded viewing angles in full color displays [7, 8]. Chen and co-workers have shown a hybrid liquid crystal configuration (combining planar and twist regions) using photolithography to create a double-rubbed polyimide layer for a high efficiency, polarization independent grating [6]. Honma and co-workers have demonstrated liquid crystal gratings consisting of multidomain alignment regions fabricated through a micro-rubbing technique [9, 10]. Versteeg and co-workers have applied direct laser writing methods to melt polyimide regions to form multi-domain configurations of planar and twisted alignment [25]. Wen and co-workers have shown a dual domain polarization grating configuration fabricated by scribing a polyimide layer with an atomic force microscope tip to produce right- and left-handed twist regions [14]. Komitov and co-workers have demonstrated a uniform lying helix (ULH) alignment for short pitch cholesteric liquid crystals using periodic planar and homeotropic anchoring conditions [21]. Additionally, Rosenblatt and co-workers have published extensive results on the anchoring effects, surface roughness and electro-optic dynamics associated with liquid crystal alignment on atomic force microscopy scribed polyimide surfaces [11, 22, 26].

In addition to modifying polyimide coated surfaces to manipulate the surface alignment of liquid crystals, photosensitive layers have been demonstrated as non-contact methods for establishing multi-domain configurations. Schadt and co-workers demonstrated a four domain twisted nematic display, which exhibits wide angle viewing characteristics, using a coumarin based photo-prepolymer layer with polarized ultraviolet irradiation [13]. Gibbons and co-workers have demonstrated a method of creating a liquid crystal grating by exposing a dye-doped polymer layer to an ultraviolet interference pattern to create periodic regions of planar and twist alignments [12]. Lee and

Clark have functionalized a self assembled monolayer (SAM) to create hybrid regions of planar and bend alignments upon irradiation with non-polarized ultraviolet light [27].

The creation of periodic boundary conditions for liquid crystal materials using a linear photopolymerizable polymer (LPP) surface layer exposed to a polarization interference pattern is discussed here. Unlike amplitude holography, which uses two interfering beams of the same polarization to create an intensity modulation, as shown in Figure 3.1(a), polarization holography uses two interfering beams of orthogonal linear or orthogonal circular polarizations to create polarization modulations as shown in Figure 3.1(b) and 3.1(c), respectively [17]. When creating polarization interference patterns, as in Figure 3.1(b) and 3.1(c), the intensity of the incident light is constant, or nearly constant, for certain exposures. The pitch of the formed interference patterns, Λ, is also defined in Figure 3.1. Although Figure 3.1(c) shows that ideally no intensity modulation exists, one is in fact present in real systems. Cloutier and coworkers have shown that if the exposure angles are small, as in the case of the gratings to be discussed, the intensity interference pattern is very weak [28].

Here we employ the arrangement shown in Figure 3.1(c). The holographic exposure of the LPP in this configuration polymerizes the material in the incident polarization direction and creates planar-periodic boundary conditions of liquid crystal in the plane of the substrate. The photo-chemical mechanism by which such an alignment is achieved is analogous to that reported by Schadt and co-workers [13]. Using this holographic polarization alignment pattern on a pair of substrates we have created a rotating planar alignment configuration of liquid crystal registered between the top and bottom substrates. Furthermore, we have combined the holographic polarization alignment pattern with conventional, non-periodic alignment layers to enforce uniform planar or homeotropic conditions on one of the two substrates.

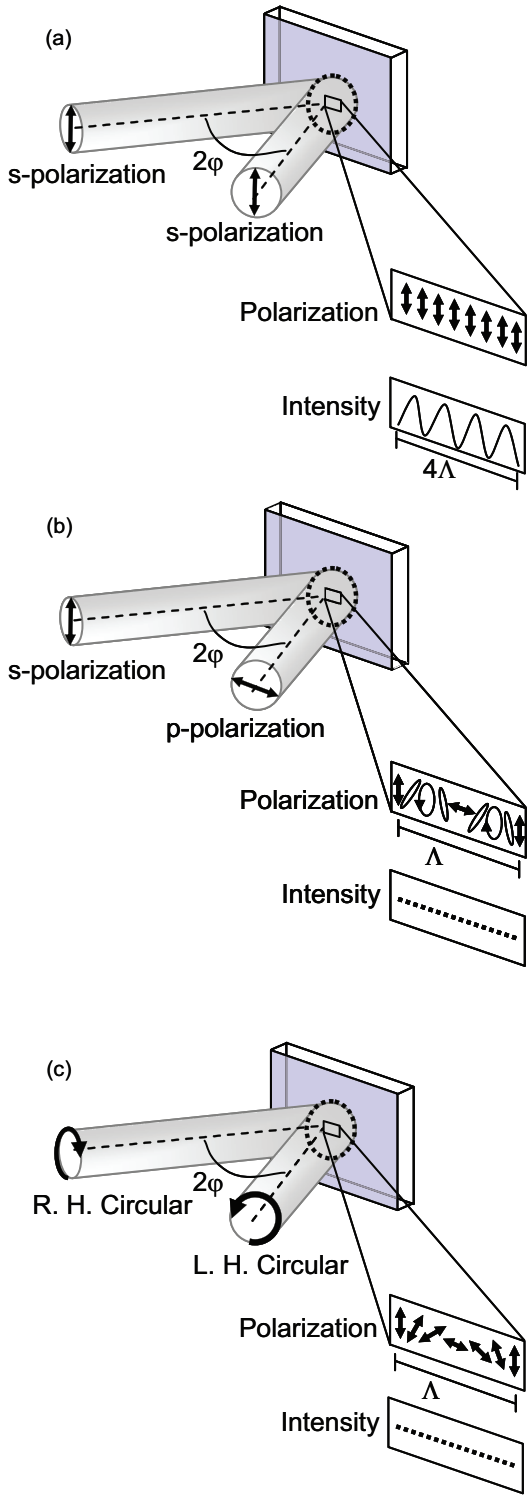

Figure 3.1: Schematic illustrations of (a) an amplitude holographic exposure using linear s-polarization, (b) a polarization holographic exposure using orthogonal s- and p-polarizations, and (c) a polarization holographic exposure using right- and left-handed circularly polarized beams. In all three cases Λ is used to denote the grating pitch.

3.1 Materials Preparation

The linear photopolymerizable polymer (LPP F301), commercially available from ROLIC (*ROLIC Ltd*, Allschwil, Switzerland), was used as a photosensitive alignment layer. It was spin coated on indium tin oxide (ITO) coated glass substrates resulting in a uniform film thickness of ∼100 nm. After spin coating, the substrates were thermally treated on a hotplate at 150 °C for 15 minutes to remove the residual solvent from the alignment layer. Cell configurations were prepared by sandwiching two substrates together with the alignment layers facing each other; a cell gap of 5 μm was maintained by glass fiber spacers (*EM Industries*, Hawthorne, NY). A single holographic exposure with an Ar^+ laser (Innova 70, Coherent, Santa Clara, CA), emitting at $\lambda = 351$ nm, was used to create a two-beam transmission interference pattern; the beams had equal intensity and orthogonal circular polarizations and resulted in the spatially rotating linear polarization pattern. After exposure to the interference pattern, the liquid crystalline material was infiltrated into the empty cell by capillary action at an elevated temperature (above the nematic-isotropic transition temperature) and cooled to room temperature under ambient conditions. By sandwiching the substrates together prior to the holographic exposure, a liquid crystal grating structure was formed by the periodic boundary conditions registered on both substrates.

Liquid crystal gratings were also created using hybrid boundary conditions. These cell configurations were prepared using one LPP polarization patterned ($\Lambda = 7.5$ μm) ITO coated glass substrate and one polyimide and ITO coated glass substrate. Commercially available polyimide precursors were used (Nissan SE-2170 and Nissan SE-1211, *Brewer Science*, Rolla, MO) to promote planar and homeotropic alignments. The planar polyimide material was spin coated and then cured in an oven to achieve a film thickness of ∼200 nm. After curing, the planar polyimide coated substrate was mechanically rubbed with a velvet wheel to achieve a uniform planar alignment in the rubbing direction. The homeotropic polyimide material was spin coated and then cured in an oven to achieve a uniform film thickness of ∼100 nm. Following the exposure of the LPP coated substrate to the

polarization interference pattern, the hybrid cell fabrication was completed by sandwiching the LPP polarization patterned ITO glass and polyimide coated ITO glass separated by 5 μm glass fiber spacers. In the hybrid configurations it was not necessary to sandwich both substrates together prior to the holographic exposure since the boundary conditions on the two substrates did not require registration. Liquid crystal (MLC-6292-100, *EM Industries*, Hawthorne, NY) was again filled by capillary action into these empty cells at an elevated temperature and subsequently cooled to room temperature under ambient conditions.

Planar periodic boundary conditions were also used to align reactive mesogen materials. These grating configurations were prepared by using one LPP polarization patterned glass substrate with a liquid crystal polymer (LCP) (LCP CB 483, *ROLIC Ltd*, Allschwil, Switzerland) coated on the substrate using a Meyer rod after the holographic exposure. Prior to polymerization the LCP material exhibited similar surface alignment characteristics as a low molecular weight liquid crystal material. Polymerization with UV light was used to permanently 'capture' the order of the liquid crystal phase in a polymer form. This particular reactive mesogen was chosen as it was developed to work well with the LPP material.

To summarize, several processes were used to fabricate polarization gratings using both low molecular weight liquid crystal and liquid crystal polymer. The gratings formed using registered planar-periodic boundary conditions will, in principle, exhibit a larger refractive index modulation due to the continuous spatial rotation of the alignment. This may enhance their electro-optic properties and functionalities for potential devices. The hybrid configurations will exhibit a lower refractive index modulation, caused by the constraints of the boundary conditions, but may be applicable for specific device applications if larger refractive index modulations are not necessary.

3.2 Nematic Grating Configurations

The following sections describe, in depth, one-dimensional grating configurations using nematic LCs and a two-beam holographic exposure. One-dimensional smectic LC gratings will be presented in Chapter 4, along two-dimensional nematic LC gratings using a four-beam holographic exposure.

3.2.1 Registered Planar Periodic Boundary Conditions

An optical polarizing microscopy image of a liquid crystal polarization grating ($\Lambda = 7.5$ μm) between crossed polarizers is shown in Figure 3.2, where n defines the liquid crystal director. The anchoring conditions of the LPP alignment layer create a uniform grating configuration without defects. The dark grating lines indicate regions where the liquid crystal is oriented at 0° or 90° with respect to the polarizer (P) or analyzer (A), while the lighter regions indicate where the liquid crystal is aligned at some other angle between the polarizer and analyzer. A schematic illustration of the top and cross sectional views showing the anchoring alignment imposed by the polarization patterned surfaces is also shown in Figure 3.2. Because the top and bottom patterned surfaces are registered during exposure, the planar alignment propagates unperturbed through the depth of the cell and results in a uniform alignment throughout its volume. As will be shown later, the propagation of the liquid crystal alignment through the entire depth of the cell can only occur if the grating pitch is comparable or larger than the cell gap ($\Lambda \geq d$).

3.2.2 Periodic-Planar – Planar Boundary Conditions

The hybrid configuration of a uniformly rubbed planar substrate and LPP polarization patterned substrate resulted in a hybrid structure of alternating regions of planar and twist alignment. The pitch of the planar-periodic boundary condition was $\Lambda = 7.5$ μm. An optical polarizing microscopy image taken between crossed polarizers of this hybrid configuration is shown in Figure 3.3.

Regions where the polarization direction of the LPP coated substrates was aligned parallel to

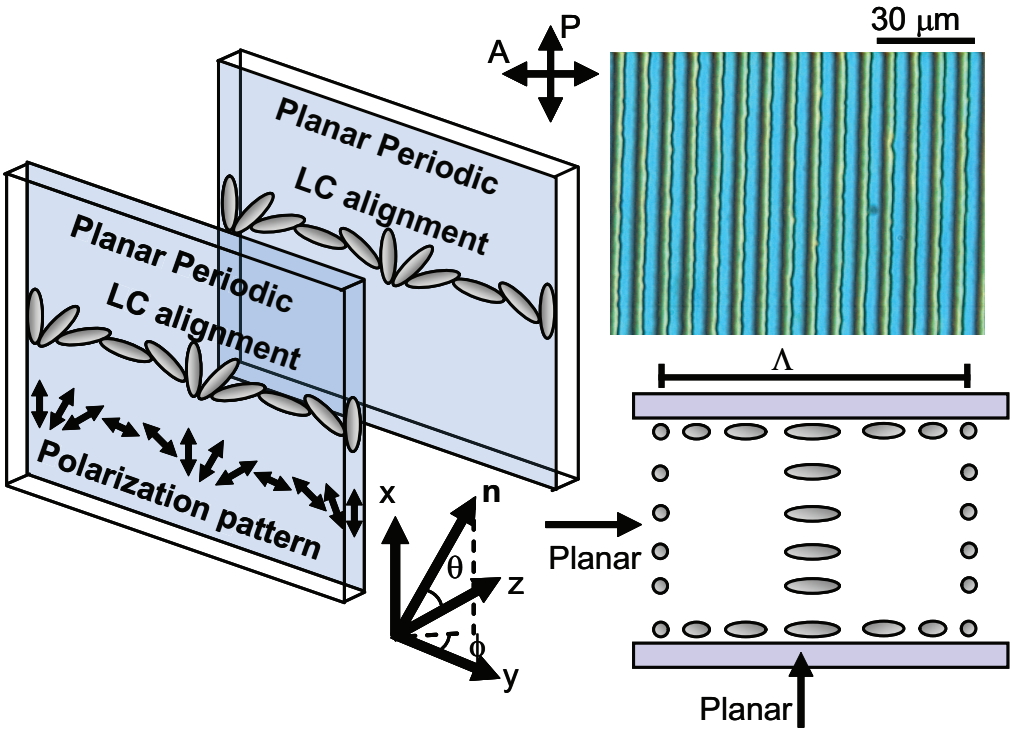

Figure 3.2: Schematic illustration showing the liquid crystal alignment created by two registered planar-periodic boundary conditions. The coordinate system shown here was used for expressing the director orientation in the free energy equation. An optical polarizing microscopy image of this grating configuration is shown between crossed polarizers. An illustration also depicts the cross-sectional view of the periodic director orientation.

the rubbing direction of the polyimide coated substrate resulted in a planar alignment of the liquid crystal propagating through the depth of the cell. These areas are the thick, dark grating lines in the optical polarizing microscopy image in Figure 3.3. Schematic illustrations showing the surface and cross sectional hybrid alignment views are also presented.

Regions where the polarization direction of the LPP coated substrates were aligned at some angle ($< 90°$) with respect to the rubbing direction of the polyimide coated substrates resulted in a continuous twist alignment ($< 90°$) of the liquid crystal through the depth of the cell. These areas appear as light grey grating lines in the optical polarizing microscopy image due to the adiabatic waveguiding of light in the twist configuration. Because of the continuous and rotating nature of the polarization pattern, the amount of twist spatially varies across the grating pitch between $0°$ and $90°$, as observed by the grey levels in the optical polarizing microscopy image.

Defect lines are also present in this configuration due to a competition between twisting directions in the cell. The planar-periodic boundary conditions imposed by the polarization patterned alignment layer and polyimide alignment layer create an inherent twist sense as described earlier. These acutely twisted regions exhibit both right-handed and left-handed twist directions, which 'collide' in the region where the liquid crystal alignment imposed by the planar polyimide boundary condition is orthogonal to the liquid crystal alignment imposed by the polarization patterned boundary condition. Instead of forming a complete $90°$ twist, a sharp defect line is observed, appearing as a dark line within a white grating line. Because of a competition between the right-handed and left-handed twist domains, it is not possible to suppress the appearance of the defect line for this particular hybrid geometry.

3.2.3 Periodic-Planar – Homeotropic Boundary Conditions

The hybrid configuration from the homeotropic polyimide boundary conditions on one substrate and planar-periodic boundary condition on the other results in a structure combining periodic regions of different bend geometries. This is a defect-free configuration because the periodic regions do not

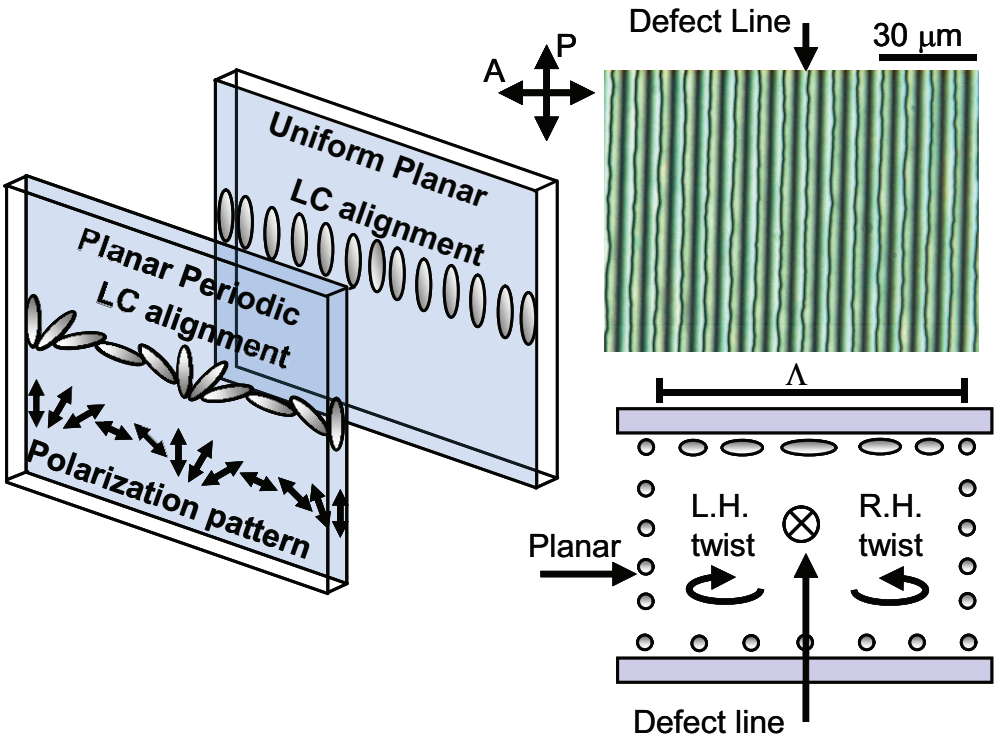

Figure 3.3: Schematic illustration showing the liquid crystal alignment created by planar-periodic and planar boundary conditions. An optical polarizing microscopy image of this grating configuration is shown between crossed polarizers. An illustration also depicts the cross-sectional view of the periodic director orientation showing the planar and competing right-handed and left-handed twist configurations with a line defect.

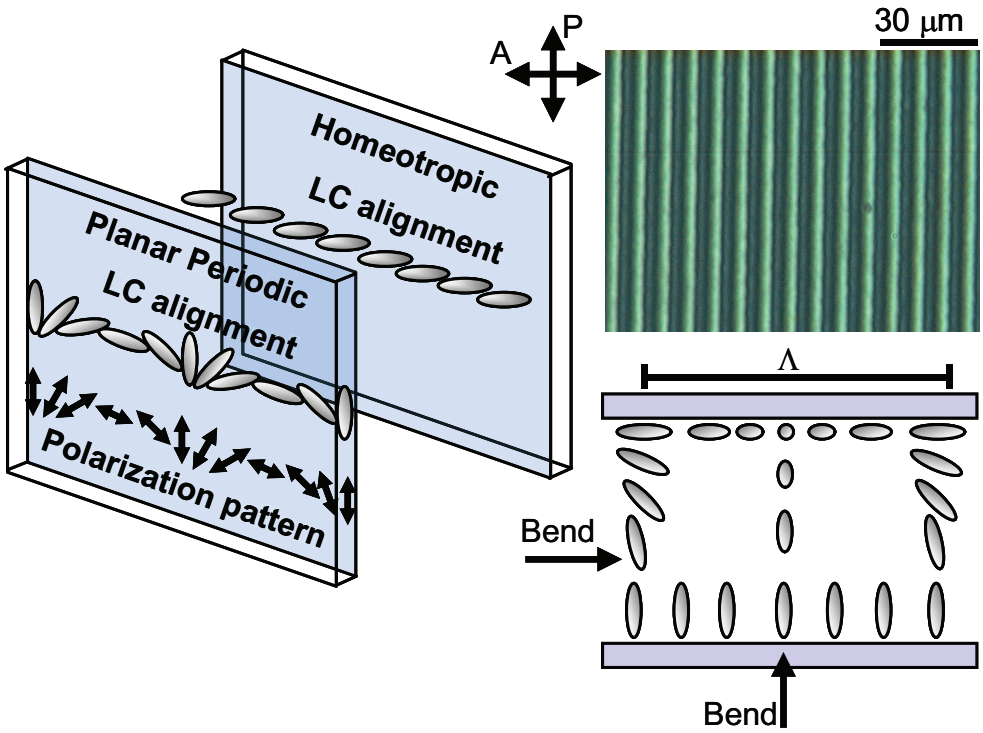

Figure 3.4: Schematic illustration showing the liquid crystal alignment created by planar periodic and homeotropic boundary conditions. An optical polarizing microscopy image of this grating configuration is shown between crossed polarizers. An illustration also depicts the cross-sectional view of the periodic director orientation showing the various bend configurations.

generate a frustrated liquid crystal alignment within the cell.

An optical polarizing microscopy image of this structure between crossed polarizers is shown in Figure 3.4. These bend structures appear as a grating texture due to the periodic and spatially rotating planar alignment established by the planar periodic boundary conditions. The darker grating lines in the microscopy image represent bend regions where the planar aligned liquid crystal is at 0° or 90° with respect to the polarizer or analyzer. Lighter gray grating lines represent bend regions where the planarly aligned liquid crystal is at some other angle with respect to the polarizer and analyzer. Schematic illustrations of the alignment surfaces and cross sectional views of the cell are also illustrated in Figure 3.4.

3.3 Electro-optic Results

3.3.1 Polarization Dependence

The polarization dependence of the hybrid configurations was investigated using a helium-neon laser illuminating the patterned area of the cell at normal incidence, while a photo-detector connected to a wide band amplifier and digital multimeter recorded the first order diffracted intensity. The first order diffraction intensity was measured as a function of incident linear polarization in 10° increments, with 0° representing incident s-polarization (polarization direction perpendicular to the grating vector) and 90° representing incident p-polarization (polarization direction parallel to the grating vector).

Plots of the first order diffraction intensity as a function of the incident linear polarization direction for the three cell configurations are shown in Figure 3.5. Results show there exists a slight polarization dependence for the patterned surfaces. The plot in Figure 3.5 shows the increase in diffracted intensity as the linear polarization is rotated from incident s-polarization (0°) to p-polarization (90°). Overall the ratio in intensity between these polarizations states is ∼3:1, which demonstrates the presence of a slight polarization dependence. This property may be attributed to the existence of a small amplitude grating formed during exposure, a quality observed in other polarization grating technologies using azo-dye doped photo-resist [28]. The first order diffraction efficiency was measured for a single patterned substrate (without any liquid crystal) for incident s-and p-polarization. The first order diffraction efficiency for incident s-polarization was ∼0.06 and ∼0.08 for p-polarization, confirming the holographic exposure creates a small refractive index modulation in the LPP film itself.

In comparison, the hybrid configuration formed with the polarization patterned LPP and planar polyimide coated substrates shows no dependence on the incident polarization as it is rotated from 0° to 90°, as shown in Figure 3.5. The diffracted intensity remains constant, thus creating a completely polarization independent grating. This is attributed to a refractive index modulation

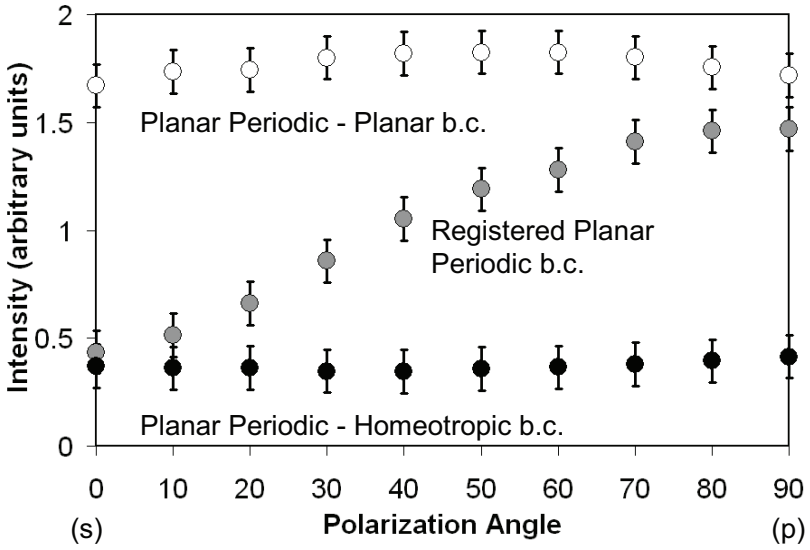

Figure 3.5: A plot of polarization dependence measuring the first order diffraction intensity as a function of incident linear polarization for each of the hybrid configurations, where (gray circles) are the configuration formed from two registered planar-periodic boundary conditions, (white circles) are the hybrid configuration formed from the planar-periodic and planar boundary conditions, and (black circles) are the hybrid configuration formed from planar-periodic and homeotropic boundary conditions. In this plot 0° represents s-polarization and 90° represents p-polarization.

between the planar and twist alignment regions independent of the incident polarization direction. Regardless of the incident linear polarization direction, the refractive index modulation will be the difference between the extraordinary ($n_e = 1.5991$) and ordinary ($n_o = 1.4845$) indices of refraction for the liquid crystal, due to the periodic and orthogonal alignment configuration established by the boundary conditions.

The hybrid configuration formed from the polarization patterned LPP and homeotropic polyimide coated substrates also shows no dependence on the polarization as it is rotated from 0° to 90°. The measured diffracted intensity is less than the hybrid configuration using planar polyimide, due to a lower refractive index modulation in the grating caused by the bend configuration. For incident s- or p-polarizations the index modulation between alternating bend configurations is the difference between an effective (n_{eff}) index and the ordinary (n_o) index for the liquid crystal. The effective index (n_{eff}) can be defined as

$$n_{\text{eff}} = \frac{1}{d}\int_0^d \frac{n_o n_e}{{n_o}^2 \cos\theta(z) + n_e^2 \sin\theta(z)} dz, \tag{3.1}$$

where d is the thickness of the cell; n_o and n_e are the ordinary and extraordinary indices of refraction for the liquid crystal; and $\theta(z)$ is the angle between the nematic director and the x-y plane. The effective index can be approximated as $\sqrt{n_e n_o}$ to give $n_{\text{eff}} = 1.5407$, for the LC used (MLC-6292-100), which supports a lower index modulation ($n_{\text{eff}} - n_o = 0.0562$) as compared to the other two configurations.

3.3.2 Dynamic Switching of Registered Planar-Periodic Cells

The electro-optic switching behavior was investigated for the three hybrid configurations with identical grating pitches and thicknesses ($\Lambda = 7.5$ μm, $d = 5$ μm). A 1 kHz square wave was applied across the cells while a helium-neon laser probed the films and a photodetector measured the changes in the first order diffraction intensity as a function of voltage. A plot of the first order diffraction as a function of voltage for the cell configuration with periodic boundary conditions is shown in Figure 3.6, with a threshold voltage of 1.4 V. The shape of the first order diffraction vs. voltage curve indicates that as voltage is increased to 2 V the liquid crystal alignment in the field essentially erases the index modulation. A 10% first order spot persists slightly above 2 V. Above 2 V, the diffraction intensity begins to grow again. As can be observed in the microscopy images (see inset in Figure 3.6), the grating again becomes more visually prominent at 3 V, before disappearing at 10 V.

The phenomenon observed in Figure 3.6 is speculated to be the result of reverse tilt disclinations arising from the absence of pretilt. At 3 V a very strong grating reappears with distinct boundaries between the adjacent domains. Mote Carlo simulations of the process should well model these phenomena. The calculations involving these structures are not trivial, especially when surface tilt angles are included. Response times (on and off) were also measured using a 10 V modulated square

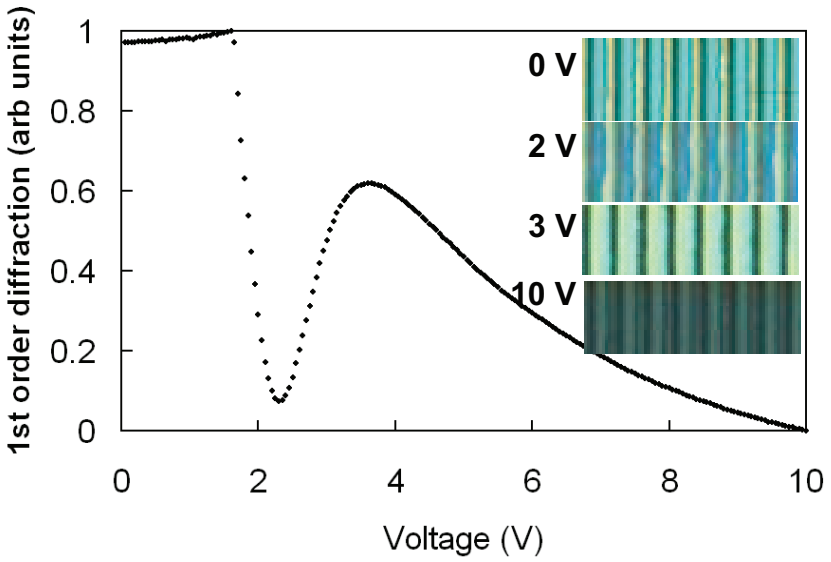

Figure 3.6: A plot of first order diffraction vs. voltage for a grating formed from two registered planar-periodic boundary conditions; the threshold voltage occurs at 1.4 V ($\Lambda = 7.5$ μm, $d = 5\mu$m). The inset shows optical polarizing microscopy images of the registered planar periodic boundary condition cell taken at 0, 2, 3 and 10 V.

wave applied across the sample; on-times were measured to be 4 ms ($\pm$0.2 ms) with relaxation times of 8 ms ($\pm$1 ms). The pitch-to-cell gap ratio was not optimized; therefore, the diffracted efficiency of the first order peak was only $\sim$8%. Using the thin screen approximation, the pitch-to-cell gap ratio could be optimized to achieve a complete diffraction efficiency [23, 24].

3.3.3 Dynamic Switching of Hybrid Cells with Planar-Periodic – Planar Boundary Conditions

The first order diffraction versus voltage curve for the hybrid planar – planar-periodic configuration (planar-twist) is shown in Figure 3.7. This configuration has a threshold voltage of $\sim$1 V. As the voltage is increased to 2 V the liquid crystal begins to untwist and align in the field; the increased diffraction intensity is attributed to a larger index modulation for this partially aligned state. The planar regions of this configuration have a lower threshold voltage than the twisted regions. Therefore, as observed under the microscope, (see inset of Figure 3.7), the planar regions

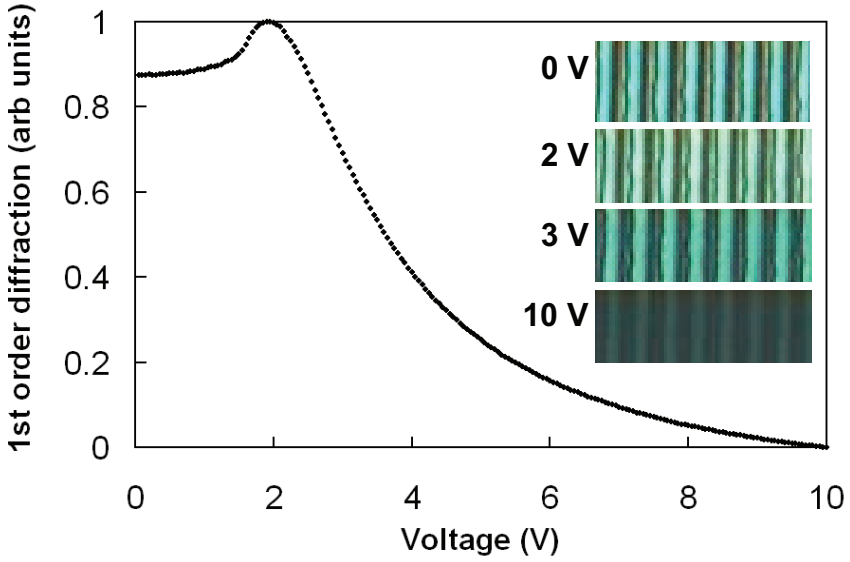

Figure 3.7: A plot of first order diffraction vs. voltage for a grating formed from planar periodic and planar boundary conditions; the threshold voltage occurs at 1.0 V ($\Lambda = 7.5$ μm, $d = 5$ μm). The inset shows optical polarizing microscopy images of the planar-periodic – planar boundary condition cell taken at 0, 2, 3 and 10 V.

begin to switch before the twisted regions do, thereby increasing the index modulation initially. Below a voltage of ∼2 V the effective index of the planar regions decreases while the twisted regions remain the same. When the twisted regions also begin to align, the index modulation between the planar and twisted regions starts to decrease, thereby reducing the diffraction intensity. The on-time of this grating was measured to be 5 ms (±0.5 ms) with a relaxation time of 20 ms (±1 ms). The pitch-to-cell gap ratio was not optimized in this cell; a low diffraction efficiency of ∼3.5% was measured. To achieve a complete diffraction efficiency the pitch-to-cell gap ratio could be optimized using the thin screen approximation [23, 24].

3.3.4 Dynamic Switching of Hybrid Cells with Planar-Periodic – Homeotropic Boundary Conditions

The first order diffraction versus voltage curve for the planar-periodic – homeotropic (periodic-bend) configuration is presented in Figure 3.8. The thresholdless behavior of this film is a result of

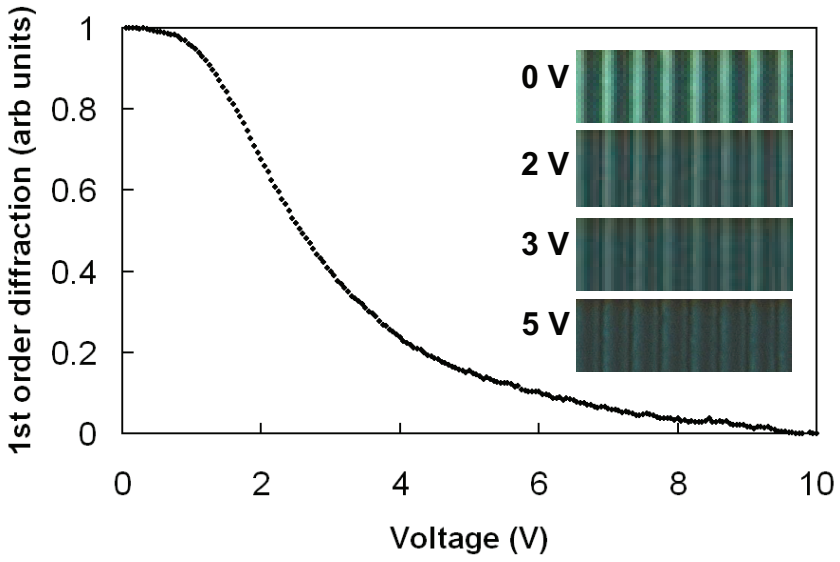

Figure 3.8: A plot of first order diffraction efficiency vs. voltage for a grating formed from planar periodic and homeotropic boundary conditions; this configuration exhibited a thresholdless voltage ($\Lambda = 7.5$ μm, $d = 5$ μm). The inset shows optical polarizing microscopy images of the planar-periodic – homeotropic boundary condition cell taken at 0, 2, 3 and 5 V.

the out of plane liquid crystal alignment established by the homeotropic substrate. As an electric field is applied across the sample, the liquid crystal is further aligned in the direction of the field, decreasing the index modulation. Optical polarizing microscopy images of the planar-periodic – homeotropic sample, shown in the inset of Figure 3.8, verify the alignment of the liquid crystal in the presence of an applied field. The on-time was measured at 3 ms ($\pm$0.5 ms) with a relaxation time of 15 ms ($\pm$1 ms). The diffraction efficiency was $\sim$1% and was attributed to the lower refractive index modulation across the grating for this particular configuration, as discussed in Section 3.3.1. The pitch-to-cell gap ratio was not optimized for this cell configuration.

3.4 Liquid Crystal Polymer Gratings

Following the development of these active liquid crystal polarization gratings, it is a natural progression to also make passive grating structures using reactive mesogen materials which can be aligned by the planar-periodic boundary conditions. The planar-periodic order through the depth of the film

is then captured by photopolymerization. A schematic representation of the fabrication steps used to create a passive polarization grating is shown in Figure 3.9(a). The planar periodic alignment layer was fabricated as described earlier, using LPP and polarization holography. A film of liquid crystal polymer (LCP CB 853) was coated onto the substrate with a Meyer bar, and subsequently polymerized in a nitrogen rich environment with UV light. An optical polarizing microscopy image of the liquid crystal polymer (LCP) grating between crossed polarizers is shown in Figure 3.9(b). The grating structure of this image indicates the polarization patterned alignment of the LPP induces the same patterned arrangement in the polymerized LCP layer as it does for low molecular weight liquid crystals. The dark regions of the grating correspond to areas where the LCP is aligned parallel or perpendicular to the polarizer or analyzer; the lighter regions correspond to region of LCP alignment at some angle with respect to the polarizer or analyzer. Since this LCP layer is completely polymerized on a single substrate, it can not be electrically switched; it can only act as a passive diffractive optical element for certain applications where switching is not required (i.e., simple spectrophotometer applications [29].

A close inspection of the microscopy photograph in Figure 3.9(b) reveals a significant number of defects. These defects are attributed to the top air surface, which does not enforce planar anchoring conditions. One can, of course, use reactive mesogen materials and two aligning surfaces to achieve a near perfect alignment similar to that observed in low molecular weight systems. Instead, the use of the liquid crystal polymer material obtained from ROLIC was chosen as it was developed to work well with the ROLIC LPP alignment layer. Other reactive mesogens should also work [30].

3.5 Free Energy Model

Polarization gratings were created with different pitch lengths ($\Lambda =$ 5, 7.5, 10, 12.5 and 15 μm) with uniform 5 μm cell gaps to investigate and model the threshold voltage behavior associated with the pitch of the polarization pattern. Since the grating pitch is comparable to or larger than the

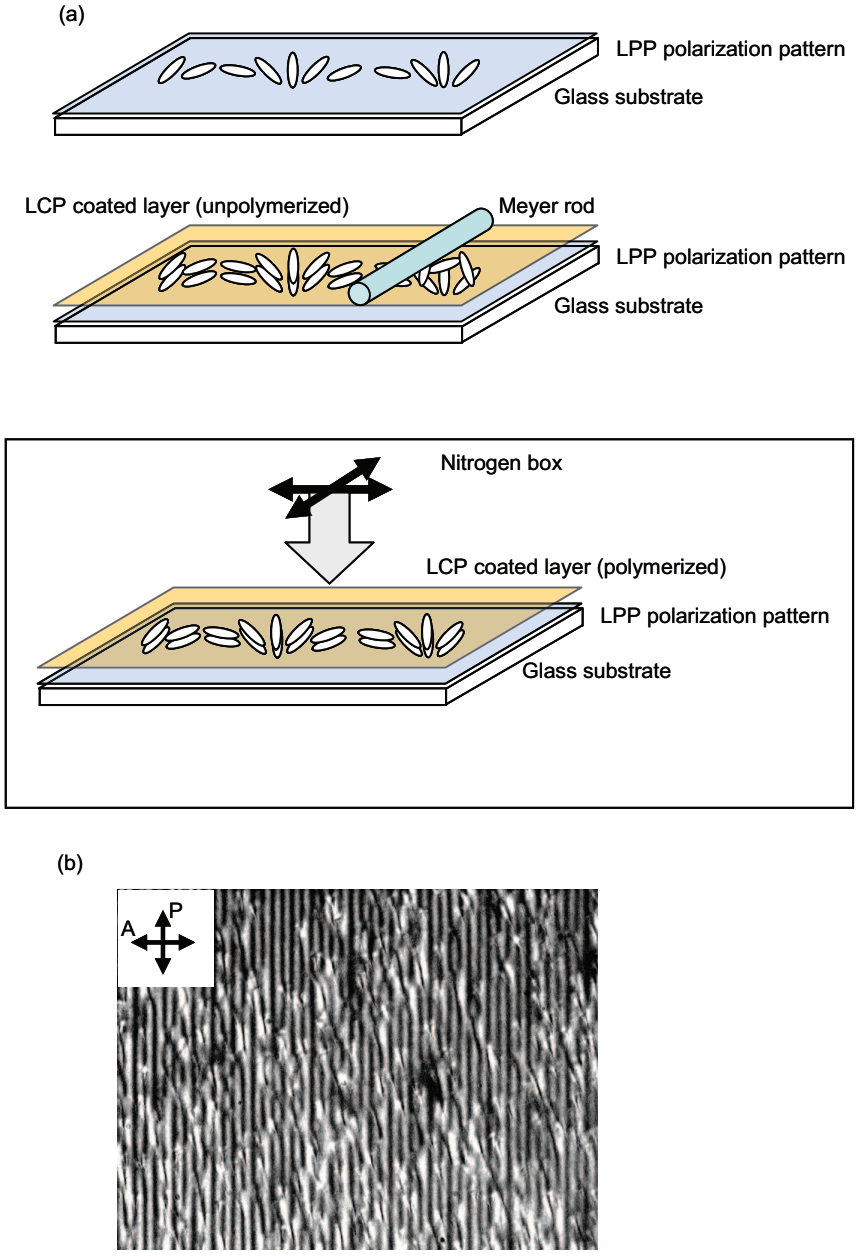

Figure 3.9: Optical polarizing microscopy image of a liquid crystal polymer (LCP) layer polymerized on a LPP polarization patterned substrate.

cell gap, the periodic boundary conditions imposed on the surface alignment layer are assumed to completely propagate through the depth of the cell, thus minimizing the free energy. In order to derive an expression for the free energy of this configuration a strong anchoring condition is imposed at the alignment layers with a zero tilt angle and a single elastic constant approximation is used. The free energy becomes [20]:

$$\frac{F}{\Lambda} = K \int_{-\Lambda/2}^{\Lambda/2} dy \int_0^d dz \left(\sin^2\theta_z \left(\frac{d\phi}{dy}\right)^2 + \left(\frac{d\theta}{dz}\right)^2 + 2\sin^2\theta_z \sin\phi_y \frac{d\phi}{dy}\frac{d\theta}{dz} - \frac{\Delta\varepsilon\varepsilon_0}{K}\left[E\cos\theta_z\right]^2 \right), \tag{3.2}$$

where F is the free energy; Λ is the grating pitch; K is the one elastic constant approximation; d is the cell gap; θ is the angle between the director $\mathbf{n}$ and the z-axis; ϕ is the angle between the director $\mathbf{n}$ and the x-axis; $\Delta\varepsilon$ is the dielectric anisotropy of the liquid crystal ($\Delta\varepsilon = +6.9$ for MLC-6292-100); ε_0 is the permittivity of free space; and E is the external electric field. Since the director varies spatially across the sample, the director profile through the depth of the sample is:

$$n = (\sin\pi y/\Lambda, \cos\pi y/\Lambda, 0). \tag{3.3}$$

By minimizing the free energy equation and taking into account the boundary conditions imposed at the photoalignment surfaces, the threshold voltage becomes:

$$V_{th} = \pi\sqrt{\frac{K}{\Delta\epsilon\epsilon_0}\left(1 - \frac{d^2}{\Lambda^2}\right)}, \tag{3.4}$$

where the threshold voltage is a function of the grating pitch and cell gap. In cases where the grating pitch is equal to the cell gap, the model predicts a thresholdless voltage. The model and experimental results for the threshold voltage as a function of grating pitch, $d - 5$ μm, are shown in Figure 3.10. The inset shows the visible diffraction patterns for $\Lambda = 5$, 7.5, 10, 12.5, and 15 μm. The boundary conditions imposed at the surfaces create non-uniform director orientations through the

depth of the cell in the zero electric field state. By applying an electric field across the sample (above the threshold voltage) the director is uniformly aligned in the direction of the field with no increase in the elastic field energy. This creates a gain in elastic energy due to electric and non-electric terms. Note, this does not happen in the ordinary Freedericksz transition, where at zero electric field the sample is uniformly aligned.

The periodic surface alignment created through the holographic exposure acts as an effective field of magnitude:

$$\left(\frac{d\phi}{dy}\right)^2 \propto \frac{1}{\Lambda^2}. \tag{3.5}$$

For a grating pitch comparable to the cell gap, it is energetically favorable to have a Freedericksz transition to a uniformly aligned state at zero electric field, in order to minimize the cost in elastic energy. In cases where the grating pitch is less than the cell gap, the model breaks down. This is due to the prohibitively high cost in elastic energy for the periodic director orientation to propagate through the depth of the cell. In this case, the director orientation in the interior part of the cell will not correspond to the director orientation at the surfaces.

3.6 Free Energy Considerations for Hybrid Boundary Conditions

3.6.1 Planar-Periodic – Planar Boundary Conditions

As described earlier, the planar-periodic – planar alignment configuration exhibits a lower threshold voltage behavior than the one predicted and observed in the registered periodic boundary alignment configuration. In this hybrid configuration, the periodic regions of planar and variable twist add to the elastic free energy in the zero electric field state, a facet not present in the periodic boundary alignment condition. As the applied electric field uniformly aligns the director, a decrease in

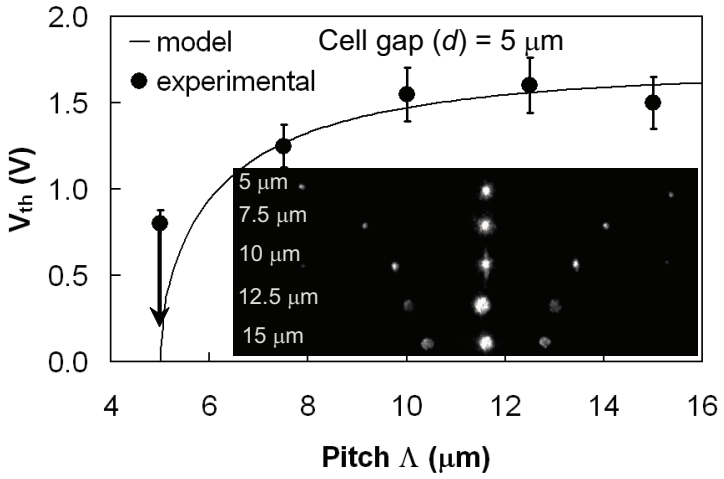

Figure 3.10: A plot of the threshold voltage as a function of grating pitch, Λ, for registered planar-periodic boundary conditions showing the experimental data points and phenomenological model for $d = 5$ μm. The inset shows the visible diffraction pattern for grating pitches $\Lambda = 5$, 7.5, 10, 12.5, 15 μm.

the elastic energy due to electric and non-electric terms results. We believe the additional twist component of this configuration affects the lower threshold voltage behavior. While this cannot be shown analytically, due to the more general functional dependences, this topic should be further investigated using computational methods.

3.6.2 Planar-Periodic – Homeotropic Boundary Conditions

The periodic-bend configuration, which also exhibits a thresholdless voltage behavior in the case when the grating pitch is larger than the cell gap, is described simply by virtue of the boundary conditions imposed at $z = 0$ and $z = d$, where the director field must bend out of the x-y plane between the substrates. As a result, applying a field perpendicular to the substrates, while inducing further bending out of the x-y plane, does not qualitatively change the zero-field arrangement (which is independent of the grating pitch and thickness). The thresholdless voltage response is expected and observed, as even strong fields only change the degree of bend rather than the type of director configuration.

3.7 Summary

A number of switchable liquid crystal gratings based on planar-periodic boundary conditions achieved through holographically (polarization holography) patterned alignment layers have been disclosed. The underlying physics was studied for various periodic structures. These structures are attractive for applications as they offer significantly reduced switching voltages as compared to other material combinations involving the patterned phase separation of liquid crystal / polymer dispersions. Furthermore, thin polarization gratings have the potential for nearly 100% diffraction efficiencies for circular polarization, as has been demonstrated by Escuti and co-workers [29, 31]. The extension of these simple gratings was also extended to the formation of passive polymerized structures.

Chapter 4

Other Photoalignment Gratings Configurations

This chapter expands on the one-dimensional nematic polarization grating structures discussed in Chapter 3 and presents on results on a variety of grating configurations. These novel grating configurations include: one-dimensional gratings using a calamitic thermotropic LC material exhibiting both stable smectic-A (SmA) and nematic phases, two-dimensional nematic gratings formed from separately exposed substrates, and two-dimensional nematic gratings formed from a single, four-beam holographic exposure.

4.1 One-Dimensional Grating Configurations Using Smectics

Jánossy and co-workers have demonstrated non-contact photoalignment techniques to optically control the alignment of a liquid crystal material having a nematic and smectic-A (SmA) phase [32–34]. By creating a sandwich-type cell configuration consisting of a polyimide coated substrate mechanically rubbed to promote planar alignment and a photosensitive azo-dye coated substrate, they induced an in-plane twist in the smectic-A phase by illuminating the photo-sensitive substrate with

polarized ultraviolet light. Furthermore, they have shown periodic alignment in the nematic phase, while illuminating the cell with a polarization interference pattern.

In this section, a non-contact photoalignment technique by means of a polarization holography exposure on a linear photopolymerizable polymer (LPP) alignment layer was used to create a periodic alignment configuration in a SmA liquid crystal material. This method, unlike Jánossy's, permanently writes a polarization pattern into the polymerized surface, which in turn is replicated through the depth of the cell when infiltrated with the SmA phase material.

To reiterate, the photo-chemical mechanism of the LPP material uses polarized ultraviolet light to create a (2+2) cyclo-addition of the coumarin photo-prepolymer molecules, forming long polymer chains parallel to the direction of the incident linear polarization, as reported by Schadt and coworkers. When the liquid crystal material comes into contact with the LPP coated substrate after the holographic exposure, it is planarly aligned with the average liquid crystal director parallel to the direction of the polymer chains. This creates a stratified periodic alignment configuration of liquid crystal due to the interaction with the LPP surface.

In this section, a SmA phase liquid crystal material was used in conjunction with a LPP coated substrate exposed to an orthogonal circular polarization interference pattern. As previously mentioned in Chapter 3, this polarization interference creates a spatially rotating linear polarization pattern that will polymerize the LPP in a periodic direction, promoting a spatially rotating planar alignment. This enables a periodic and structured alignment configuration of liquid crystal materials using only surface treatments.

4.1.1 Materials and Methods

Linear photopolymerizable polymer (ROLIC LPP F301 CP) commercially available from ROLIC Technologies (Allschwil, Switzerland) was spin coated on glass substrates to obtain a uniform film thickness of $\sim$100 nm. The substrates were then heated on a hotplate at 150 °C for 15 minutes to remove the excess solvent from the LPP. Empty cells were fabricated prior to the holographic

exposure by sandwiching two LPP coated substrates together separated by 5 μm glass fiber spacers. This fabrication step prior to the holographic exposure ensured the boundary conditions on the top and bottom substrates would be completely registered once the cell was infiltrated with liquid crystal. The empty cell was then illuminated with a two beam transmission interference pattern from an Ar^+ laser (Innova 70, Coherent, Santa Clara, CA) with an emission line of $\lambda = 351$ nm. The two interfering beams possessed equal intensities and orthogonal circular polarizations to form a spatially rotating linear polarization interference pattern with a pitch of $\Lambda = 7.5$ μm. Following the holographic exposure, 4'-n-4-octylcyanobiphenyl (8CB) was capillary filled into the empty cell at an elevated temperature and cooled to room temperature under ambient conditions. The 8CB exhibited the following phase transition temperatures in the bulk: crystal (21.5 °C) SmA (33.5 °C) nematic (40 °C) isotropic.

4.1.2 Optical Polarizing Microscopy Measurements

LPP polarization patterned gratings were fabricated with a holographic grating pitch, Λ, larger than the cell thickness, d. This ensured the liquid crystal alignment established by the surface patterning would be energetically favorable for propagation through the entire volume of the grating [20]. The grating appearance was probed at various temperatures using a computer controlled heat stage (INSTEC, Broomfield, CO) and an optical polarizing microscope. The images were captured between crossed polarizers from room temperature through the nematic and isotropic phases of the material, Upon reaching the target temperature, the temperature was held constant for 10 minutes prior to imaging, ensuring the liquid crystal grating structure had completely stabilized. Images were recorded at 32.5, 33, 33.5, 38, 40, and 42 °C, as shown in Figures 4.1(a-f), respectively.

The grating appearance in the SmA phase at 32.5 °C shows a well-defined grating with alternating dark and light textures. The dark appearance is attributed to planar liquid crystal alignment that is either parallel or perpendicular to the polarizer (P) or analyzer (A). The light appearance corresponds to a planar alignment at some azimuthal angle, θ, with respect to the polarizer or analyzer.

While the SmA material naturally opposes twist and bend deformations by having prohibitively large K_{22} and K_{33} elastic constants respectively, bend deformations were present, as observed by the light colored regions in the optical polarizing microscopy image. The optical contrast between the alternating dark and light colored regions verifies the holographic exposure on the alignment layer creates a periodic alignment of liquid crystal in the SmA phase.

As the polarization grating was heated to 33 °C, slightly below the SmA-nematic transition temperature, a transformation in the grating texture was observed. While still possessing partial regions of highly ordered LC alignment (parallel or perpendicular to the polarizer or analyzer), less ordered alignment regions were also apparent as indicated by the light color regions shown in Figure 4.1(b). Once heated to 33.5 °C (the SmA-nematic transition temperature for bulk 8CB), the grating texture changed. Instead of the well-defined alternating light and dark regions of the SmA phase, the nematic phase established a 'rougher' grating texture with less well-defined boundaries. This texture was characteristic of a more randomly ordered alignment, as further observed in the images captured deep in the nematic phase (38 °C) and at the nematic-isotropic transition temperature (40 °C).

Once the sample was heated above the nematic-isotropic transition temperature, a faint optical grating structure remained. This texture suggests the presence of a residual alignment caused by the polarization pattern at the surface, even though the sample was stable in the isotropic phase. While this was fascinating from a surface ordering phenomenon, the underlying mechanisms are considered out of the scope of this thesis and can be investigated in future work.

4.1.3 Qualitative Temperature Dependence of Optical Diffraction

In order to fully evaluate and understand the alignment changes occurring during the various phase sequences of the material, a helium-neon laser probed the grating while a digital camera captured still images of the projected visible diffraction pattern. These images were taken at 28, 32, 34, 40, 42, and 44 °C, as shown in Figures 4.2(a-f), respectively. As the grating was heated from room temperature to 32 °C (remaining in the SmA phase), the visible diffraction showed the presence

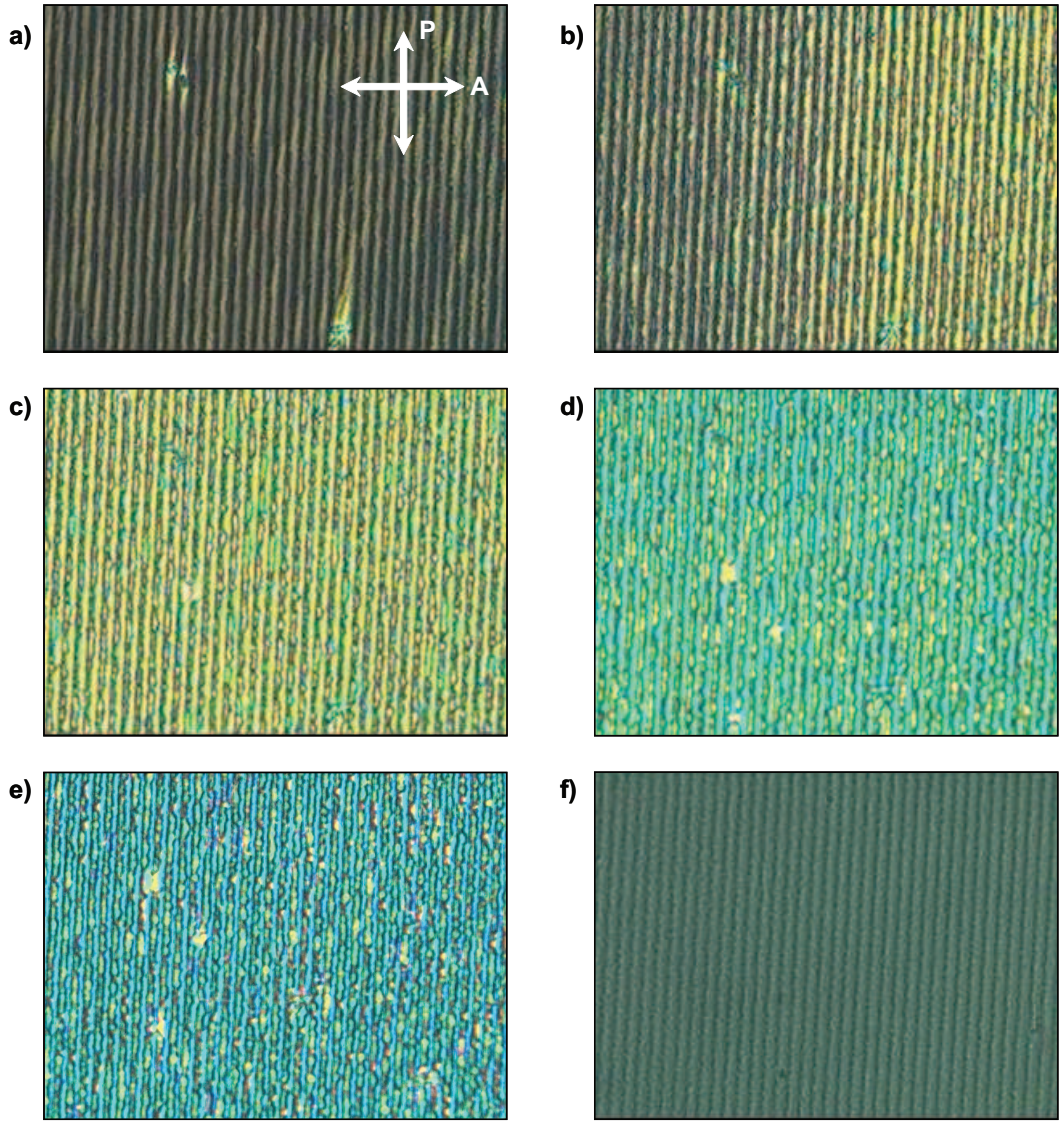

Figure 4.1: Optical polarizing microscopy images of a liquid crystal grating formed from a holographically patterned photo-alignment layer. Images were captured at (a) 32.5 °C, (b) 33 °C, (c) 33.5 °C, (d) 38 °C), (e) 40 °C, and (f) 42 °C.

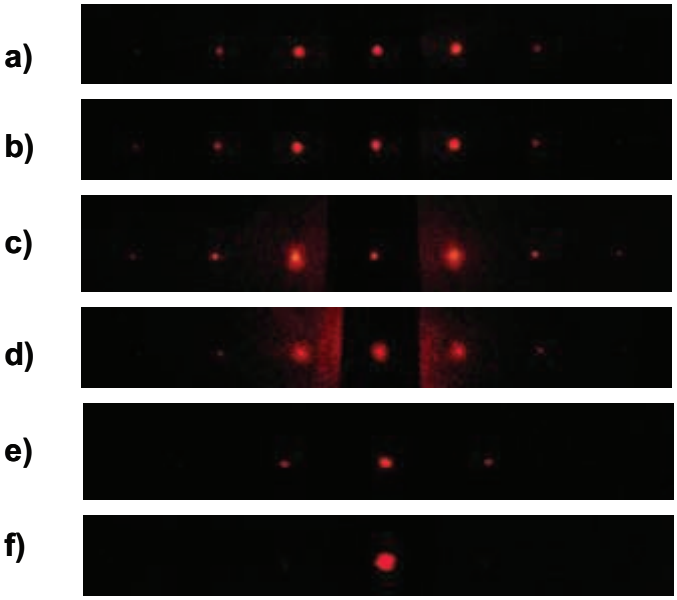

Figure 4.2: Images of an optical diffraction pattern taken at (a) 28 °C, (b) 32 °C, (c) 34 °C, (d) 40 °C, (e) 42 °C, and (f) 44 °C.

of strong ±1, ±2, and ±3, diffracted orders, with minimal scattering. This further supports the smooth, well-defined SmA grating structures observed with the optical polarizing microscope. Upon further heating, above the SmA-nematic transition temperature, strong scattering was observed, along with an increased intensity in the ±1 diffracted orders.

At the nematic – isotropic transition temperature, an optical diffraction pattern was still present. While the ±1 diffracted orders could still be observed, the ±2, and ±3 orders were no longer apparent, further supporting the optical polarizing microscopy findings in Figure 4.1(e). At this transition temperature, nematic ordering was still present, albeit much less defined than at temperatures deeper in the nematic phase. The diffraction image at 42 °C shows the weak presence of ±1 diffracted orders. Although it is believed that the midlayer of the polarization grating is isotropic, the patterned surfaces induce a residual ordered alignment, supporting the microscopy image of the grating in Figure 4.1(f). Upon further heating, deeper in the isotropic phase, the residual alignment observed earlier is erased. At 42 °C, only the zeroth order was present, confirming the entire grating was isotropic.

4.1.4 Temperature Dependence of Diffraction Intensity

In order to measure the change in diffraction for the SmA and nematic phases, a helium neon laser was used to probe the polarization grating while a photodiode connected to a wide band amplifier and computer monitored the first order diffracted intensity as a function of temperature. The measured intensities were recorded as the sample was heated from $26 - 46$ °C, as shown in Figure 4.3.

The presence of higher order diffraction peaks and the relatively low first order diffraction intensity observed in the SmA phase confirms and supports the optical polarizing microscopy and diffraction images. This phase, although highly ordered, exhibits a relatively low index modulation through the depth of the grating. This was attributed to the ordered smectic layers resisting the bend configuration imposed by the patterned surfaces.

It was not until the grating reached the SmA-nematic transition temperature that the first order diffraction peaks increased in both intensity and scattering. This resulted from a larger index modulation occurring through the depth of the grating as the less ordered nematic phase did not oppose the bend configuration of the surface patterning. The increased scattering was also attributed to the 'rough' grating texture as observed in the optical polarizing microscopy study. When heated deeper into the nematic phase, the first order diffracted intensity decreased continuously until the nematic-isotropic transition temperature was reached. This transition is associated with the weaker Van der Waals interactions between the LC and the surface inducing a weaker surface alignment. At 42 °C, just above the nematic-isotropic transition, a weak first order diffraction was recorded. Although weaker than the SmA and nematic phase first order diffracted intensities, a noticeable diffraction peak confirmed the presence of a residual ordering occurring at the LPP polarization patterned surfaces. Above 42 °C, only the zero order transmitted beam was present, confirming the liquid crystal film was completely isotropic.

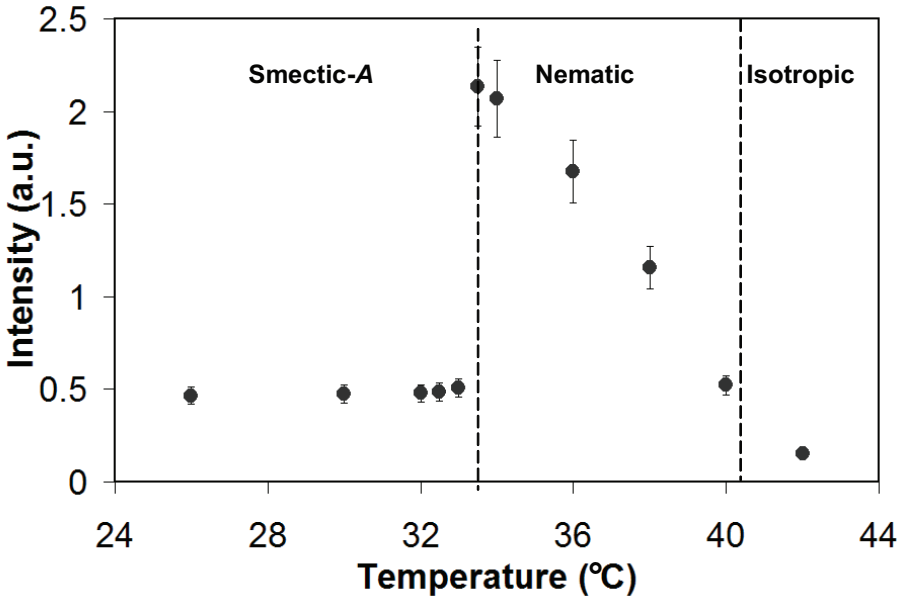

Figure 4.3: Measured first order diffraction intensity as a function of temperature.

4.1.5 Electro-optic Performance

The threshold switching voltage characteristics of these polarization gratings was also investigated as a function of temperature. A 1 kHz square wave was applied across the film while the first order diffracted intensity was recorded as the voltage was increased to 1.4 V. The corresponding intensity vs. voltage curves were taken at 32, 33, 36, 38, and 42 °C, as shown in Figure 4.4. As the voltage ranged from $0 - 1.4$ V, in the smectic phase at 32 °C, the grating did not experience a critical field strong enough to induce the LC to orient parallel to the electric field. Since the SmA phase resists bending deformations in both the polar and azimuthal angles, it characteristically requires higher critical fields as compared to nematics.

As the temperature was increased to the nematic phase, the polarization grating exhibited electro-optic switching characteristics. Deep in the nematic phase the threshold voltage was recorded to be ∼1.1 V, comparable to the threshold voltages for the one-dimensional nematic polarization gratings as discussed in Chapter 3. Further increasing the temperature in the nematic phase resulted in reduced threshold voltages. This reduction was again attributed to the weaker Van del Waals

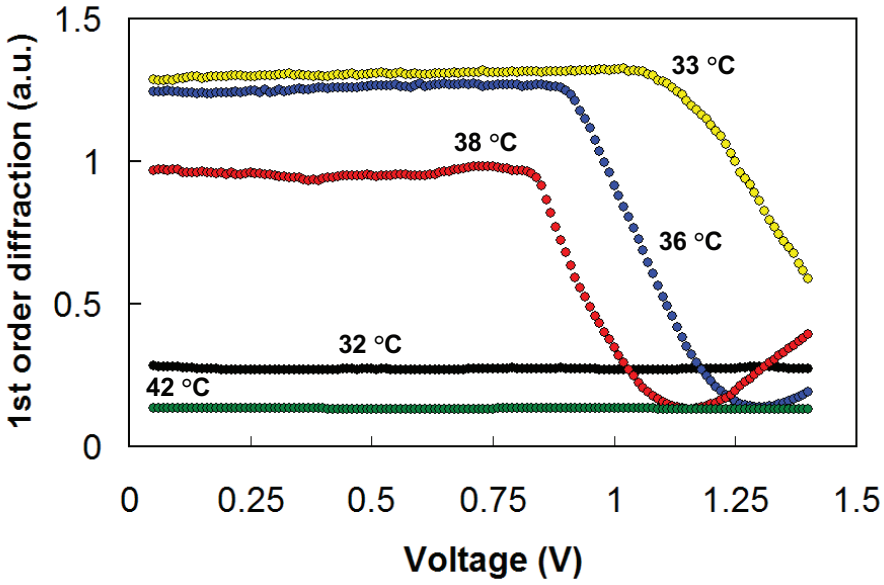

Figure 4.4: Electro-optic switching behavior of the first order diffraction as a function of voltage and temperature.

interactions at the surface allowing the LC to align in the direction of the applied field at lower voltages.

At 42 °C, the residual patterned LC alignment at the surface, which created a weak first order diffraction peak, did not noticeably respond as the voltage was increased to 1.4 V.

4.1.6 Smectic-A and Nematic Director Profiles

Based on the temperature dependence of the microscopy and diffraction results, conclusions have been made about the director profile on the LPP patterned surfaces and also in the mid-layer. These conclusions reflect the differences in the grating texture observed with optical polarizing microscopy, as well as the relative strength and presence of scattering in the visible diffraction patterns for SmA and nematic ordering.

The ideal director profiles for SmA and nematic polarization gratings and their corresponding index modulation profiles are illustrated in Figure 4.5. In the nematic phase, the continuously

rotating bend configuration imposed by the surface patterning caused the average nematic director alignment to continuously bend on the surfaces. This periodic alignment also propagates through the mid-layer, as shown in Figure 4.5(a). Manifested in this director profile is a sinusoidal index modulation that propagates from the surface alignment through the mid-layer of the film. Of course, this is an idealized representation of what is occurring deep in the nematic phase; as the temperature increases in the nematic phase, approaching the isotropic temperature, the Van der Waal interactions between the surface and LC decrease, resulting in a more random alignment.

In contrast, the schematic representation of the SmA phase in Figure 4.5(b) shows a continuous bend alignment only at the surface. The anchoring energy on the surface inhibits the formation of smectic layers. As the liquid crystal alignment propagates further into the mid layer it is more energetically favorable to form smectic layers (planar alignment) rather than having the continuous bend alignment established by the surface patterning. As a result, the refractive index modulation profile at the surface is different than that occurring in the mid-layer. Assuming strong Van der Waals forces at the surface, the director profile assumes the sinusoidal index modulation as shown in the nematic phase. However, at the mid-layer, the SmA refractive index modulation is represented by a constant refractive index resulting from the planar alignment. This, of course, is an idealized representation.

4.1.7 Thermally Bi-stabile Configurations

A unique embodiment of a polarization patterned grating using a liquid crystal material with a SmA and nematic phase is the ability to create thermally bistable configurations, the practical applications of which will be described in Chapter 6.

In order to create a thermally bistable configuration, the polarization pattern needs to be heated from the SmA phase to the nematic phase. Upon reaching the nematic phase, a voltage is applied across the grating to homeotropically align the molecules perpendicular to the substrates, as illustrated in Figure 4.6(a). The temperature is then slowly decreased from the nematic to the SmA

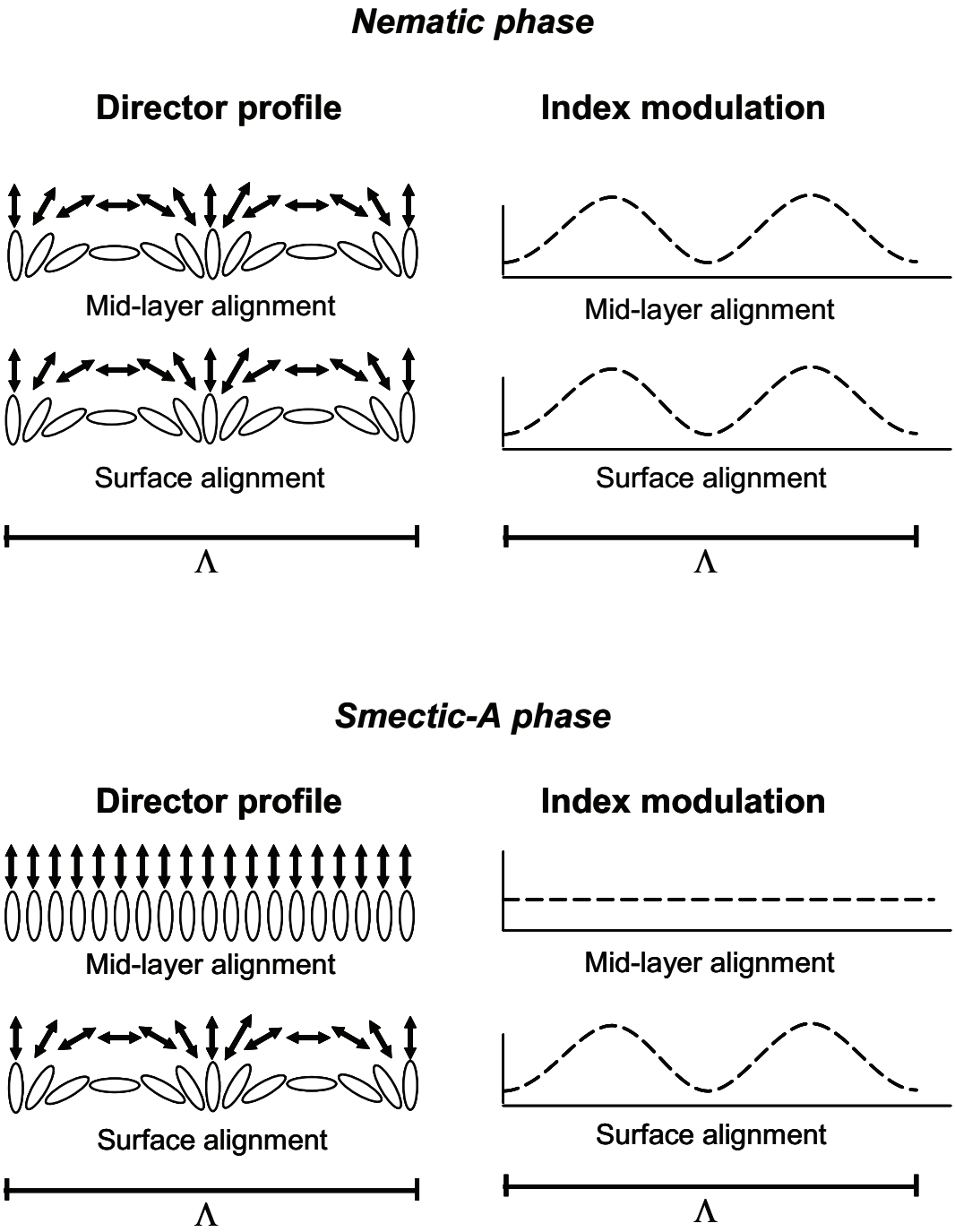

Figure 4.5: The director profile corresponding to surface and mid-layer alignment for (a) nematic and (b) smectic liquid crystal polarization gratings.

phase, while the voltage continues to be applied across the grating. This ensures the molecules remain homeotropically aligned and form the ordered lamellar arrangement characteristic of a bulk SmA liquid crystal. Once deep in the SmA phase the voltage can be turned off, leaving the homeotropically aligned liquid crystal unperturbed, as illustrated in Figure 4.6(b).

With this thermally stabilized alignment state, incident laser light on this sample will not experience a refractive index modulation and therefore not diffract as previously observed in the SmA phase at $V = 0$. If, however, the thermally stabilized alignment experiences a temperature increase, exceeding the SmA-nematic transition, in the absence of an external voltage, the LC molecules will realign to the original nematic configuration imposed by the surface alignment conditions, as shown in Figure 4.6(c). Likewise, if the grating is further cooled to the SmA phase, the periodic alignment will remain 'locked in,' assuming the periodic boundary conditions imposed by the surface alignment as in Figure 4.6(d). If incident laser light illuminates the configuration in Figure 4.6(c-d) it will experience the periodic index modulation and create a visible diffraction pattern similar to that in Figure 4.2.

4.1.8 Smectic Grating Summary

The ability to create patterned liquid crystal alignment in the SmA and nematic phases by using a holographically patterned photoalignment layer has been demonstrated. The optical polarizing microscopy and diffraction characteristics were evaluated as a function of temperature. The periodic alignment established by the photoalignment layer created strong diffraction gratings stable in both the nematic and smectic-A phases. The relative intensities and presence or absence of scattering in the diffraction gratings was also discussed in the context of surface and mid-layer director profiles. Switching characteristics were also investigated and are typical of LC-based polarization patterned gratings. Finally, a thermally bi-stable grating configuration was disclosed with applications to be discussed in Chapter 6.

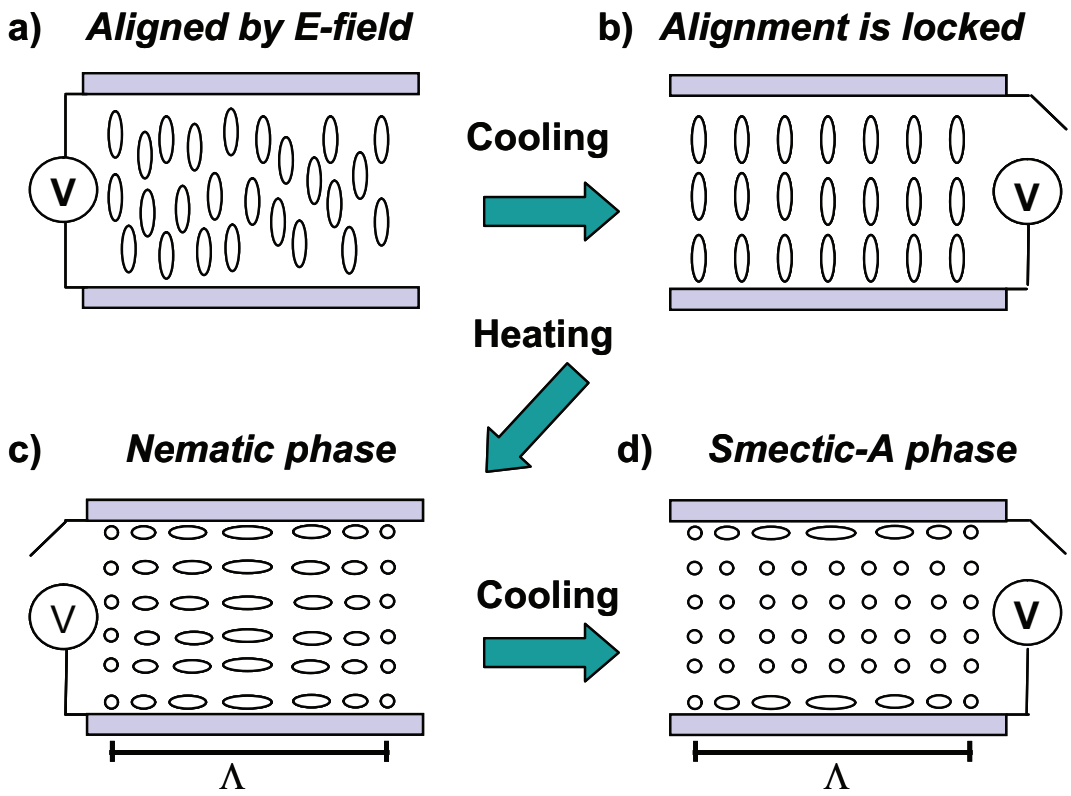

Figure 4.6: A schematic illustration of a thermally bistable grating configuration using liquid crystal material with a SmA and nematic phase.

4.2 Two-Dimensional Grating Configurations from Separately Exposed Substrates

Though the work with 1-D nematic gratings and the opto-electrical intricacies that resulted, it is a natural progression to also investigate periodic alignment in two-dimensions. Two-dimensional active gratings were created by exposing LPP and ITO glass substrates to the orthogonal circular polarization interference pattern ($\Lambda = 15$ μm) individually, and assembling an empty cell configuration with one polarization patterned substrate rotated 90° with respect to the other. The resulting configuration is a two-dimensional array of planar and twisted ($\leq 90°$) liquid crystal alignment created by the overlapping patterned surfaces.

A schematic illustration showing the two-dimensional alignment array between parallel and crossed polarizers is presented in Figures 4.7(a) and 4.7(b). The dashed arrows represent the liquid crystal director alignment on the top substrate, while the solid arrows represent the liquid crystal director alignment on the bottom substrate. Regions with parallel arrows indicate planar alignment propagating through the depth of the cell. Regions with orthogonal arrows represent 90° twist configurations. Finally, regions with arrow directions angled between 0° and 90° represent twist configurations coinciding with the angle between the two arrows. When such a configuration is placed between parallel polarizers an optical microscopy image, as shown in Figure 4.7(c), is achieved with the light regions coinciding with planar alignments parallel or perpendicular to the polarizer or analyzer. Regions producing a twist $< 90°$ can be seen as gray areas in the illustration in Figure 4.7(a) and Figure 4.7(c). Likewise, 90° twist regions appear as dark regions between parallel polarizers. Once the polarizer and analyzer are crossed, a contrast inversion occurs in the images. The planar aligned regions that were light regions between parallel polarizers appear as dark regions; the 90° twist regions that were dark between parallel polarizers appear as light regions. This is shown in the optical polarizing microscopy image, in Figure 4.7(d). An example of the two-dimensional diffraction pattern generated by this grating is shown in Figure 4.7(e), using a helium-neon laser ($\lambda = 633$ nm).

The diffraction efficiency from one of the four first order diffraction peaks was measured to be ∼8%.

The electro-optic switching curve for one of these two-dimensional samples ($\Lambda = 15$ μm, $d = 5$ μm) is shown in Figure 4.8. The experimental results show the transmission versus voltage curve with a nearly thresholdless behavior. Above the voltage necessary to align the liquid crystal, the material becomes aligned at the boundaries, resulting in a gain in elastic energy from both the electric and non-electric terms in the interior of the cell. The on-times of these films were measured to be 5 ms (±0.1 ms) with relaxation times of 15 ms (±1 ms), comparable to those of the one-dimensional gratings.

In all cases (one-dimensional and two-dimensional gratings) the electro-optic response times were roughly equivalent to those of liquid crystal cells with uniform alignment. The feature sizes of our periodic alignment condition were on the order of ∼7 μm, which is relatively large. Larger deviations in switching times are expected for smaller feature sizes (i.e., < 1 μm), where elastic distortion effects can play a bigger role.

4.3 Two-Dimensional Gratings from a Single Holographic Exposure

The final grating configurations presented in this chapter use a single four-beam exposure to create two-dimensional periodic alignment configurations of liquid crystal. This exposure configuration inherently assures that the top and bottom substrates are registered with respect to each other.

A holographic exposure technique was employed by interfering multiple coherent laser beams to create a desirable irradiance profile incident on a linear photopolymerizable polymer alignment layer. The interference profile can be generalized as a vector sum of electric fields of the incident beams as defined by:

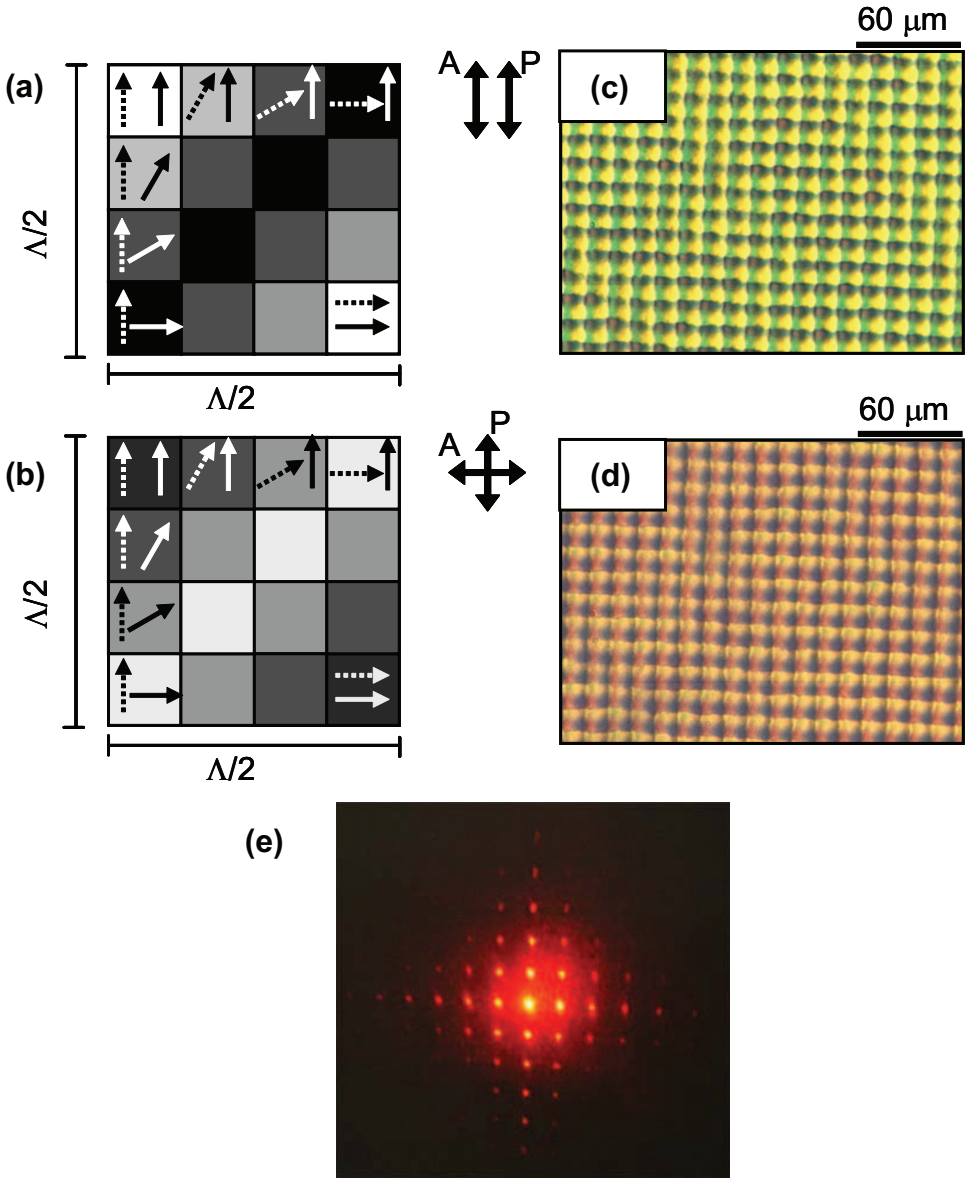

Figure 4.7: (a) A schematic representation of the liquid crystal director orientation in a two-dimensional grating between parallel polarizers, arrows indicate director orientation on the alignment surfaces; (b) a schematic representation of the liquid crystal director orientation in a two-dimensional grating between crossed polarizers; (c) optical polarizing microscopy image of a two-dimensional grating between parallel polarizers; (d) optical polarizing microscopy image of a two-dimensional grating between crossed polarizers; (e) visible diffraction pattern created from a two-dimensional polarization grating.

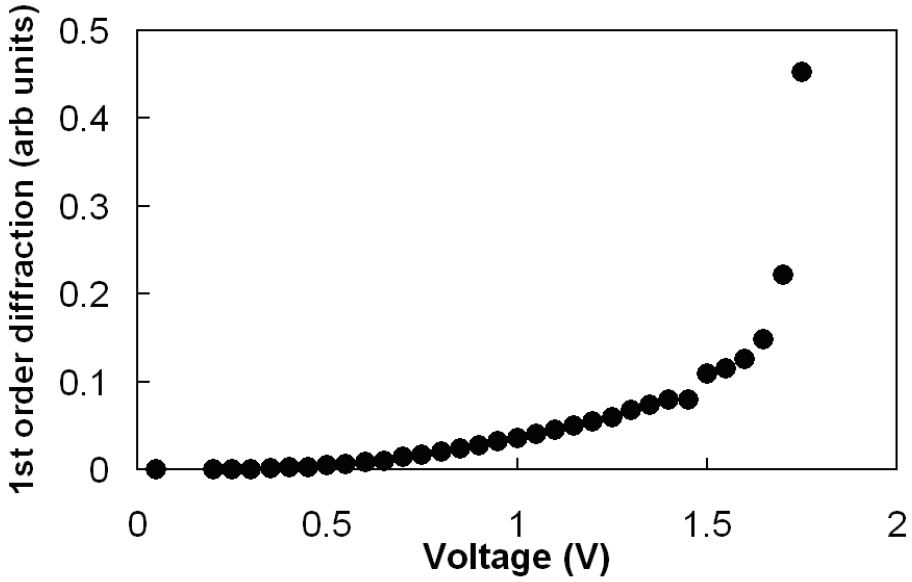

Figure 4.8: Plots of transmission vs. voltage for a two-dimensional planar-periodic cell configuration ($\Lambda = 15$ μm, $d = 5$ μm); the threshold voltage was 0.5 V.

$$I(r) \propto R\left\{\sum_{l=1}^{N}\sum_{m=1}^{N} E_l \cdot E_m^* e^{i(k_l - k_m)\cdot r}\right\}, \tag{4.1}$$

where I is the resulting intensity; r is the spatial position vector; N is the number of coherent beams incident on the film; and k is the wave number. The maximum resulting intensity occurs when $k_l - k_m$ is equal to a reciprocal lattice vector G_{lm}.

From this phenomenon an exposure technique was developed using both amplitude and polarization holography to selectively polymerize LPP alignment layers and create periodic and continuous alignment configurations for a liquid crystal material in two-dimensions. In traditional (amplitude) holography, a spatial modulation occurs without disturbing the polarization state. In polarization holography, the resulting polarization state is modulated, ideally with little modulation in the light intensity. While there are extensive publications on the electro-optic behavior on one-dimensional periodic and hybrid alignment configurations using polarization holography, this chapter demonstrates a 2-D registered patterned alignment using a four-beam polarization holographic exposure.

However, for these configurations a slight intensity modulation does exist, but this observation did not affect the alignment configurations established by the polarization modulation.

4.3.1 Periodic Circumferential Alignment

Four non-coplanar p-polarized beams having the same polar angle of 4° distributed evenly around the azimuthal plane were used to generate a 2-D irradiance profile of a circumferential polarization pattern, as shown in Figure 4.10(a). The high intensity regions of the interference pattern are represented by red, with low intensity regions represented by blue. The result is a square lattice with a periodicity of ∼1.7 μm. Super-imposed on the iso-intensity pattern is a 2-D map of the linear polarization field, represented by blue lines. During the holographic exposure, the LPP material selectively polymerized along the same direction of the incident polarization, mimicking the periodic circumferential pattern. Once the liquid crystal material was infiltrated into the holographically exposed cell, it exhibited a continuous and periodic planar alignment configuration with a grating pitch of ∼3 μm. An optical polarizing microscopy image of the 2-D circumferential liquid crystal alignment configuration is shown in Figure 4.10(b). The optical polarizing microscopy image, captured in the transmission mode between crossed polarizers, shows a 2-D periodic alignment of liquid crystal where the dark regions of the microscopy image represent uniform planar alignment either parallel or perpendicular to the polarizer (P) or analyzer (A). The lighter grey regions of the microscopy image represent liquid crystal alignment at some angle between the crossed polarizers.

Additionally, a simulation of the theoretical prediction of what the optical polarizing microscopy image should look like between crossed polarizers is shown in Figure 4.10(c), assuming no out-of-plane alignment. This was achieved by mapping the polarization vector field with planar aligned liquid crystal parallel to the direction of the polarization. By simulating the birefringence and alignment of the liquid crystal between crossed polarizers, the transmitted intensity was modeled as a function of the liquid crystal alignment direction. The dark regions in Figure 4.10(c) represent a uniform liquid crystal alignment parallel or perpendicular to the polarizer (P) or analyzer (A);

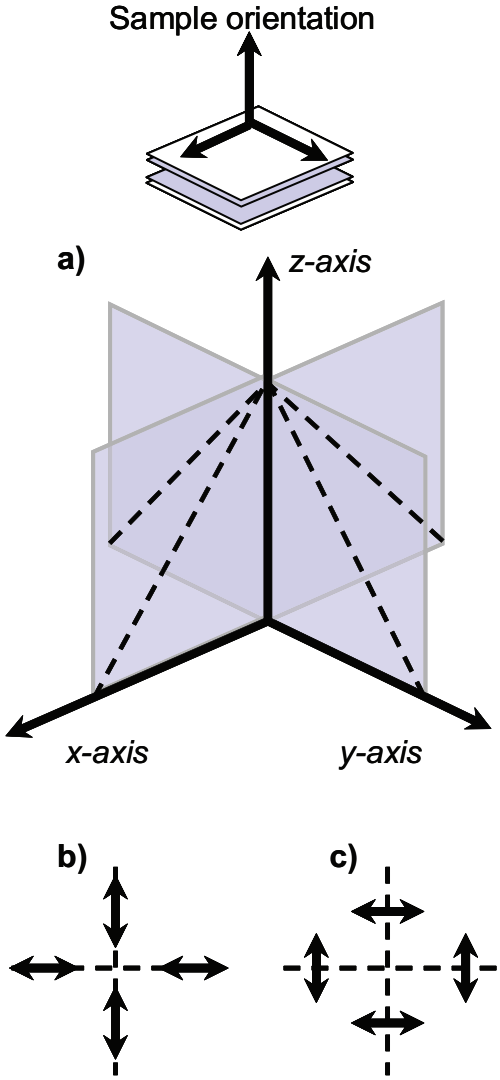

Figure 4.9: Schematic representation of a four beam holographic setup and exposure. (a) Top view illustration (along z-axis) of the beam polarizations for (b) periodic circumferential and (c) radial alignment configurations.

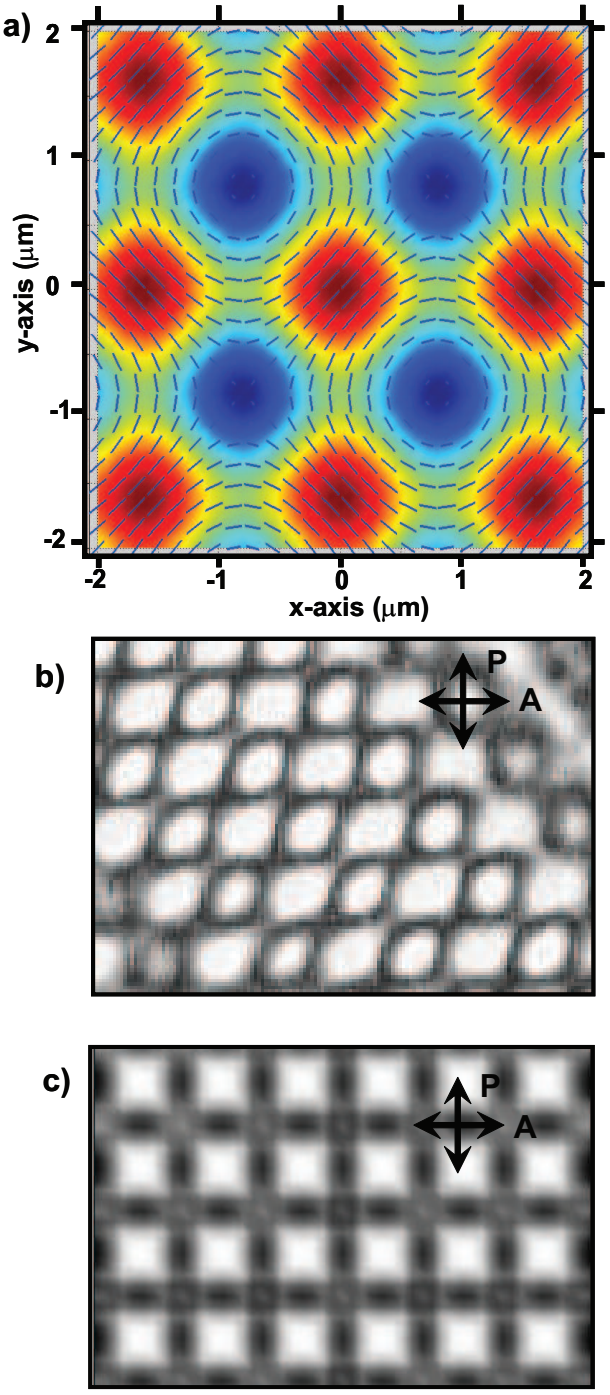

Figure 4.10: A two-dimensional patterned circumferential liquid crystal alignment surface profiles showing (a) a computational simulation of the two-dimensional scalar iso-intensity and vectorial polarization modulation, (b) an optical polarization microscopy image of the liquid crystal alignment pattern between crossed polarizers and (c) a computational simulation of the liquid crystal alignment imaged between crossed polarizers.

and the light regions represent liquid crystal at some angle θ between the crossed polarizers. These initial results show the expected similarities between the experimental and theoretical predictions of the alignment pattern.

4.3.2 Periodic Radial Alignment

To create a 2-D patterned radial polarization pattern, four non-coplanar s-polarized beams having the same polar angle of 4° distributed along the same azimuthal plane were used. The irradiance profile of a radial polarization pattern is shown in Figure 4.11(a) with an overlay showing the polarization modulation. The iso-intensity pattern of the radial alignment was similar to the circumferential pattern; however, the vectorial maps of the polarization fields were different. the optical polarizing microscopy image of the radial alignment between crossed polarizers is shown in Figure 4.11(b), as compared to the theoretical prediction in Figure 4.11(c).

4.3.3 Electro-optic Results

Initial electro-optic switching results revealed a low threshold voltage behavior (< 2 V) for both the circumferential and radial 2-D patterned configurations, as shown in Figures 4.12 and 4.13, respectively. In these plots, the first order diffraction intensity was measured as a function of applied voltage using a helium-neon laser ($\lambda = 633$ nm) to probe the patterned alignment region addressed with a 1 kHz square wave applied across the sample. A photodetector connected to a wide band amplifier and digital multimeter recorded the change in diffracted intensity.

The electro-optic behavior that occurred at low applied voltages may be attributed to the low pretilt angles in the alignment layer, giving rise to the presence of disclination lines. This phenomenon was also observed this in one-dimensional hybrid alignment configurations as previously discussed in Chapter 3.

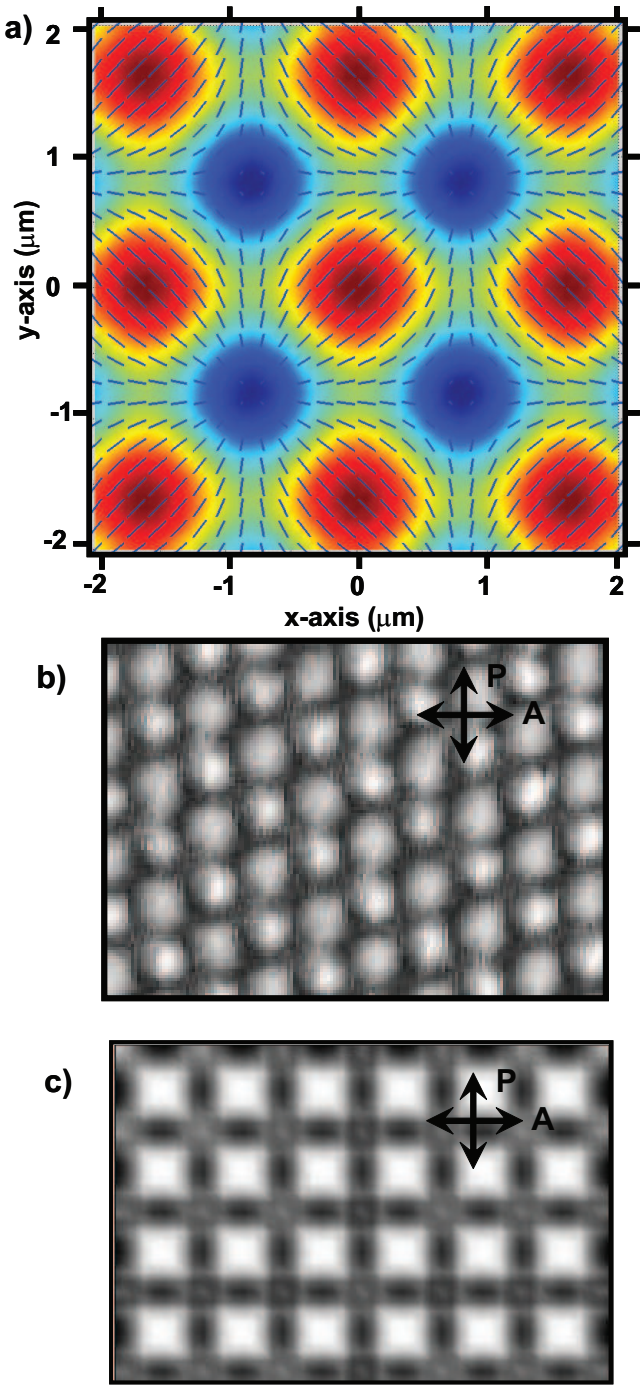

Figure 4.11: A two-dimensional patterned radial liquid crystal alignment surface showing a (a) computational simulation of the two-dimensional scalar iso-intensity and vectorial polarization modulation, (b) an optical polarization microscopy image of the liquid crystal alignment pattern between crossed polarizers and (c) a computational simulation of the liquid crystal alignment imaged between crossed polarizers.

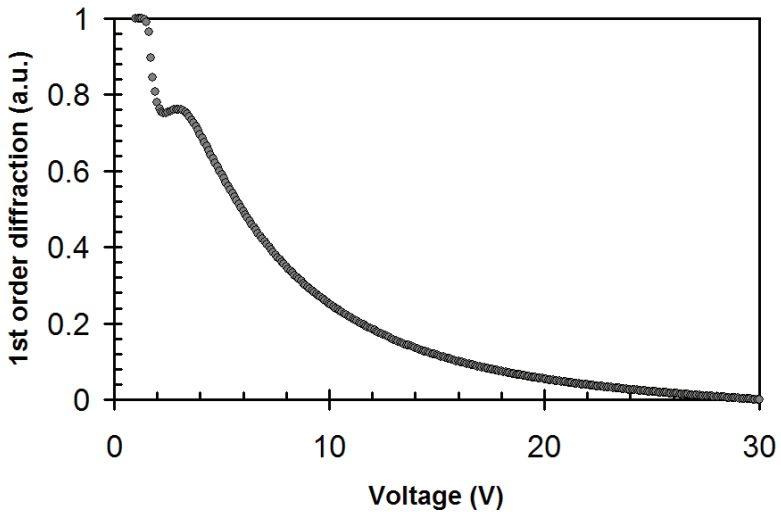

Figure 4.12: Electro-optic measurements of first order diffraction intensity as a function of applied voltage for a two-dimensional patterned liquid crystal alignment induced by circumferential polarization patterned surfaces.

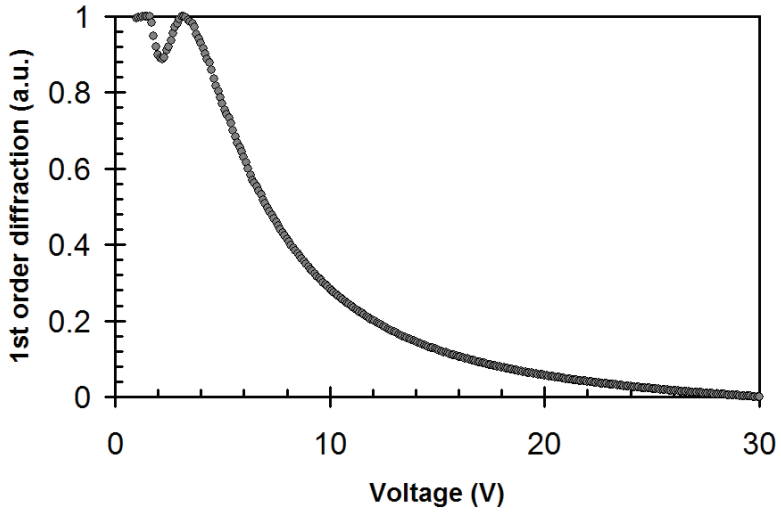

Figure 4.13: Electro-optic measurements of first order diffraction intensity as a function of applied voltage for a two-dimensional patterned liquid crystal alignment induced by radial polarization patterned surfaces.

4.4 Two-dimensional Grating Summary

Patterned alignment layers have been fruitful areas of research for the demonstration of novel liquid crystal configurations and geometries useful in display applications; in particular, for wide viewing angle solutions. This work with 2-D patterned alignment layers is extremely pertinent to the display community because of the ability to implement patterned alignment configurations as active optical elements for the expansion of viewing angles in displays.

This chapter outlined several two-dimensional patterned configurations – a 2-D alignment generated by using two individually exposed substrates, as well as a 2-D concentric alignment and a 2-D radial alignment formed in a single exposure step. This holographic exposure technique is not limited by these available materials or exposure configurations. Similar alignment patterns using reactive mesogens for retarder applications, pertinent to transflective displays, could also be fabricated using this single-step holographic exposure technique.

Chapter 5

Holographic Polymer Dispersed FLC Gratings

5.1 Introduction to H-PDFLCs

Switchable gratings comprised of periodic dispersions of liquid crystal encapsulated by a photopolymer network have been demonstrated as candidates for a number of applications including diffractive optical elements, optically pumped lasers [3,35–38], reflective displays [39–41], switchable lenses and mirrors [42], and telecommunications devices [43]. Fabrication of these composite structures is accomplished through a holographic exposure incident on a homogenous mixture of nematic liquid crystal, pre-polymer and photo-sensitive dyes; the resulting films are referred to as holographic polymer dispersed liquid crystals (H-PDLCs) [44–46]. A permanent recording of the holographic exposure, modulated in amplitude, polarization or a combination of both, in photosensitive materials results in a refractive index modulation and a grating structure.

When an amplitude modulation is present on such a dispersion, a photo-induced phase separation and counter diffusion process creates a periodic and well-segregated dispersion of the liquid crystal

and polymer materials [39, 47]. The pre-polymer polymerizes in the bright fringes of the interference pattern, counter-diffusing the liquid crystal to the dark fringes. Amplitude modulation recording in H-PDLCs has been demonstrated with various material sets, including both acrylate and thiol-ene polymers [48, 49], sensitive to holographic exposures at ultraviolet (UV) or visible wavelengths.

Cipparrone and coworkers have also successfully demonstrated H-PDLC gratings formed from polarization modulation rather than amplitude modulation [50]. For this type of exposure, the orientation of the liquid crystal is controlled by the incident polarization state, resulting in a uniform alignment encapsulated by a periodic polymer network. Both exposure techniques effectively capture the profile of the holographic pattern, creating a stratified structure of liquid crystal and polymer with a refractive index modulation. In turn, the modulation in refractive index produces Bragg reflective or diffractive properties, which can be electrically 'erased' to create a transparent film when the indices of the polymer and liquid crystal are matched.

Recent developments in this field have led to the replication of two- and three-dimensional lattices and quasi-lattices periodic on length scales commensurate with the wavelength of visible light. Face-centered cubic lattices have been demonstrated in an H-PDLC [51, 52], as well as an orthorhombic square lattice [53]. Quasi-crystal H-PDLCs with 5, 7, and 9-fold symmetry have also been shown [54, 55].

Liquid crystal alignment in H-PDLC confined geometries is significantly influenced by the morphology of the polymer network. The morphology, which can be classified as rough droplets, scaffolds or smooth layers, dictates the uniformity in the liquid crystal alignment and incoherent scattering in the grating [56–58]. In order to reduce the amount of scattering, researchers have disclosed a homogeneous liquid crystal alignment texture having well-defined polymer walls in an H-PDLC by exposing the liquid crystal and pre-polymer mixture above the nematic-isotropic transition temperature [59–61]. Various other investigations have sought to optimize the diffractive properties of these structures through further adjustments in the polymer material or other conditions during the fabrication process [56, 57, 62–64].

Ferroelectric liquid crystal materials represent an interesting class of materials, which have been utilized for liquid crystal displays and other diffractive optical devices. Ferroelectric materials are advantageous because of their intrinsic polarization, fast response times and bistability [65]. Polymer dispersed ferroelectric liquid crystals (PDFLCs) and surface stabilized ferroelectric liquid crystal (SSFLC) have been demonstrated for rapidly switchable light shutters and other photonic applications [66–68]. In these systems, a prepolymer mixture of reactive monomer and FLC is photopolymerized, phase separating the FLC into randomly aligned micrometer sized droplets encapsulated in a polymer binder. A uniform alignment of the FLC can be achieved by applying mechanical shear [65, 69], or an electric or magnetic field across the film [70].

In this contribution we elaborate on the diffractive properties, previously reported on in an earlier contribution [70], for creating smooth polymer walls for the uniform alignment of ferroelectric liquid crystals (FLC) in layers using a holographic exposure [71, 72]; as opposed to nematics, which have been the dominant liquid crystal phase used for holographic polymer dispersed systems. By encapsulating the FLC within smooth polymer walls separated by a distance comparable to the chiral pitch length of the FLC, we suppress the chirality of the smectic-C* (SmC*) phase and demonstrate the formation of uniform smectic-C domains. Holographic-polymer dispersed ferroelectric liquid crystals (H-PDFLCs) intrinsically exhibit faster response times when compared to nematic based H-PDLCs because of the permanent dipole of the FLC molecules. A diffractive model is also presented that adequately predicts the relative diffraction intensities of the structures.

5.2 Methods and Materials

Holographic-polymer dispersed ferroelectric liquid crystal films were formed from a mixture of fluorinated ferroelectric liquid crystal (*3M Company*, St. Paul, MN) and ultraviolet (UV) light curable monomer (PN393, *EM Industries*, Hawthorne, NY). The refractive index of the polymer was given to be $n_p = 1.473$. The FLC mixture consisted of a non-chiral component (7O]1222[6-]) and a chiral

component (81222[7F8-]) combined in a 1:2 weight ratio; the chemical structure of these constituents are shown in Figure 5.1. The FLC exhibited a stable SmC* phase from 20 °C to 64.8 °C, and was soluble in the pre-polymer. In the bulk state, the FLC possesses a helical or SmC* pitch of $\sim$2 μm, a cone angle $\varphi \sim 23.7°$, a spontaneous polarization of 28.8 nC/cm^2, an extraordinary index of refraction $n_e = 1.55$, and an ordinary index of refraction $n_o = 1.46$. Additionally, the bulk FLC exhibited the following phase transition temperatures from the smectic-C* phase to the smectic-A (SmA) and isotropic phases: SmC* (64.8 °C) SmA (88.1 °C) I.

A homogenous mixture of the pre-polymer and fluorinated ferroelectric liquid crystal was sandwiched between two glass substrates having indium tin oxide (ITO) conducting transparent electrode layers; a uniform film cell gap ($d \sim 5$ μm), was controlled by glass fiber spacers. Samples were exposed to a two-beam amplitude interference pattern generated from an Ar^+ laser ($\lambda = 351$ nm) with equal power distribution between the two beams (15 mW/cm^2 each). The pitch (Λ) of the formed grating is governed by the Bragg condition: $\Lambda = \lambda/2 \sin \alpha$, where λ and α are the wavelength and half angle between the writing beams, respectively [45]. The H-PDFLC samples detailed in this contribution were fabricated from two different weight ratios of FLC and pre-polymer – a 50:50 and a 40:60 mixture of FLC and pre-polymer.

5.3 Atomic Force Microscopy

Following the holographic exposure, H-PDFLC samples, of pitch lengths $\sim$2 μm, were prepared for atomic force microscopy (AFM) imaging to investigate the polymer morphology. Samples were prepared using a freeze fracture and solvent evaporation technique (whereby the cell is frozen, the top substrate is physically lifted off, and the liquid crystal is washed away with a solvent) to remove the FLC material and leave behind the polymer features on an open-faced substrate. It should be noted that a small degree of polymer layer shrinkage may occur during this process of sample preparation. AFM imaging shows distinct morphological differences between the H-PDFLC gratings formed from

Component 7O]1222[6-]

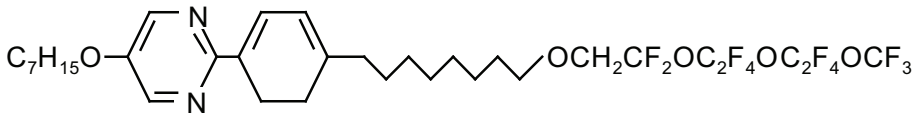

Component 81222[7F8-]

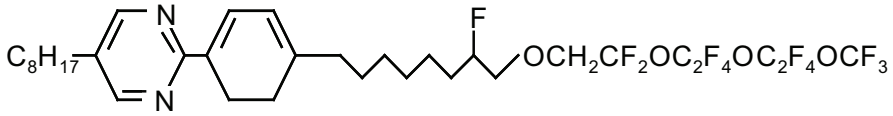

Figure 5.1: Chemical structure of the two components that comprise the fluorinated ferroelectric liquid crystal.

a 50:50 weight ratio of FLC and pre-polymer and a 40:60 weight ratio of FLC and pre-polymer, as evidenced by Figures 5.2 and 5.3, respectively. The morphology of the 50:50 mixture is of a droplet type, where voids in the polymer structure indicate FLC rich regions removed by the solvent prior to imaging. These voids have random shapes and sizes on the order of $\frac{\Lambda}{4}$ to $\frac{\Lambda}{2}$ of the grating pitch. While a polymer grating structure is still evident in Figure 5.2, the lack of well-defined uniform features is strongly apparent. This can be attributed to a low degree of phase separation between the FLC and polymer during the holographic exposure, or from an over-loading of the FLC into the pre-polymer mixture.

In comparison, the H-PDFLC grating formed from the 40:60 mixture of FLC and pre-polymer shows a pronounced phase separation and a smooth layer-like morphology, as shown in Figure 5.2. These layers, or voids in the AFM image, reveal the locations of the FLC rich regions removed by the solvent prior to imaging. From the AFM results, it is impossible to verify the alignment geometry of the FLC in these two structures, as the FLC has been removed. While both of the resulting morphologies are fundamentally intriguing, the remainder of this contribution will focus entirely on the gratings formed from the 40:60 mixture of pre-polymer and FLC that results in a smooth layer morphology.

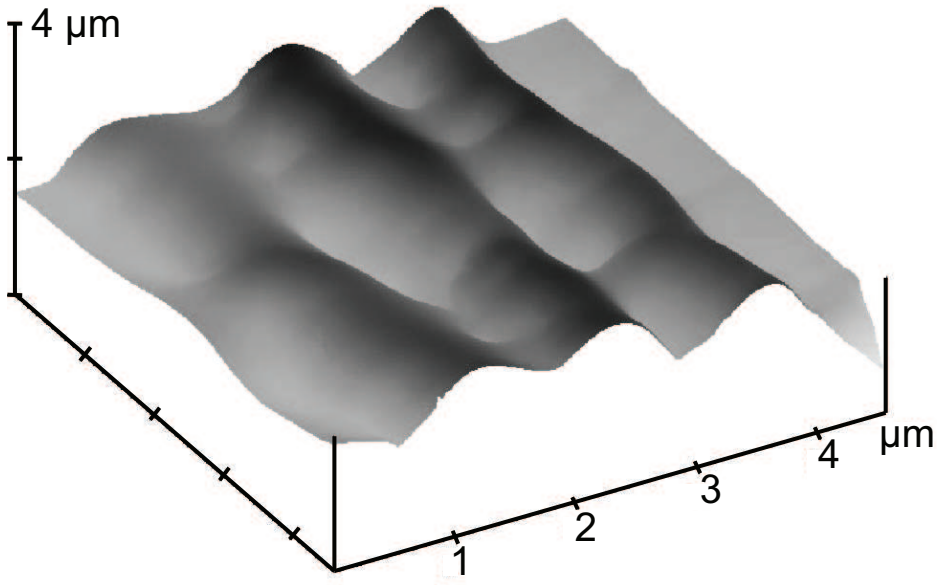

Figure 5.2: Atomic force microscopy (AFM) image of a holographic polymer dispersed ferroelectric liquid crystal (H-PDFLC) formed using a 50:50 mixture of FLC and pre-polymer. A droplet morphology is shown, which produces a random FLC alignment.

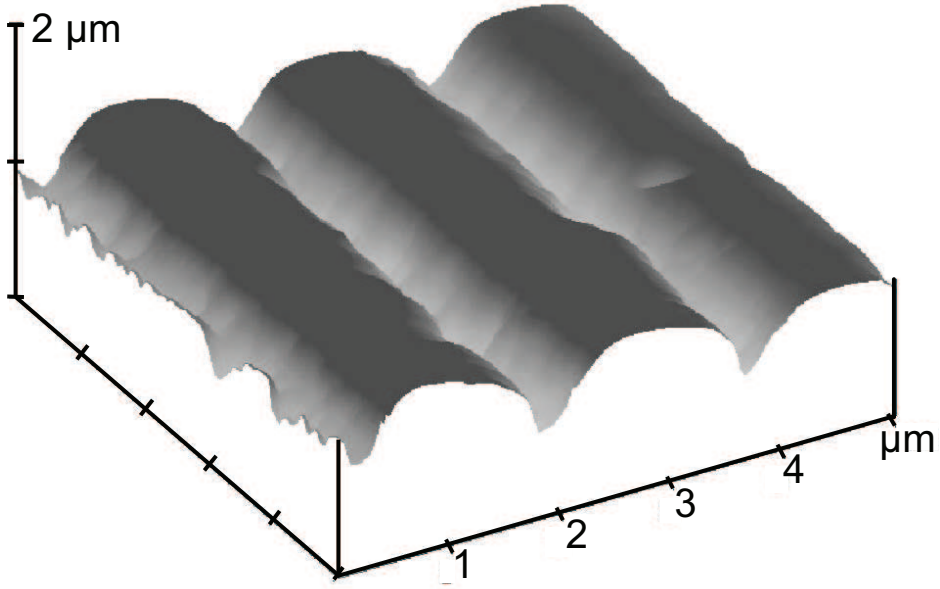

Figure 5.3: Atomic force microscopy (AFM) image of a H-PDFLC formed using a 40:60 mixture of FLC and pre-polymer. A layer morphology in shown, which produces a uniform FLC alignment.

5.4 Optical Polarizing Microscopy Analysis

Holographic polymer dispersed ferroelectric liquid crystal gratings were next fabricated from a 40:60 mixture of FLC and pre-polymer with grating pitches of $\Lambda \sim 3.32$, 7.40, and 11.3 μm to investigate the FLC alignment in the layer morphology. Optical polarizing microscopy was used to distinguish differences in the FLC alignment by measuring an intensity ratio of the grating at $\theta = 0°$ and $\theta = 45°$ between crossed polarizers, where θ is the angle between the polarizer axis and the preferred FLC director, as defined in Figure 5.4. Optical microscopy images of the three different pitch sizes oriented at $\theta = 0°$ and $\theta = 45°$ are shown in Figure 5.4.

When the grating is aligned at $\theta = 0°$ with respect to the crossed polarizers, there is little optical contrast between the FLC rich planes and the polymer walls. This is attributed to the uniform planar alignment of the FLC domains, as shown for a $\Lambda \sim 3.32$ μm H-PDFLC grating in Figure 5.4. As the grating is rotated to $\theta = 45°$ between crossed polarizers, the optical contrast between the FLC rich planes and polymer walls increases, as shown in Figure 5.4(b). The FLC rich planes are bright, indicating the average director alignment is highly aligned at an angle between the polarizers; meanwhile, the polymer walls remain dark, verifying the polymerized network is isotropic in nature. The presence of some residual FLC in the polymer planes results in a non-ideal dark state in these regions. The continuously uniform FLC alignment is thus the result of the smooth layer formed during the holographic exposure and verified in the AFM image in Figure 5.3.

5.5 Zero-order Transmission

For a more complete account of the director deviations in the layer morphology, the H-PDFLC gratings were probed between crossed polarizers using a helium-neon laser ($\Lambda = 633$ nm). As the grating is rotated in the azimuthal plane, the transmitted intensity is recorded using a photodiode connected to a broadband amplifier. A plot of the transmitted intensity as a function of azimuthal angle for different pitch sizes is shown in Figure 5.5. Taking into account the distribution of domain

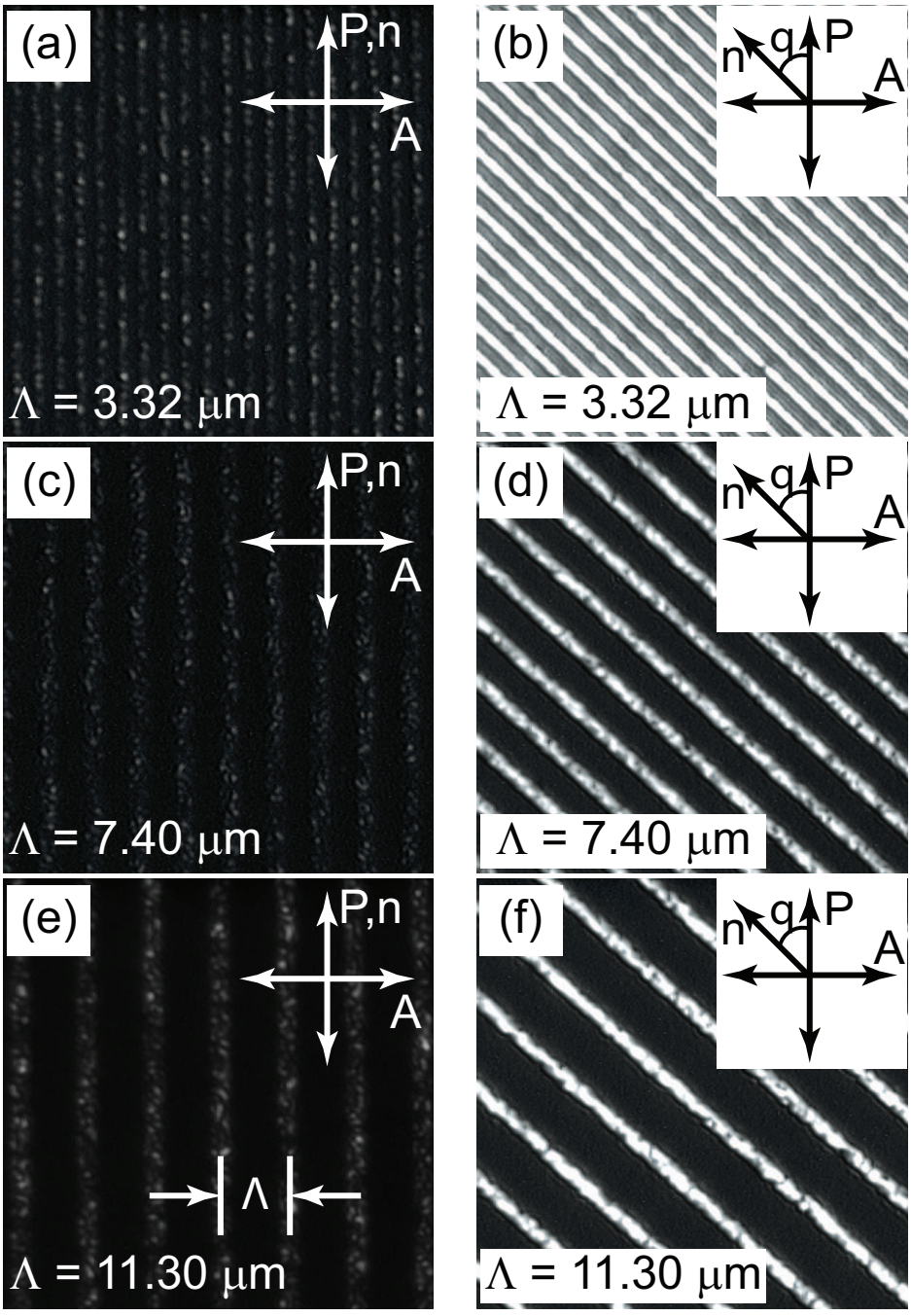

Figure 5.4: Optical polarizing microscopy images of different pitch length H-PDFLCs oriented at $\theta = 0^\circ$ and $\theta = 45^\circ$ between crossed polarizers.

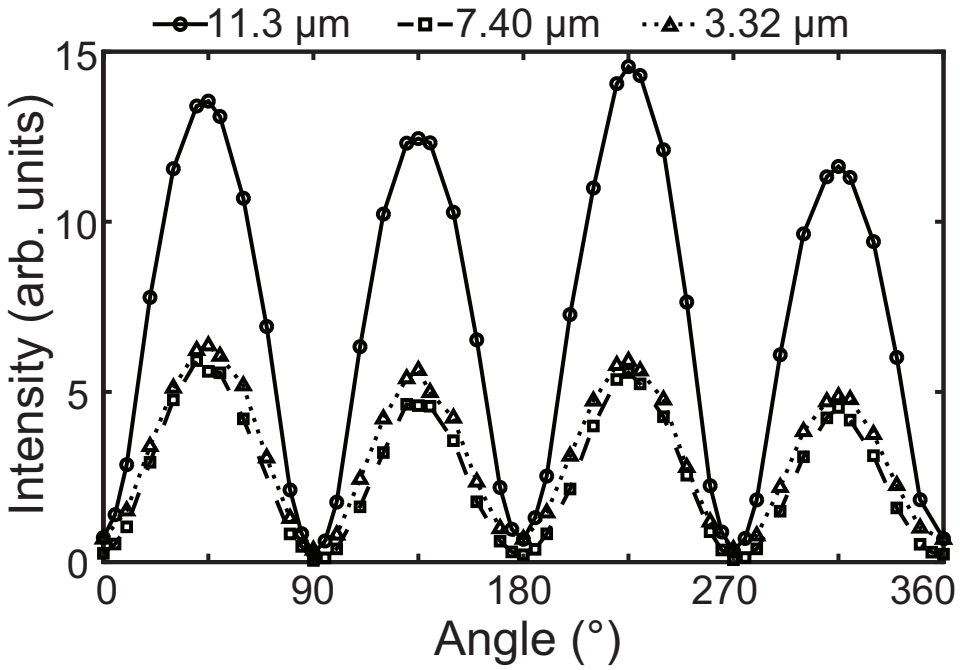

Figure 5.5: Zero order transmission through an H-PDFLC grating between crossed polarizers as the grating is rotated relative to the crossed polarizer axes.

orientations, we can express the transmitted intensity, I, as:

$$I = I_0\left(d, \Delta n, \lambda\right)\left\langle \sin^2 2\left(\Delta\Theta + \theta\right)\right\rangle \tag{5.1}$$

where I_0 is a measure of the amplitude of the intensity and is a function of, d, the cell thickness, Δn, the birefringence of the liquid crystal, and λ, the wavelength of light probing the sample. The sinusoidal term takes into account the average variation in the FLC domain orientations away from the preferred director; $\theta + \Delta\Theta$ is the angle between the FLC domain directors and polarizer axis. Assuming $\left\langle \Delta\Theta^2 \right\rangle \ll 1$ for all pitch sizes, we can express the transmitted intensity as being proportional to the angle θ and the average domain director deviation $\left\langle \Delta\Theta^2 \right\rangle$:

$$I \propto \sin^2 2\theta + 4\cos 4\theta \left\langle \Delta\Theta^2 \right\rangle, \tag{5.2}$$

which reduces to:

Pitch (μm)	I_{max}/I_{min}	$\langle\Delta\Theta^2\rangle$ (radians^2)
3.32 ± 0.12	48.9 ± 6.5	0.005 ± 0.001
7.40 ± 0.16	13.6 ± 3.3	0.017 ± 0.004
11.30 ± 0.36	8.75 ± 3.1	0.026 ± 0.006

Table 5.1: Calculated average domain orientation deviations for H-PDFLCs of different pitches.

$$I \propto 1 - \left(1 - 8\left\langle\Delta\Theta^2\right\rangle\right)\cos 4\theta. \tag{5.3}$$

By assuming the FLC director only deviates from a direction parallel to the polymer walls, the maximum transmitted intensity (I_{max}) occurs when $\theta = 45°$ and a minimum transmitted intensity (I_{min}) occurs when $\theta = 0°$. The ratio of I_{max}/I_{min} can be written as:

$$\frac{I_{max}}{I_{min}} = \left[\frac{1 + (1 - 8\left\langle\Delta\Theta^2\right\rangle}{1 - (1 - 8\left\langle\Delta\Theta^2\right\rangle}\right]. \tag{5.4}$$

This relationship between maximum and minimum intensities was also visible in the polarizing microscopy images. As the grating pitch increases, the less uniform FLC alignment is apparent, as observed in Figure 5.4. A loss in brightness corresponds to a less ordered director aligned along the layer. We quantitatively describe these results by summing over the total intensity for each pixel in each of the microscopy images and comparing counts for the $\theta = 0°$ and $\theta = 45°$ cases. The ratio between the bright ($\theta = 45°$)and dark ($\theta = 0°$) cases decreased with increasing pitch size from 48.9 ± 6.5 for $\Lambda \sim 3.32$ μm to 13.6 ± 3.3 for $\Lambda \sim 7.40$ μm and 8.75 ± 3.1 for $\Lambda \sim 11.3$ μm, as shown in Table 5.1. These microscopy results suggest the FLC domains are formed within the layers, but the domain directors can deviate from the preferred FLC director alignment within the layers, which is parallel to the polymer walls. By measuring the pixel intensity of the images, we qualitatively show how the director deviations determine the optical texture in the microcopy images. We can rewrite Equation 5.4 to solve for the FLC domain deviations $\left\langle\Delta\Theta^2\right\rangle$ in each of the three pitch sizes:

$$\left\langle\Delta\Theta^2\right\rangle = \frac{1}{4}\left(\frac{\mathrm{I_{max}}}{\mathrm{I_{min}}} + 1\right)^{-1}. \tag{5.5}$$

The experimental results for the average domain orientation deviations increase from 0.005±0.001 to 0.026±0.006 square radians as the pitch increases from $\Lambda = 3.32 \pm 0.12$ μm to $\Lambda = 11.30 \pm 0.36$ μm, as shown in Table 5.1; the initial assumption of $\langle \Delta\Theta^2 \rangle \ll 1$ is still valid. The increasing spread in the distribution of domain orientations with increasing pitch size is attributed to the degree of phase separation that occurs during the photopolymerization process and will be further discussed in the following section.

5.6 FLC Alignment Model

The discussion above relates only to static measurements and provides insight into the FLC domain alignment in the absence of an external field. We expand on the idea of a uniform domain alignment encapsulated by smooth channels to develop a phenomenological model in the context of a phase grating. The phase grating results from the periodically patterned UV illumination and is characterized by a pitch Λ. The non-uniform photo-induced phase separation of this holographic exposure yields a periodic array of polymer rich layers of width ($c_{\text{poly}}\Lambda$) normal to the glass substrates, where c_{poly} is a relative width of the polymer walls with respect to the total pitch Λ, as depicted in Figure 5.6. During the holographic exposure the space in-between the polymer walls becomes more liquid crystalline as the FLC counter diffuses into the low intensity regions of the interference pattern. As the holographic exposure is completed, FLC rich layers emerge between the polymer walls, having a thickness of $(1 - c_{\text{poly}})\Lambda$. Congruent with the optical polarizing microscopy investigation, we assume the FLC molecules orient parallel to the cell surfaces and parallel to the internal polymer interfaces. In the case of perfect polymer separation, the small-scale confinement of the polymer walls is comparable in size to the SmC* pitch. In assuming very strong anchoring on the substrates and rather strong coupling on the polymer wall interfaces, the SmC* helical structure prefers to unwind, restricting the director to uniformly align parallel to the polymer walls. Taking

this geometry into account, there is equal probability the smectic planes will make an angle equivalent to the tilt angle, either φ or $(180^\circ - \varphi)$ against the preferred FLC director. In our case the tilt angle φ is $\sim 23^\circ$. Half of the FLC domains will have polarization along the +z axis and half down along the -z-axis, as represented in the schematic illustration in Figure 5.6. When an electric field is applied across the sample, only those domains whose polarization are anti-parallel to the applied field will switch.

In real systems polymer separation is not complete, some of polymer network remains in the FLC-rich layers and yields a local perturbation in the domain director orientation. Particularly with increasing pitch length at a constant polymerization rate, when the polymer separation becomes diffusion limited, we expect a pronounced increase in the disorder of domains. This is consistent with the increased spread of the alignment $\langle \Delta\Theta^2 \rangle$ observed with polarization microscopy (Table 5.1).

The experiments demonstrate a rather uniform FLC alignment in the context of solid surface anchoring and polymer wall confinement. For our phenomenological model, this is a good approximation. However, for a more complete understanding, more complicated effects occurring during the photo-induced phase separation process should be considered. For instance, it is reasonable to assume that shrinkage of the polymer matrix occurs during photopolymerization and creates stress and shear tensors on the polymer depleted regions, as they become FLC rich planes. It is possible that these shear forces can also play a pivotal role in the uniform FLC alignment, along with the confinement and anchoring effects. In fact, shear alignment has been shown to align the FLC director perpendicular to the shear direction [65, 73].

5.7 Zero-order Transmission

In the presence of an external electric field, the FLC domain orientation can be expressed as a collective motion of molecules from one side of the cone angle to the other as the dipole moment aligns in the direction of the electric field. We can introduce a function, $Y(E)$, to represent a relative

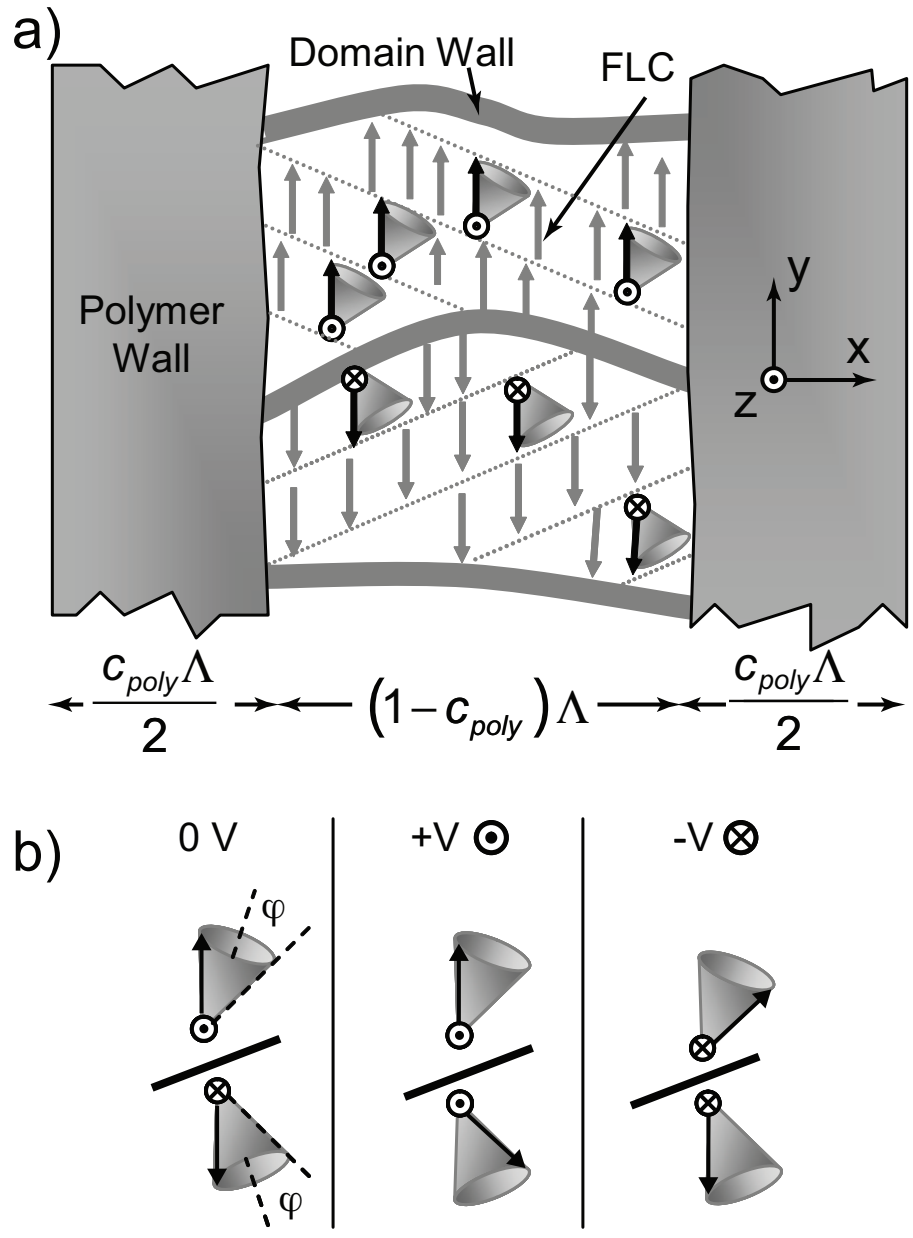

Figure 5.6: Schematic illustration of FLC alignment between polymer walls in a H-PDFLC grating.

measure of the FLC domains that have already switched in the electric field. Assuming the FLC director aligns parallel to the polymer walls, we can neglect out of plane director misalignment. Given, the distribution of domains with positive or negative polarization along the z-axis, only half of the domains switch, those with a polarization anti-parallel to the applied field. The transmitted average intensity can be writen as:

$$\frac{I\left(\theta=0,E\right)}{I_0}=\frac{1}{2}\left[2-Y\left(E\right)\right]+\frac{I_{2\varphi}}{I_0}Y\left(E\right), \tag{5.6}$$

where $I_0 = I\left(\theta = 0^\circ, E = 0\right)$ and $I_0 = I\left(\theta = 2\varphi, E = 0\right)$ are experimentally determined values of the zero-field transmitted intensity when the sample is oriented at $\theta = 0^\circ$ and $\theta = 2\varphi$ (φ being the half cone angle of the FLC) between crossed polarizers. The ratios I_{max}/I_{min} are taken to be the same as the ratios calculated from Figure 5.5 and given in Table 5.1. It should be noted that the values of this ratio do contain a rather significant degree of error, attributed to the quality of the sample at various spots across the grating. Multiple measurements were made of this ratio over several spots on the grating; the error introduced by this value will become significant in the following section.

The zero order transmission through an H-PDFLC grating between crossed polarizers was measured as a function of applied voltage for incident s-polarization and p-polarization. We define s-polarization as the polarization component parallel to the polymer walls, along the y-axis in Figure 5.6(a); and p-polarization as the polarization component perpendicular to the polymer walls, along the x-axis in Figure 5.6(a). The experimental plots of the normalized zero order transmission intensity as a function of applied field for the three pitch sizes are shown in Figure 5.7. The data was normalized such that the maximum intensity was set to one. In all gratings we observe an increase in intensity with optical saturation occurring at or above $\sim$15 V/μm. The greatest contrast between bright (field-on) and dark (field-off) states occurs in the smallest pitch cells for incident s-polarization and p-polarization. The coupling between the permanent dipole and applied field is assumed to be dominant, as compared to the dielectric coupling, and supports a zero or low threshold behavior.

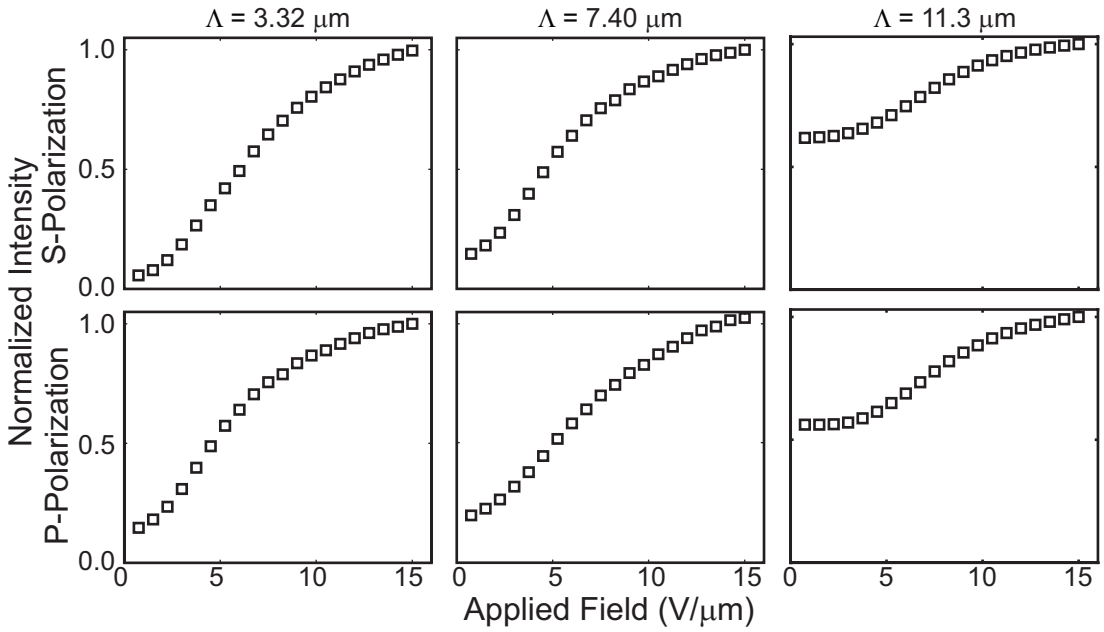

Figure 5.7: Normalized zero order transmission data with incident s-polarization and p-polarization as a function of applied electric field.

From the zero-order electro-optic switching curves, $I(E)$, for incident s-polarization, Figure 5.7, we can make use of Equation 5.6 to determine $Y(E)$ from the experimental results for each pitch size as:

$$Y\left(E\right) = \frac{2\left(I(E)/I_0 - 1\right)}{\left(I_{2\varphi}/I_0 - 1\right)}. \tag{5.7}$$

I_0 is chosen to be the minimum relative intensity in the zero order data and $I_{2\varphi}/I_0$) are the values of $I_{\max}/I_{\min}$ given in Table 5.1.

The function $Y(E)$ could also be determined theoretically as it is also relates to the distribution of FLC domain sizes $dN/d\zeta$ between the polymer walls:

$$Y(E) = \int_{\zeta_c}^{\infty} \alpha\zeta^3 \frac{dN}{d\zeta} d\zeta, \tag{5.8}$$

where ζ is a characteristic size; the domain volume is expressed as ζ^3; $\zeta_c(E) = (K/EP)^{1/2}$ is the

minimum switchable domain size for an applied field E; K and P are the intrinsic elastic constant and polarization of the FLC, respectively; and a is used as a normalization constant. For this contribution, we determine *Y(E)* experimentally from transmission data.

5.8 First-order Transmission

Using the zero order transmission data, we predict the behavior of the first order diffraction intensity for incident s-polarization and p-polarization as an electric field is applied from $0 - 15$ V/μm. As mentioned earlier, the H-PDFLC grating can be modeled as a phase grating, with a periodicity of Λ, within the context of diffraction theory. Incident light on the phase grating will experience a phase shift from the polymer regions, ϕ_{poly}, and a phase shift in the FLC rich regions, ϕ_{FLC}. We have shown, through optical polarizing microscopy, that the photo-polymerized walls have an isotropic refractive index; the phase shift in the polymer is independent on the polarization direction and can be expressed as: $\phi_{\text{poly}} = 2\pi n_{\text{poly}} d/\lambda$. The phase shift in the FLC region is highly dependent on the alignment of the FLC domains and the polarization of the incident light; this phase shift is expressed by: $\phi_{\text{FLC}} = 2\pi n_{\text{FLC}} d/\lambda$, where n_{FLC} is a value somewhere in-between the ordinary and extraordinary indices of refraction of the FLC – and depends on sample orientation. Reorienting the FLC domains with an external field or rotating the sample relative to the incident polarization can manipulate the scalar value of the phase shift.

Within the context of diffraction theory, the diffraction from a phase grating with N slits can be written as a product of the grating factor:

$$H(x) = \left(\frac{\sin Nx}{\sin x}\right)^2 \tag{5.9}$$

and the slit factor:

$$J(x) = \left| C \int_0^1 \exp(-i\phi(\xi) - i2x\xi) d\xi \right|^2 , \tag{5.10}$$

where the dependence on the diffraction angle, β, is hidden in the integral diffraction order:

$$x = \left(\frac{\pi \Lambda}{\lambda} \sin \beta \right), \tag{5.11}$$

and $\phi(\xi)$ is a step-wise function defining the phase shift acquired by light passing through the polymer or FLC regions at ξ, a relative position within a slit.

Further, we assume the FLC alignment uniformly propagates through the depth of the grating, and the light incident on the grating can be separated into its extraordinary and ordinary ray components with their corresponding phase shifts: $\phi_{||} = 2\pi n_e d/\lambda$ and $\phi_{\perp} = 2\pi n_o d/\lambda$, respectively. This assumption is based on previously captured SEM photographs [71, 72], which clearly depict the fully separated polymer and FLC layers through the depth of the grating in a 40:60 H-PDFLC mixture.

The $\phi_{||}$ phase shift corresponds to incident s-polarization – parallel to both the polymer walls and long axis of the FLC; the $\phi_{\perp}$ phase shift corresponds to incident p-polarization – perpendicular to both the polymer walls and long axis of the FLC. At the first order diffraction maxima, occurring when $\xi = \pi$, the zero-field intensity, J, can be written as:

$$J \propto \sin^2 (\phi_{\mathrm{FLC}} - \phi_{\mathrm{poly}}) \sin^2 (\pi c_{\mathrm{poly}}) , \tag{5.12}$$

taking into account the step-wise nature of $\phi_(\xi)$. The diffracted intensity J is dependent on the incident polarization direction and can be expressed, in terms of the ordinary and extraordinary refractive indices of the FLC, as two separate terms:

$$J_{||} \propto \sin^2 \left(\frac{\pi d}{\lambda} (n_e - n_p) \right) \sin^2 (\pi c_{\mathrm{poly}}) \tag{5.13}$$

$$J_{\perp} \propto \sin^2\left(\frac{\pi d}{\lambda}\left(n_o - n_p\right)\right)\sin^2\left(\pi c_{\text{poly}}\right) \tag{5.14}$$

Using the experimentally determined or previously reported values of the refractive indices n_e, n_o, n_p, cell thickness d, and incident wavelength λ, the ratio between these two values is determined to be $J_{\perp}/J_{||} \sim 0.11 \pm 0.03$, with error introduced by uncertainties in the film thickness and FLC refractive indices in solution. The values of the refractive index are subject to error given the likelihood of an incomplete phase separation of the FLC and polymer during the polymerization process.

The material and sample properties appearing in Equations 5.13 and 5.14 have a significant impact on the diffraction intensities of the fabricated H-PDFLCs. In the ideal case, the $J_{\perp}/J_{||}$ ratio would be minimized – accomplished through either index matching n_o and n_p, or by choosing an appropriate cell gap so as to minimize the first term of Equation 5.14. Such an optimization would enhance the electro-optic diffractive properties of the film.

In general, given that the director, which is parallel to $J_{||}$, makes an angle $\Delta\Theta + \theta$ with the incident polarization direction, we can write the average diffracted intensity as:

$$\langle I_{\text{diff}} \rangle \propto J_{||}\left\langle \cos^2\left(\theta + \Delta\Theta\right)\right\rangle + J_{\perp}\left\langle \sin^2\left(\theta + \Delta\Theta\right)\right\rangle \tag{5.15}$$

or:

$$\langle I_{\text{diff}} \rangle \propto J_{||} - \left(J_{||} - J_{\perp}\right)\left[\sin^2\left(\theta\right) + \cos\left(2\theta\right)\left\langle \sin^2\left(\Delta\Theta\right)\right\rangle\right], \tag{5.16}$$

where θ is the angle between the FLC director and the crossed polarizer axes.

We can express the relative diffraction intensity (relative to the intensity $J_{||}$) for incident s-polarization ($\theta = 0°$) and p-polarization ($\theta = 90°$) as:

$$\frac{\left\langle I_{\text{diff}}^{(\text{s})} \right\rangle}{J_{||}} \propto 1 - \left(1 - \frac{J_{\perp}}{J_{||}}\right) \left\langle \sin^2(\Delta\Theta) \right\rangle \tag{5.17}$$

and

$$\frac{\left\langle I_{\text{diff}}^{(\text{p})} \right\rangle}{J_{||}} \propto \frac{J_{\perp}}{J_{||}} + \left(1 - \frac{J_{\perp}}{J_{||}}\right) \left\langle \sin^2(\Delta\Theta) \right\rangle . \tag{5.18}$$

As an external electric field is applied across the phase grating, half of the FLC domains between the polymer walls switch on the cone angle (2φ). We can predict the behavior of the first order diffraction using the function $Y(E)$, which was introduced in the zero-order transmission description. We again use the small angle approximation and assume

$$\left\langle \sin^2(\Delta\Theta) \right\rangle \approx \left\langle \Delta\Theta^2 \right\rangle \tag{5.19}$$

which enables the relative diffraction intensities to be rewritten as:

$$\frac{\left\langle I_{\text{diff}}^{(\text{s})}(E) \right\rangle}{J_{||}} \propto 1 - \left(1 - \frac{J_{\perp}}{J_{||}}\right) \left\langle \Delta\Theta^2 \right\rangle - \left(1 - \frac{J_{\perp}}{J_{||}}\right) \left(\sin^2(2\varphi) - \left\langle \Delta\Theta^2 \right\rangle\right) \frac{Y(E)}{2} \tag{5.20}$$

and

$$\frac{\left\langle I_{\text{diff}}^{(\text{p})}(E) \right\rangle}{J_{||}} \propto \frac{J_{\perp}}{J_{||}} + \left(1 - \frac{J_{\perp}}{J_{||}}\right) \left\langle \Delta\Theta^2 \right\rangle - \left\{1 - \left(1 - \frac{J_{\perp}}{J_{||}}\right) \left[\sin^2(2\varphi) + \left\langle \Delta\Theta^2 \right\rangle\right]\right\} \frac{Y(E)}{2}, \tag{5.21}$$

where $J_{||}/J_{\perp} \sim 0.11 \pm 0.03$, as from above; the angle φ is the half cone angle of the FLC, $\sim 23°$; and the pitch dependent values for $\left\langle \Delta\Theta^2 \right\rangle$ are given in Table 5.1.

The normalized experimental results and fit of the model for the first order diffraction for incident s- and p-polarizations are shown in Figure 5.8. Both the data and model were normalized to have

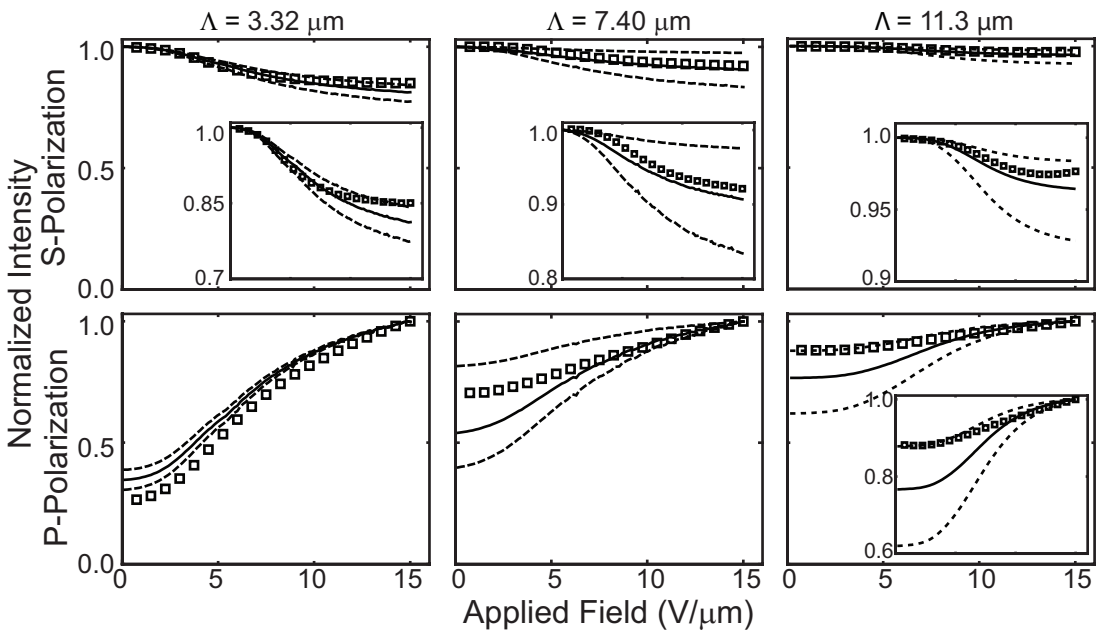

Figure 5.8: First order diffraction data () for incident s- and p-polarization. The zero-order s-polarization transmission data was used to model and predict the behavior of the first order diffraction (solid lines), along with an error bar for the model (dashed lines). The insets are magnifications of their respective subplots and clearly show the differences between the model and experimental results.

a maximum intensity of one; no other arbitrary fitting parameters were used. Several of the subfigures contain insets of magnifications of the results, so as to more clearly represent the differences between the model and the experimental results. The model, as represented by the lines in each of the plots, correctly extrapolates the trends in the first order diffraction intensities, to within a reasonable approximation. The deviations in the amplitudes of these trends from the observed experimental results are most likely caused by inaccuracies in the experimentally determined values of $I_{\max}/I_{\min}$, which were used to calculate the function $Y(E)$. Maximum and minimum values for the ratios $I_{\min}/I_{\max}$ were calculated from the results shown in Figure 5.5 and the results of the model's predictions of the first order diffracted intensity using these values are shown as dashed lines in Figure 5.8. These maximum and minimum values represent a significant error bar for the model's predictions, but the experimental results almost entirely fall within these ranges.

The contrasting diffraction intensity trends for s- and p-polarization observed in Figure 5.8 are

the result of the FLC domains switching on the cone and modifying the phase mismatch between the FLC and polymer layers. The diffracted intensity for incident s-polarization decreases as a voltage is applied across the grating. Given the refractive indices for the FLC ($n_e = 1.53$, $n_o = 1.49$) and polymer ($n_p = 1.473$), and the geometry described in Figure 5.6, the grating effectively becomes transparent with an increasing field. At zero field, the FLC domains are highly aligned between the polymer walls and present an index modulation between n_e and n_p; as the field increases a large number of FLC domains switch on the cone angle (2φ) and reduce the refractive index modulation. The relative change in diffracted intensity is also shown to decrease with increasing pitch sizes. This is attributed to a decrease in the refractive index modulation brought on by a less complete phase separation and a larger orientational disorder in the larger pitch samples. The relative change in diffraction intensity, however, is limited for incident s-polarization. In the ideal scenario, the values $\langle \Delta\Theta^2 \rangle$ and $J_\perp / J_{||}$ would approach zero and Equation 5.20 would reduce to:

$$\frac{\left\langle I_{\text{diff}}^{(\text{s})}(E) \right\rangle}{J_{||}} \propto 1 - \sin^2(2\varphi)\frac{Y(E)}{2} \tag{5.22}$$

Given the cone angle $\varphi \sim 23^\circ$ and the normalization condition that the function $Y(E)$ approaches one in the infinite field regime, the maximum possible relative diffracted intensity for s-polarization becomes ~75% of the zero field diffracted intensity, a change of 25%. In the non-ideal physical systems, the maximum relative change in diffraction intensity of ~12% of the zero field intensity is observed in the smallest grating pitch at an applied field strength of 15 V/μm. Incident s-polarization is not ideal for any device applications where a high contrast between field-off and field-on states is needed.

Conversely, when p-polarization is incident on the grating, we observe an increase in diffraction intensity with increasing applied field strength. This is a result of a small effective refractive index modulation between the FLC domains and the polymer at zero field. As the field increases, the FLC

domains switch on the cone angle, increasing the refractive index modulation and effectively 'turn-on' the grating. The change in relative diffracted intensity decreases as the pitch length increases and is attributed to a larger distribution of domain orientations, as reported earlier.

Just as was observed for incident s-polarization, the switching performance for first order diffraction with incident p-polarization can also be investigated. Here, in the ideal case, Equation 5.21 reduces to:

$$\frac{\left\langle I_{\text{diff}}^{(\text{p})}(E)\right\rangle}{J_{||}} \propto \left\{1-\sin^2(2\varphi)\right\}\frac{Y(E)}{2}. \tag{5.23}$$

Thus, we observe that the intensity of the first order diffraction peak can theoretically increase by a factor depending on the cone angle of the FLC and the material and cell properties contained within the function $Y(E)$ (Equation 5.7). This phenomenon offers the potential for greater contrast ratios between field-on and field-off states, as compared to those resulting from incident s-polarization states. In utilizing these types of films for device applications, careful material and film optimizations must be performed so the device performs as close to the theoretical limits as possible.

Along this vein, the diffraction efficiency was also calculated for each grating period by: $\eta = \ell_1/(\ell_0+\ell_1)$ where ℓ_0 is the intensity of the zero-order transmission at zero field, and is the intensity of the first order diffraction peak. The diffraction efficiencies for the Λ = 3.32, 7.40, and 11.30 μm samples were calculated to be: for incident s-polarization, approximately 11.9%, 6.0% and 5.0%, respectively, and 0.04%, 2.1%, and 2.6% for incident p-polarizations. These zero-field diffraction efficiencies, which may be too low for any electro-optic switching applications, are the result of the low index modulation of the FLC-polymer composite material. Our H-PDFLCs were not optimized to exhibit high diffraction efficiency, but through careful materials selection and cell optimization, these diffraction efficiencies can be significantly increased.

5.9 Dynamic Switching Response

Finally, dynamic responses were also measured for the three grating pitches, to evaluate the response-time and relaxation-time as a function of applied field. Two different waveform pulses were applied: a positive DC bias ($0 \rightarrow +V$) and a negative DC bias ($0 \rightarrow -V$), each at a frequency of 200 Hz. The FLC adequately responds to the DC fields at this frequency and no charge effects are observed. Measurements for both positive and negative applied fields were made in order to compare the dynamic response of the cone-up and cone-down domains. The response time measurements were recorded between $10 - 90\%$ of optical saturation for applied fields ranging from 8 V/μm to 20 V/μm. The experimental data for the electro-optic response and relaxation time, Figure 5.9(a), shows a decrease in both response time and relaxation time as the field strength is increased. At lower voltages we observe faster response times for larger pitch samples; the opposite case is true for confined nematics, where higher thresholds and faster response times result from an increased polymer confinement [58]. However, at higher voltages, we show that response times for various pitch lengths do converge to a value of $10 - 20$ μs. These response times are noticeably faster than the reported response times of nematic based H-PDLCs.

The relaxation times of the H-PDFLC systems are significantly improved over nematic H-PDLCs and lend further credence to the potential for H-PDFLCs as rapidly switchable diffractive optics or as tools for rapid light shutter applications. There is, however, a field dependence on the relaxation time, which is not observed in other liquid crystalline systems. This phenomenon in attributed to the domain structure of the FLC layers. At higher field strengths, the FLC molecules are more fully aligned and seem to have a tendency to relax much more rapidly as a whole. At lower field strengths, the relaxation processes occur at a slower rate. This phenomenon is evidenced by a lack of a simple exponential decay in the transmitted intensity once the field has been removed, as shown in Figure 5.9(b). Here, the logarithm of the intensity as a function of time after the field has been removed is plotted for the 7.4 μm grating pitch film. In a bulk liquid crystal, a field

independent exponential decay is expected; however, this is not observed for the H-PDFLC films. The non-linearity in Figure 5.9(b) represents a non-exponential decay. Further investigations may shed greater light on the dynamic processes dictating these observations.

5.10 Conclusion

We have demonstrated the fabrication of H-PDFLCs using ferroelectric liquid crystals. The morphology that results from the phase separation process creates smooth polymer layers for a uniform alignment of FLC domains, as verified through optical polarizing microscopy. The resulting FLC alignment from this photo-induced phase separation creates uniform domains, where the preferred FLC director is oriented parallel to the polymer walls. Deviations in the domain distribution that occur as the pitch length increases are calculated experimentally through zero-order transmission data and within small angle approximations.

The polarization dependence of the zero-order transmission data, allows us to effectively model the H-PDFLC as a phase grating of uniformly aligned FLC domains surrounded by polymer walls. Through a phenomenological model we use the zero-order transmission data to effectively predict the voltage dependence of the first order diffraction intensity and shape. This model is in agreement with the experimental results that show a thresholdless voltage transition and optical saturation. The microsecond electro-optic response times for H-PDFLCs are inherently faster than nematic based H-PDLCs and show potential for rapidly switchable diffractive optics applications.

To translate these systems to the application space, material optimization must be performed. Indexing matching the FLC and the polymer, as well as using an FLC with a larger birefringence, could greatly enhance the diffraction efficiencies of these systems. An optimal pitch length and cell thickness must also be determined; this, again, will depend on material properties.

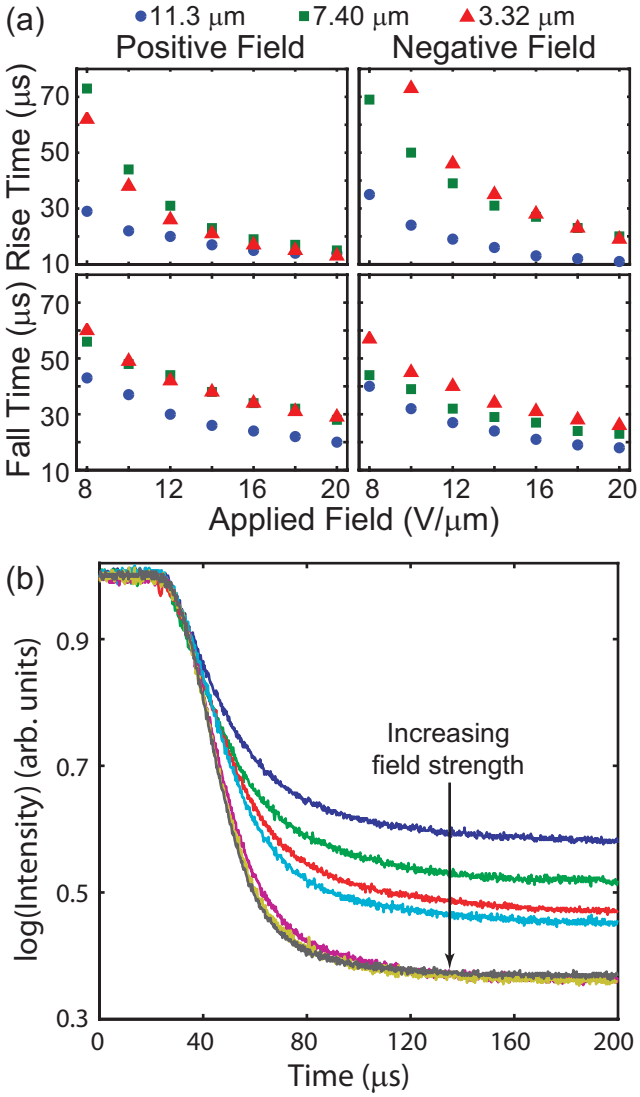

Figure 5.9: Measured response and relaxation times for the three pitch lengths as a function of applied DC fields; the field is switched from the 'on' state to the 'off' state at a frequency of 200 Hz. Only those domains with a polarization anti-parallel to the applied field will switch.

Chapter 6

Applications of Surface Patterned LC Alignment

There are many potential applications for the periodic grating structures discussed in Chapters 3 and 4. The intent of this thesis was to focus solely on the underlying physics of the unique liquid crystal configurations created using periodic alignment layers, rather than an exercise in optimization for a particular application.

There are several technologies in the literature that produce electrically switchable gratings. Holographic polymer dispersed liquid crystals (H-PDLCS) are created through a photo-induced diffusion process, where alternating layers of liquid crystal rich and polymer rich layers are formed [51,62,74]. Because of the nature of the phase separation [56,57], the switching voltages are quite high – a result of the polymer confinement. Another approach for polarization grating technology, is to add azo-dye compounds to polymers to create an index modulation [28,75]. However, azo-dye doped polymers tend to produce very small diffraction efficiencies of a few percent [28, 75]. The grating approaches presented in Chapters 3 and 4 overcome these issues as these films can be switched at relatively low voltages and the aligned liquid crystal produces a large index modulation. These

inherent advantages make surface patterned liquid crystal alignment gratings especially attractive as either passive or active optical elements in displays, photonic applications, and optical security features.

6.1 Displays

The potential to create highly efficient polarization gratings has been established by various groups [23, 24, 76, 77]. Sarkissian and co-workers have demonstrated that a thin film approximation results in a complete diffraction of normally incident light into the ± 1 diffracted orders. This has been experimentally demonstrated by Escuti and co-workers in a projection display application. Through their work, these authors have improved upon the registered planar-periodic alignment configuration though an optimization of the ratio between the grating pitch and cell thickness and thus overcome the generation of the defect lines formed in the films presented in Chapter 3. With such an optimization, the grating configuration exhibited only ± 1 diffracted orders, with minimal intensity contribution in the zero order. Likewise, the ± 1 diffracted orders are orthogonally circularly polarized, and can diffract $\sim$100% of the incident intensity when using right- or left-handed circularly polarized light.

6.2 Photonic Applications

6.2.1 Spectropolarimetry

An application of the passive one-dimensional polarization gratings using liquid crystal polymers (shown previously in Chapter 3) has been demonstrated by Escuti and co-workers [78]. In their simplified spectropolarimetry configuration, a series of three polarization gratings having a constant grating pitch with varying thicknesses were used in conjunction with two $\lambda/4$ waveplates to measure the complete Stokes parameters for an incident light source, recording four simultaneous intensities at

each wavelength. Since this simplified design does not require costly polarizers, or electro-mechanical components, the approach is cost effective and extremely robust.

6.2.2 Tunable Lasing Cavities

The periodic structure of the one-dimensional polarization gratings can also serve as a distributed feedback cavity for lasing applications. Woltman and coworkers have successfully demonstrated liquid crystal polarization grating lasers fabricated from the interference pattern of two orthogonal circularly polarized beams. The holographic exposure and materials selection were optimized such that when the liquid crystal and laser dye mixture were infiltrated into the grating configuration and optically pumped, laser emission was observed at the edge of the sample, parallel to the grating vector.

Using a frequency doubled Nd:YAG laser, with an emission line of $\lambda = 532nm$ and pulsed at a repetition rate of 10 Hz, as a pumping source Woltman and co-workers observed a narrow-band of emission $\lambda \sim 570nm$ centered at the broad florescent emission ofthe laser dye. As the pump pulse energy increased beyond a threshold value, a sharp increase in the emission line intensity along with a line narrowing down to ∼4 nm was observed, supporting the premise that the periodic structure and liquid crystal alignment serve as a gain medium for the laser dye. Upon the application of an electric field, sufficiently strong enough to align the liquid crystal in the grating along the direction of the field, the emission line could be red-shifted up to 7 nm. The implications of this thin-film lasing medium can also be applied to liquid crystal polarization gratings formed with reactive mesogen (polymeric) materials to create passive lasing films.

6.3 Optical Security Features

The polarization gratings detailed in this thesis can also be implemented as optical security features. The motivation for this type of application is driven by two separate market needs. The first market

need calls for an effective means to differentiate and authenticate pharmaceuticals from their deadly counterfeit counterparts being sold illegally. The second market need is driven by a quick, non-invasive means to monitor temperature fluctuations in blood bags during transportation.

6.3.1 Pharmaceutical Authentication Features

It is estimated that up to 15% of the word's prescription drugs are counterfeit, either by lacking in the proper amount of active ingredient or by containing the wrong active ingredient. This growing epidemic has caused serious health issues and deaths to individuals who unknowingly consume these counterfeit prescription drugs. These statistics skyrocket in underdeveloped parts of the world including Africa and Asia where it is estimated that up to 50% of the drugs on the consumer market are counterfeit. The main culprit for this epidemic is that prescription drugs lack sophisticated security elements in the packaging to authenticate a genuine product manufactured by a legitimate pharmaceutical company.

Using the thermally bi-stable smectic-A grating configuration demonstrated in Chapter 4, it is possible to create a sophisticated security feature (a thermally active hologram) on a prescription drug bottle or blister pack with thermally sensitive diffraction characteristics. In one envisioned embodiment, the SmA grating can be applied to the prescription bottle at the manufacturer in the homeotropically aligned state. Is this configuration a visible diffraction pattern is not observed. As the prescription drug is shipped to the end user, the authenticity of the drug can be probed by heating the active hologram and observing the visible diffraction patten that becomes apparent once the hologram cools back to room temperature. A schematic illustration of this process is shown in Figure 6.1.

6.3.2 Irreversible Thermometers

The medical industry is constantly searching for non-invasive methods to easily detect temperature fluctuations in blood bags during transportation. If at any point during transit the blood experiences

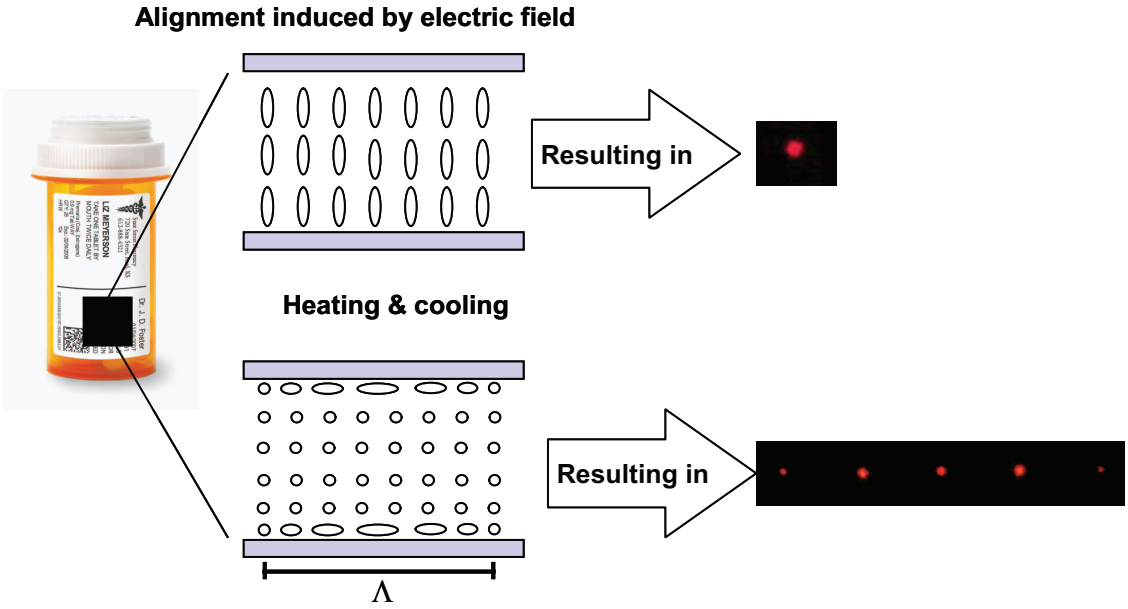

Figure 6.1: Application of an SmA liquid crystal polarization grating used as a security feature to differentiate authentic pharmaceuticals from illegal counterfeits.

a large temperature fluctuation, the possibility of coagulation is high, thus making it ineffective. For this reason, hospitals need to perform costly and time consuming diagnoses on every individual blood bag before it is given to a patient.

A cost effective, and non-invasive solution for monitoring temperature fluctuations is envisioned using a thermally bi-stable grating configuration similar to the pharmaceutical authentication feature described above. In this embodiment, a homeotropically aligned smectic grating, exhibiting no visible diffraction pattern, is attached to a blood bag prior to transportation. If the blood bag reaches the end user, and a visible diffraction pattern is not observed, the blood is deemed safe and can be used in transfusions without further testing.

If a visible diffraction pattern is present, a temperature elevation occurred during transit. While this technique only qualitatively indicates that a temperature fluctuation did occur, it is unclear whether the fluctuation was severe enough to induce coagulation. Further laboratory testing will be needed to quantitatively inspect the quality of the blood before it is used. A schematic illustration of an irreversible thermometer for blood bag applications is shown in Figure 6.2

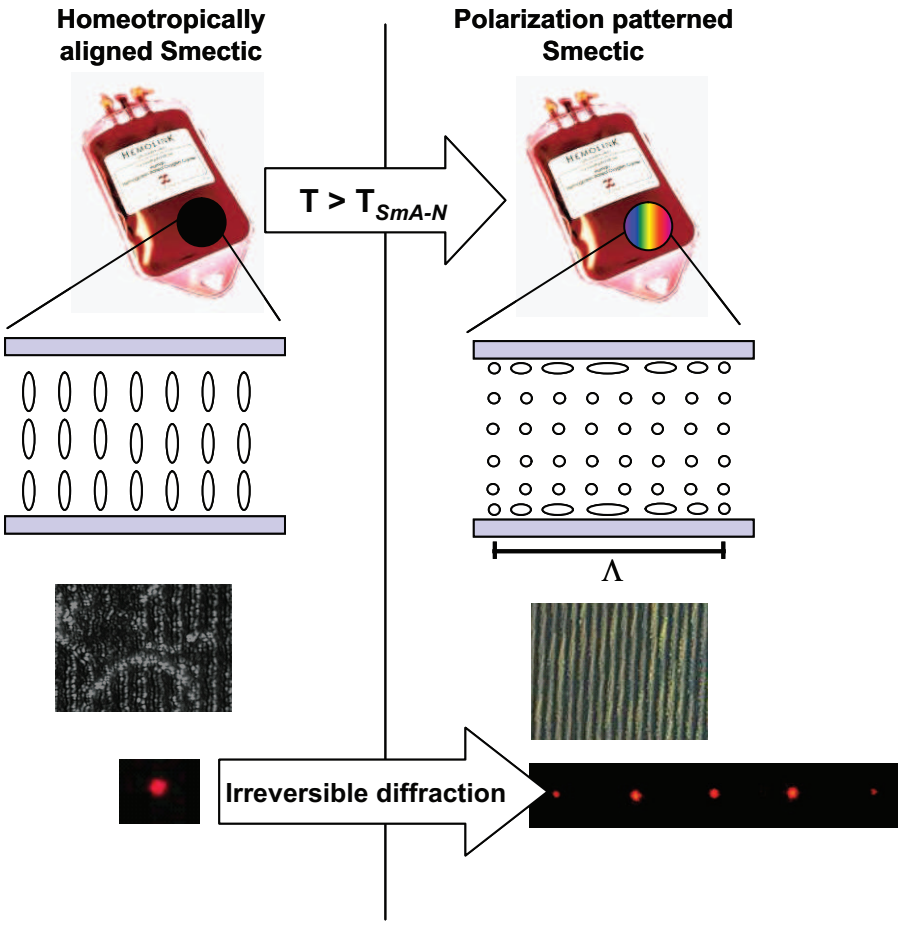

Figure 6.2: Application of an SmA liquid crystal polarization grating used as an irreversible thermometer to detect any extreme fluctuations in the temperature of blood bags during transportation.

6.4 Summary

A number of different applications have been introduced in this chapter, including those that relate to displays, photonics, and optical security. The polarization grating configurations demonstrated in Chapters 3 and 4 were the subject of an issued patent titled: *Method of alignment of liquid crystals comprising exposing an alignment material to an interference pattern* (US Patent 7196758).

Chapter 7

Summary

The overarching theme of this thesis focused on unique surface patterning features used to align liquid crystals (LCs) in novel ways. Substantial findings include a new approach to LC alignment, phase holography, which enables the creating of 1D and 2D diffraction gratings. A by-product of this unique approach to phase holography to align LCs is the finding that under certain circumstances, the competition between elastic and periodic surface forces results in a thresholdless nature in LC electro-optic switching.

In another set of experiments, holography was used to created gratings in LC-polymer composites. Rather than nematic LCs, fast switching FLCs were utilized. These materials were found to switch as low as 10 μs, several orders of magnitude lower than conventional nematics. A phenomenological model was created, based on the competition between two FLC domains with opposite facing dipoles, consistent with experimental observations. This work has been published in several peer reviewed publications, and the phase holography was the subject of a US patent.

Chapter 1 introduced the basic classifications of LCs, beginning with those that exhibit a LC phase through a range of concentrations in solvents, called lyotropics, and those that exhibit a LC phase through a stable temperature regime, called thermotropics. For the purpose of this thesis only calamitic (rod-like shaped) thermotropics were discussed. The phase sequence for a

calamitic thermotropic material possessing a crystal - nematic liquid crystal - isotropic phase was described in the context of orientational and positional ordering. The crystalline phase exhibited three dimensional orientational and positional ordering. The nematic LC (the least ordered LC phase) exhibited orientational ordering in only one dimension with an average orientational direction denoted by the nematic director (or unit vector) n. In contrast, the isotropic phase lacked both orientational and positional ordering. The presence or lack of orientational ordering was described quantitatively by an order parameter, S, taking into account the average angular deviation of the molecular axes for an ensemble of molecules to give perfect order ($S = 1$) for a crystal phase, and complete disorder ($S = 0$) for an isotropic phase. The order parameter for a nematic LC was temperature dependent and in the range of $S = 0.3 - 0.7$.

Chapter 1 also introduced higher ordered LC phases that possess a degree of one-dimensional positional ordering in addition to their orientational order, called smectics. These phases, which form lamellar structures, can be tilted (smectic-C) or non-tilted (smectic-A). The addition of a chiral carbon center or chiral dopant produces tilted chiral (smectic-C*) and non-tilted chiral (smectic-A*) phases, analogous to the smectic-C and smectic-A phases.

All LC molecules can be represented as having a shape anisotropy to give an aspect ratio for the molecular axes. Manifested in the shape anisotropy is the dielectric anisotropy, which, in the presence of an external field, will induce a dipole moment in the LC affecting its alignment in the direction of the field. Additionally, the optical anisotropy (or birefringence) dictates the speed at which light propagates though the LC.

The free energy of a LC system can also be expressed by taking into account the basic elastic deformations (splay, twist and bend) of a non-uniform director profile, as well as its field and surface interaction effects. LC alignment techniques were also introduced in Chapter 1, demonstrating conventional mono-domain alignment where the director aligns parallel to the surface normal (homeotropic) and in the plane of the surface (planar). Likewise, non-conventional alignment materials and methods to produce periodic, multi-domain configurations were presented, with an emphasis

on photo-reactive materials that can be used in conjunction with holographic exposure techniques to create periodic LC alignment.

Chapter 2 introduced light as an electromagnetic wave, where its propagation is well described by Maxwell's equations. Through these four equations, light and matter interactions – including refraction (Snell's law), incoherent scattering, and diffraction – can be described using mathematical relations. Additionally holography was introduced and differentiated from conventional photography in the sense that both the amplitude and phase of light are captured on a photosensitive film through the interference of an object beam and a reference beam. Upon illumination of the holographic film with a reconstruction (reference) beam, a three-dimensional virtual object can be imaged at the location of the original object.

Two different holographic recording modes were also discussed – reflection mode and transmission mode. In reflection mode, monochromatic, coherent beams illuminate the holographic film from opposite sides of the film to produce a sinusoidal amplitude modulation parallel to the surface of the film. The periodicity of the amplitude modulation (or grating pitch) is dictated by the Bragg equation. In transmission mode, beams interfere on the same side of the holographic film to produce a periodic amplitude modulation perpendicular to the surface. For the purpose of this thesis, only transmission mode holography was considered in greater detail.

In the case of an amplitude modulation, interfering beams have the same incident polarization, to create an intensity modulation while maintaining a constant polarization pattern. Additionally, holographic interference can induce a phase modulation (or modulation in polarization) while maintaining constant amplitude. Two separate methods to create a phase modulation were shown – the first used the interference of orthogonal linear (s- and p-polarizations) to create a periodic polarization pattern that spatially varied with linear, elliptical and circular polarization; the second used the interference of orthogonal circular (right- and left-handed) to create a periodic polarization pattern that spatially varied with rotating linear polarization. The relative thickness of the holographic recording film relative to the fringe spacing dictated whether the diffraction characteristics of the

gratings were in the Raman-Nath regime, Bragg regime or an intermediate regime between the two, as dictated by a dimensionless parameter.

Chapter 2 concluded with an introduction to holographic recording materials, including holographic polymer dispersed liquid crystals (H-PDLCs), azo dyes, and linear photopolymerizable polymers (LPPs). H-PDLCs are a homogenous mixture of non-reactive LC and photocurable polymer that, through amplitude interference, undergo a photo-induced phase separation and counter-diffusion to polymerize the monomer in the high intensity regions and force the LC to the low intensity regions of the interference pattern, thus creating a stratified grating of polymer rich and LC rich planes. Upon proper selection of LC and polymer, the holographic film can be index mismatched or matched upon application of an external electric field to create an electrically switchable diffraction grating. Azo dyes represented another class of holographic materials that undergo an isomerization process and realign perpendicular to the direction of incident polarization. Diffraction gratings using this class of materials in conjunction with LC have been demonstrated with the polarization modulation pattern created from incident orthogonal circular polarizations for periodic and continuous LC alignment. Chapter 2 concluded with LPP materials that undergo selective polymerization in the presence of polarized ultraviolet (UV) light. Subsequent to their exposure, these LPP materials align parallel to the direction of the incident polarization and result in a planar LC alignment parallel to the direction of the polymer chains (and polarization direction). The effects of LC gratings using this material with polarization holography were presented in Chapter 3.

Chapter 3 presented studies of LC alignment using LPP materials exposed to the interference pattern of orthogonal right- and left-handed circular polarized light. LC grating configurations were presented using registered planar-periodic boundary conditions by simultaneously exposing the top and bottom substrates to the polarization pattern. Electro-optic investigations were undertaken to experimentally determine the threshold voltages required to align the LC for different grating pitch sizes while maintaining a controlled film thickness. Experimental results showed that the threshold voltage decreased with reducing grating pitches. A model was presented, taking into

account the boundary conditions imposed by the LPP patterned surfaces, to predict the occurrence of a thresholdless transition when the grating pitch is comparable to the film thickness. This result is attributed to a non-uniform director profile propagating through the depth of the sample at zero voltage, thus increasing the elastic energy of the film. Because of this gain in elastic energy the model showed it was energetically favorable to have a zero voltage Freedericksz transition to minimize the free energy. This model was only valid for cases when the grating pitch was comparable to or larger than that the film thickness, since it was energetically prohibitive for the director to propagate periodically through the depth of the film when the thickness was greater than the grating pitch. Hybrid LC alignment configurations of periodic-planar – planar, and periodic-planar – homeotropic were also introduced in Chapter 3 and compared to the registered periodic-planar gratings in terms of alignment and electro-optic performance.

Chapter 4 investigated other photoalignment grating configurations for novel alignment configurations. A LC material exhibiting a smectic-A – nematic – isotropic phase sequence, was demonstrated in conjunction with the LPP polarization holographic exposure. The optical polarizing microscopy and diffraction studies verified the boundary conditions on the surface to enforce the periodic alignment structure imposed by the holographic exposure, while the interior of the cell resists the periodic bend profile due do a prohibitively large bend elastic constant in the smectic-A phase. This is in contrast to the nematic phase where the director profile on the surface propagates through the depth of the film in the same periodic manner.

Additionally, two-dimensional grating configurations were also presented. The first used separately exposed substrates and orthogonally rotated substrates to create two-dimensional LC alignment patterns with spatially varying planar and twist alignment that exhibited near-thresholdless switching. The second method of creating a two-dimensional alignment used the amplitude and polarization interference from four beams incident on the same side of the sample. Two structures were presented using this exposure technique – a two-dimensional periodic concentric LC alignment, and a two-dimensional periodic radial LC alignment, both of which show near thresholdless switching.

Chapter 5 presented an investigation of holographic polymer dispersed liquid crystals using ferroelectric liquid crystals. Using a 40:60 mixture of FLC and photo-curable monomer, exposed to the amplitude interference pattern, resulted in stratified regions of FLC rich planes and polymer planes formed perpendicular to the substrate surface. The polymer morphology resulting from this exposure process yielded a frustrated and unwound FLC director profile parallel to the polymer walls. The effect of FLC alignment was investigated as a function of grating pitch, where electro-optic studies of light transmission through the holographic grating showed that smaller grating pitch samples possess smaller deviations in the FLC domain orientation (i.e., more uniform planar alignment) than larger grating pitch samples due the confinement in the polymer channels. A model based on a phase grating of FLC and polymer was introduced to describe the first order diffraction characteristics for both incident s- and p-polarizations using experimental results from zero-order transmission data and the phase retardation values for the aligned FLC and polymer. The diffractive model accurately predicted the diffractive characteristics for smaller pitch samples. Taking into account the larger uncertainties of the FLC director deviations in the larger pitch sizes, the diffractive model remained within acceptable error bars of the experimental results. The electro-optic switching response for the holographic polymer dispersed ferroelectric liquid crystal gratings approached 10 μs at 15 V/μm, making these FLC-based H-PDLCs at least an order of magnitude faster than conventional nematic-based H-PDLCs.

Chapter 6 concluded with applications using the holographically patterned LPP surface alignment layers in displays, photonics, and optical security devices. One of the most promising applications for the LPP polarization gratings is its use as a diffractive optical element in portable projection displays. Through a materials optimization, these polarization gratings can demonstrate high diffraction efficiency for unpolarized light, or nearly 100% diffraction efficiency for circularly polarized light. Additionally, the LC gratings using the LPP alignment layers have been demonstrated as tunable lasing elements when pumped by a pulsed laser. The lasing line, which was emitted parallel to the grating vector, demonstrated a well-defined threshold, with an emission line of 4 nm that

could be tuned upon application of an external electric field. Finally, a number of optical security features were introduced as applications using the LPP polarization pattern in conjunction with a smectic-A phase LC material to create thermally bistable diffractive elements. In the initial alignment configuration, a diffraction pattern is not observed; however, if the sample was heated above the smectic-A – nematic transition temperature and cooled back to the initial temperature, a visible diffraction pattern could be observed. This type of 'irreversible thermometer' could be applied to blood bags to record any temperature fluctuations that occur during transportation. The second possible application for this configuration is optical security elements embedded in pharmaceutical packages to differentiate authenticate products from their potentially harmful counterfeits.

In conclusion, the general theme of this thesis combined soft matter materials and holography to investigate a number of LC alignment configurations not possible using other patterning techniques. The single-step holographic exposure process was demonstrated as an attractive method for creating surface and volume LC alignment effects continuous and periodic on the micrometer length scale. The underlying physics and electro-optics of the LC grating configurations presented in this thesis are rich in fundamental science and can easily be implemented in a number of display, photonics, and optical security devices.

Since the initial polarization holography surface patterning publication, many research groups have followed suit to further investigate LC, surface and field interactions that lead to improved electro-optic characteristics useful in device applications. This strongly suggests that the work demonstrated here, while not fully optimized for a particular application, is a substantial breakthrough in creating diffraction gratings that can be electrically erased at minimal field strengths, with major implications for future displays and photonic devices.

Appendix A

Surface Induced Orientation Order in Stretched PDLCs

A liquid crystal material in physical contact with a solid substrate is partially ordered even above the nematic-isotropic transition temperature. This phenomenon can be treated as orientational wetting of the substrate by the nematic phase at a temperature where the isotropic phase is stable in the bulk [79, 80]. On approaching the nematic-isotropic transition temperature (T_{NI}) from above, the thickness of the ordered nematic surface layer assumes either a finite or infinite limiting value, which corresponds to a partial or complete orientational wetting regime. To classify the wetting regime as either partial or complete, the absorption parameter is used $\Gamma = \int_0^\infty S(z)dz$, where z is the distance from the ordering inducing surface and $S(z)$ is the scalar orientational order parameter [30]. Neglecting the possibility of biaxiality, the surface-induced ordering in the isotropic phase is well described by $S(z)$ and the preferred molecular direction $\mathbf{n}(\mathbf{r})$ in the surface layer. If Γ diverges as T_{NI} is approached, the orientational wetting is known as complete; if Γ remains finite, orientational wetting is said to be partial. The nature of the wetting regime is strongly correlated to the interaction strength between the liquid crystal and the orienting solid surface, and therefore depends on the

magnitude of the surface induced order parameter in the interfacial layer [81]. If the value of the surface order parameter S_0 exceeds a threshold order parameter S_c, then wetting is complete; below S_c, the wetting is only partial. Within the Landau-de Gennes framework, the threshold value is equal to the bulk nematic order parameter at T_{NI} [79, 80].

The pioneering work of Miyano demonstrated the surface-induced order parameter could be accessed with pretransitional birefringent measurements [82]. Further experimental efforts include second harmonic generation, field induced twist [83], and evanescent wave ellipsometry [84]. Crawford and coworkers found that liquid crystals confined to Nuclepore cavities could be effectively probed with deuterium nuclear magnetic resonance (^{2}H-NMR) [85]. Since the surface-to-volume ratio in these confining systems was large, and the orientation of the liquid crystals in the Nuclepore cavities was uniform with respect to the static magnetic NMR field, a small but measurable quadrupole splitting was measured above T_{NI}. In fact, it was measurable to temperatures deep in the isotropic phase ($T - T_{NI} \sim 20$ K). This early study proved the validity of the ^{2}H-NMR technique in surface-induced order studies, and showed that ^{2}H-NMR was capable of measuring S_0, the interfacial layer thickness l_0, and the exchange rate between ordered molecules on the surface and in the bulk. The ^{2}H-NMR technique was later used to study liquid crystals confined to alumina channels of Anopore membranes where anchoring transitions were observed and radically different values of S_0 were measured depending on the surface alignment layer [30, 81, 86]. The work has recently been extended to smectic liquid crystals, where NMR can measure the degree of smectic-nematic coupling [87] and pretransitional smectic layering phenomena [88]. In fact, the NMR technique has been applied to numerous confined liquid crystal systems, including Vycor glass [89–91], silica aerogel [92], and Millipore filters [93]. Most recently, NMR has been used to probe the layer order of mesogenic molecules deposited on the cavity walls of Anopore membrane surfaces [94].

In contrast to the intensive efforts devoted to liquid crystals confined to cylindrical and random geometries [95], the surface parameters of polymer dispersed liquid crystals (PDLC) have been scarcely investigated. Golemme and coworkers used ^{2}H-NMR to study spherical liquid crystal

droplets [96]. In their pioneering publication on NMR to study PDLCs, they revealed that the weak first order nematic-isotropic transition was replaced by a continuous evolution of order for sufficiently small droplets, a prediction made many years before by Sheng in planar samples [79] and later by Vilfan and coworkers in spherical droplets [97]. Studies of PDLC droplets have continued on since the seminal publication of Golemme. NMR relaxometry was used to extract the value of S_0 from the transverse relaxation rate T_2^{-1} [98]. The ability to measure S_0 directly from the ^{2}H-NMR quadrupole splitting frequency in PDLC systems remains a challenge for two reasons: (1) the droplet director (the average orientation of the symmetry axis of the liquid crystal droplet) differs from droplet to droplet with respect to the magnetic field direction; and (2) there tends to be a much larger size distribution in PDLCs compared to the well-defined pores of Nuclepore and Anopore membranes [30, 81, 86].

On the other hand, with the continuous increase of computing power, as well as with the development of simulation techniques, strongly confined liquid-crystalline systems are becoming increasingly accessible to computer simulation studies. In particular, great effort has been invested into the exploration of nematic ordering inside PDLC droplets; most analyses were based on a simple and computationally cheap Lebwohl-Lasher lattice model. Typically, Monte Carlo (MC) simulations were carried out for these model systems [99]. The resulting numerical output is then expressed in terms of suitable order parameters or, even more conveniently, directly in terms of macroscopic experimental observables such as ^{2}H-NMR spectra. The methodology for calculating dynamic NMR spectra, capable of handling fluctuations of molecular long axes and translational diffusion, has been presented and tested for spherical PDLC droplets [100, 101]. More recent MC studies of nematic ordering have been extended to elliptical droplets as well [102, 103].

Here we discuss a PDLC system yielding a reasonable quadrupole splitting in the isotropic phase. After PDLC formation using an emulsification technique [104], the PDLC film is subjected to high degree of uniaxial strain (as much as 400%) to create ellipsoidal droplets whose droplet director and cross-section are nearly uniform [105]. These highly aligned droplet samples, currently being

developed for light scattering polarizer applications [106], create an ideal system to be studied with ^{2}H-NMR. We present an experimental determination of the surface-induced order parameter S_0 directly obtained from the quadrupole splitting frequency measured above T_{NI}. The experimental work is complemented with quadrupole splitting data derived from Monte Carlo simulations.

A.1 Sample Preparation And Experimental Method

PDLC films used in this study consisted of dispersions of deuterated 4′-pentyl-4-cyanobiphenyl (5CB-αd_2) and polyvinyl alcohol PVA205 (molecular weight: 25000, degree of hydrolysis: 88%, *Kuraray Co., Ltd.*), which is a water-soluble polymer. A 20 wt.% aqueous solution of PVA was mixed with the liquid crystal and then dispersed in water [107]. An ultrasonic processor (CPX-400, 400 W, 20 kHz, *Cole-Parmer Instrument Co.*) at 40% output with 1/8" microtip emulsified the liquid crystal into the PVA aqueous solution. The emulsion was then coated on a smooth polyethylene terephthalate (PET) substrate using a Meyer Bar and processed under ambient conditions. After the evaporation of the water, the polymer film was carefully released (peeled) from the substrate. The film thickness was approximately 16 ± 4 μm and the concentration of liquid crystal in the film was 25 wt.%. The films were stretched to the desired strains (5%, 20%, 100% and 400%), cut into strips 20 mm $\times$ 6 mm in size, stacked such that their thicknesses were more than 50 μm, and carefully inserted into a NMR tube.

Figure A.1(a) shows a scanning electron microscope (SEM) image of a PDLC film before stretching. The director within the droplet aligns parallel to the stretch direction (the major axis of the ellipse) [108]. This has been proven using optical polarization measurements [103, 105, 106]. The average diameter in Figure A.1 was measured to 92 ± 16 nm (radius $R_0 = 46 \pm 8$ nm). Assuming the liquid crystal droplet was incompressible and its shape is spherical, the radius R after stretching is approximated by

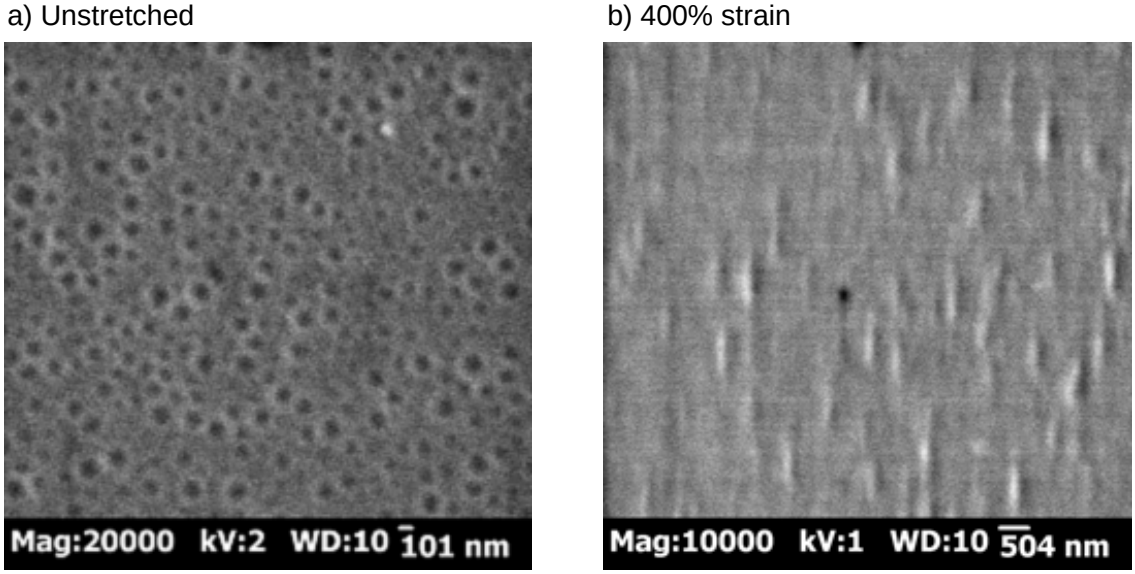

Figure A.1: SEM photographs of PDLC films: (a) before stretching, and (b) after 400% strain. The average initial diameter of the droplets is 92 ± 16 nm ($R_0 = 46 \pm 8$ nm).

$$R \sim R_0(1+\epsilon)^{-1/2}, \tag{A.1}$$

where R_0 is the initial radius and ϵ is the strain. In fact, the shape of the droplets is not perfectly spherical but an oblate spheroid with the minor axis perpendicular to the film plane [104]. Then, assuming the isotropic Poisson's ratio [109], Eq. (A.1) is still valid when we define R_0 as an initial length of one of the principal axes. Fig A.1(b) shows the droplets after they have been subjected to 400% strain.

The stretched PDLC films were stacked in the NMR tube such that the stretched axis of the film was parallel to the magnetic field. The NMR experiments were performed on a solid-state spectrometer (AVANCE$^{\text{TM}}$ 300/ Ultrashield$^{\text{TM}}$, 300 MHz, 89 mm, *Bruker BioSpin GmbH*) with a 7.05 T magnetic field. A modified quadrupolar echo sequence $(\pi/2)_x$-τ-$(\pi/2)_y$ was employed where $\tau = 100$ ms and the length of the $\pi/2$ pulse was 10 ms. The free-induction-decay (FID) was averaged

more than 10000 times to achieve a reasonable signal-to-noise ratio. The temperature in the sample probe was controlled to within ±0.1 °C.

A.2 NMR Technique

Deuterium nuclei have been used frequently as a NMR probe in studies of molecular structure and dynamics in liquid crystals. ^{2}H-NMR provides the orientational order at the molecular level via time-averaged quadrupole splitting frequency from selectively deuterated liquid crystal molecules. In the absence of motional averaging, a deuterated molecule at position $\mathbf{r}$ within a droplet will yield a spectrum of two sharp lines separated by

$$\delta\nu(\mathbf{r}) = \frac{\delta\nu_B}{S_B} S(\mathbf{r}) \left[\frac{3}{2}\cos^2\theta_B(\mathbf{r}) - \frac{1}{2}\right], \tag{A.2}$$

where $\theta_B(\mathbf{r})$ is the angle between the local nematic director and the magnetic field; $S(\mathbf{r})$ is the local order parameter; and $\delta\nu_B/S_B$ is the ratio between the quadrupole splitting frequency and the order parameter of the bulk nematic. $\delta\nu_B/S_B$ for 5CB in the nematic phase is 87.5 kHz [86].

This work focuses on uniaxially stretched PDLCs using 5CB-αd_2. The magnetic coherence length, $\xi_m = B^{-1}\sqrt{\mu_0 K/\Delta\chi}$, is $\xi_m \sim 1.1$ μm [110] for reported values of $\Delta\chi = 1.2\times10^{-7}$, the anisotropy of the diamagnetic susceptibility, $K = 6\times10^{-12}$ N, the elastic constant, and $\mu_0 = 4\pi\times10^{-7}$ N/A^2 (the permeability of free space). ξ_m is significantly larger ($\xi_m \gg R$) than the droplet radii so that the field has no appreciable aligning effect. The characteristic length of diffusion in an NMR measurement is $d \sim \sqrt{D/\delta\nu_B}$. With $D \sim 10^{-10}$ m^2/s and $\delta\nu_B = 45$ kHz in the nematic phase, $d \sim 50$ nm. In the isotropic phase, $\delta\nu \sim 500$ Hz giving $d \sim 450$ nm. Finally, $d \gg R$ in the isotropic phase, therefore a complete diffusional averaging is expected.

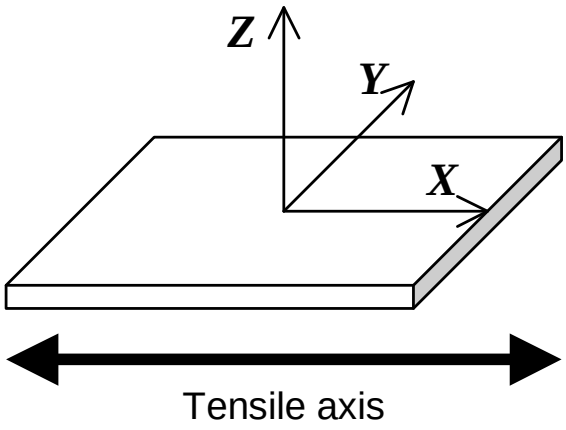

Figure A.2: The schematic diagram of the coordinate system for the NMR measurement.

A.3 Liquid Crystal Alignment In Nematic Phase

According to optical polarization measurements, liquid crystal molecules confined within stretched PDLC droplets on average align parallel to the stretch direction [103, 105, 106]. This alignment is observed by a change in birefringence of the droplets, and is not directly measured. In order to directly investigate the liquid crystal alignment, we observed the NMR spectra of stretched PDLC films in nematic phase. Figure A.2 illustrates the coordinate system of the NMR samples. By orienting the sample in the NMR magnetic field parallel to X, Y and Z, we can independently measure the liquid crystal director distribution with respect to these three axes. The NMR spectra were first measured in the nematic phase at 298 K (room temperature).

Figure A.3 shows the NMR spectra of 5CB-αd_2 in an unstretched PDLC film (Figure A.3(a) and (b)) and the bulk (Figure A.3(c)), as well as a schematic depiction of liquid crystalline alignment within droplets. Both NMR measurements where the magnetic field is in X and Y directions (Figure A.2) are equivalent under geometrical considerations. From Eq. (A.2), the quadrupole splitting frequency at $\theta_B = 90^\circ$ is one-half that of the bulk aligned splitting. The quadrupole splitting frequency in the unstretched PDLC, in the case where the magnetic field is along Z-axis

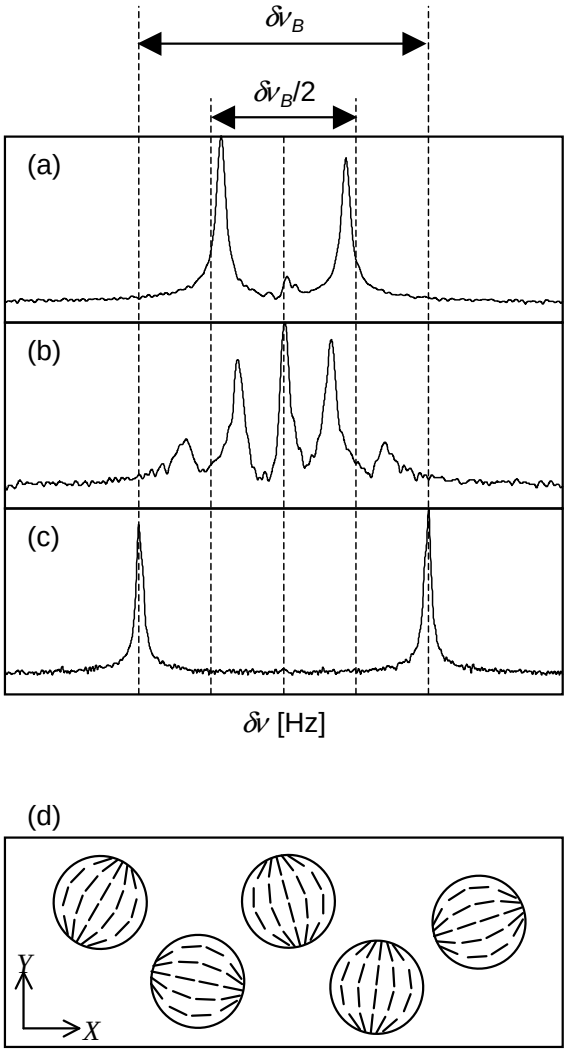

Figure A.3: The NMR spectra of 5CB-αd_2 in an unstretched PDLC film and the bulk: (a) magnetic field along Z-axis, (b) magnetic field along Y-axis, (c) bulk. (d) Schematic depiction of droplet organization: bipolar axes not aligned.

(Figure A.3(a)), is nearly one-half that of the bulk (Figure A.3(c)), which indicates the liquid crystal molecules align predomnantly perpendicular to the Z-axis in this composite. Moreover, Figure A.3(b) is similar to the NMR spectrum of a Pake-type powder spectrum, which is obtained from a two-dimensionally random distribution of liquid crystal molecules [86]. These results indicate the ordering in the droplets is bipolar and the bipolar symmetry axes are randomly oriented in the XY plane. This is in agreement with the fact that the PDLC film collapses along the Z-axis during the evaporating process, and then the shape of droplets becomes an oblate spheroid with the minor axis perpendicular to the film plane [104]. Such a film is schematically represented in Figure A.3(d). The reason why the quadrupole line-splitting frequency is slightly smaller than the expected bulk values is attributed to the curvature of the director field in the droplet [96].

Figure A.4 shows the NMR spectra of a 100% stretched PDLC film (Figure A.4(a), (b) and (c)) and the resulting liquid crystal alignment (Figure A.4(d)). The quadrupole splitting frequencies in the case where the magnetic field is directed along the Y and Z-axes are one-half that of the bulk (Figure A.4(a), (b)), and the quadrupole splitting frequency in the case where the magnetic field is directed along the X-axis is the same as that of the bulk. Consequently, liquid crystal molecules in these PDLCs are mostly aligned along the X-axis. We have also investigated 5%, 20% and 400% stretched PDLC films and compared them to the aligned bulk sample, as shown in Figure A.5. It was found that the liquid crystal molecules are aligned in all of the samples, even for the 5% sample. These highly aligned systems enable us to extend our NMR study to the isotropic phase, as the samples can be aligned such that their directors are parallel to the magnetic field, providing a maximum splitting.

A.4 Surface-Induced Order In Isotropic Phase

Thus far, we have confirmed the molecular alignment inside droplets in the nematic phase. This was essential to obtain reliable information on the effective aligning tendency of the polymer matrix,

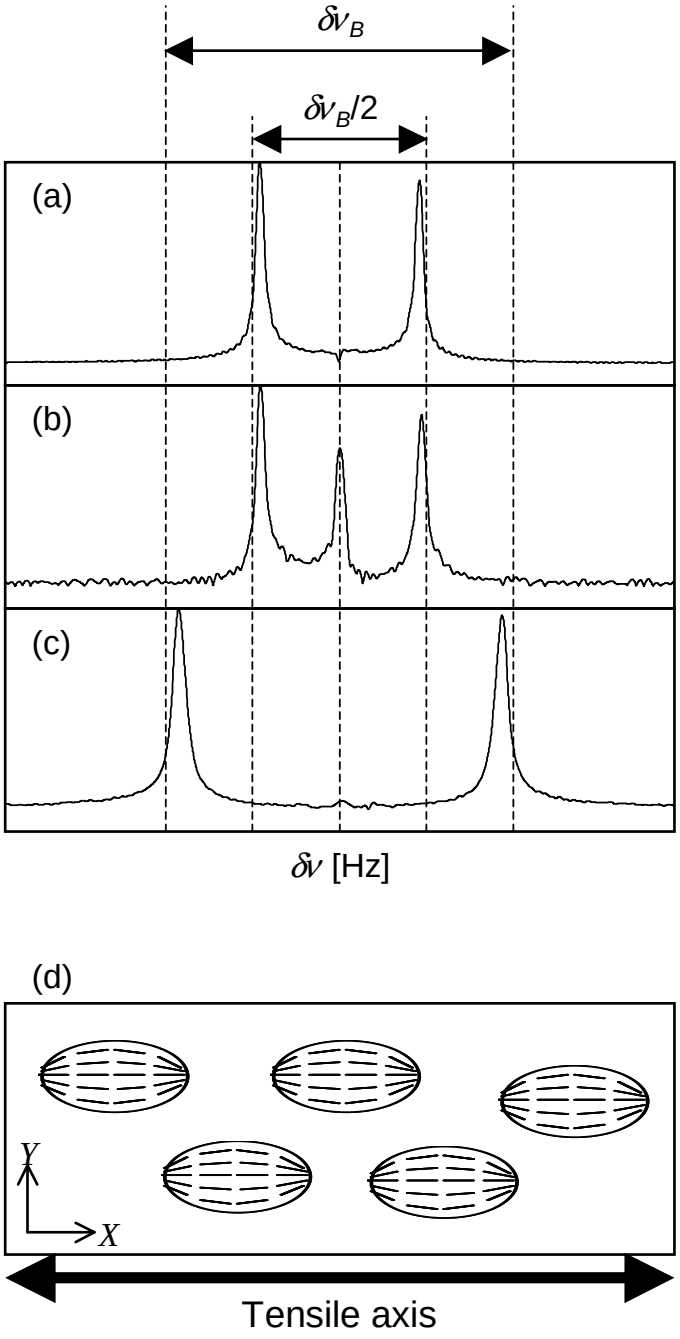

Figure A.4: The NMR spectra of 5CB-αd_2 in a 100% stretched PDLC film: (a) magnetic field along the Z-axis, (b) magnetic field along the Y-axis, (c) magnetic field along the X-axis. (d) Schematic depiction of droplet organization: bipolar axes aligned.

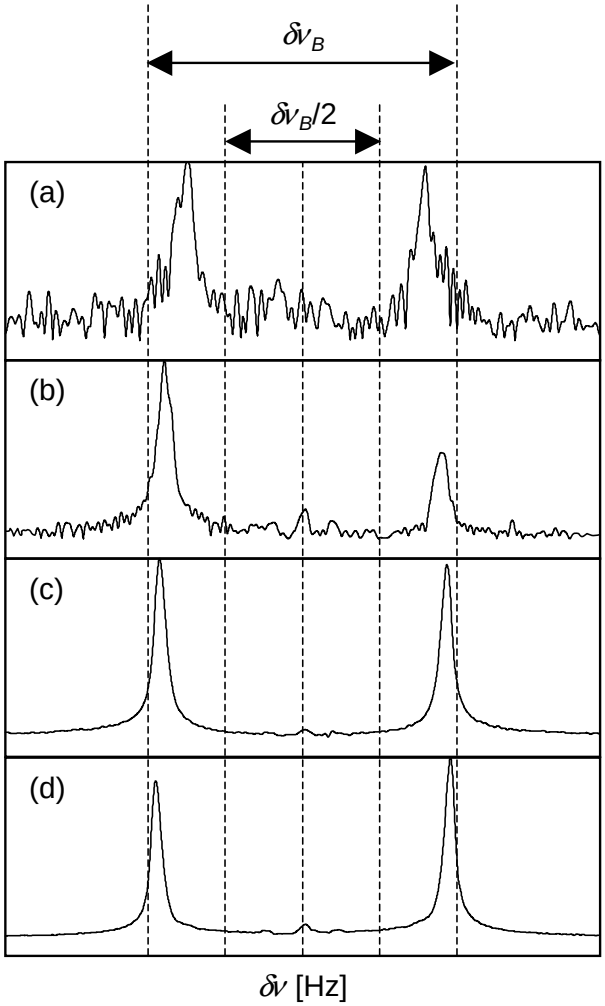

Figure A.5: The NMR spectra of 5CB-αd_2 in (a) 5%, (b) 20% and (c) 400% stretched PDLC films. Applied magnetic field is along the X-axis.

shown to be of great importance in stretched PDLC systems [103, 106]. In this section, we study stretched PDLC films in the isotropic phase and show how to detect changes in the local aligning power of the confining matrix determine the degree of surface-induced order. The same approach has already been successfully applied to nematics in cylindrical confinement [86] and will be here adapted to the elliptical geometry that characterizes our PDLC systems. Note that both versions of the approach share the underlying basic physical phenomena.

We consider a one-dimensional case where the x-axis represents the normal of a confining wall located at $x = 0$. In the isotropic phase the degree of nematic order decays when moving away from the wall. This can be formally described by the Landau-de Gennes formalism for the nematic-isotropic transition giving a phenomenological expression for the free energy density f [3, 111]. In such a case f can be expanded in terms of a single order parameter, $S(x)$, and is expressed as

$$f = f_0 + f_1[S(x)] + \frac{L}{2}[\nabla S(x)]^2 + g[S(x) - S_s]^2\delta(x), \tag{A.3}$$

where S_s is the surface-imposed degree of order, and $g > 0$ and $L > 0$ are phenomenological constants. Moreover, f_0 is the S-independent part of the free energy density and $f_1[S(x)]$ is given by

$$f_1[S(x)] = \frac{a}{2}(T - T^*)S^2(x) - \frac{B}{3}S^3(x) + \frac{C}{4}S^4(x). \tag{A.4}$$

Here T denotes temperature, T^* the limit of supercooling, while $a > 0$, $B > 0$, and $C > 0$ are phenomenological constants. The final term in Eq. (A.3) is the surface contribution where g reflects the magnitude of the liquid crystal-solid substrate interaction [**?**]. The total free energy over the volume of the cavity is obtained by integrating Eq. (A.3) over volume

$$F = \int_{vol} \left(f_0 + f_1[S(x)] + \frac{L}{2}[\nabla S(x)]^2 \right) dV + \frac{1}{2}gA(S_0 - S_s)^2, \tag{A.5}$$

where S_0 is the actual order parameter at the surface and A is the surface area.

Assuming the degree of surface-induced order in the isotropic phase to be low, in Eq. (A.4) higher-order terms $S^3(x)$ and $S^4(x)$ can be neglected. Minimizing the total free energy, the order parameter as a function of x exhibits an exponential decay

$$S(x) = S_0 e^{-x/\xi}, \tag{A.6}$$

with ξ standing for the correlation length associated with nematic ordering. It is given by

$$\xi = \xi_0 \sqrt{\frac{T^*}{T - T^*}}, \tag{A.7}$$

where $\xi_0 \sim 6.5$ Å [112] and ξ diverges at T^* [3]. For 5CB, $T_{NI} - T^* = 2B^2/9aC \sim 1.1$ K.

The actual degree of nematic order at the surface, S_0, can in principle exhibit a temperature dependence. Calculating the total free energy in a semi-infinite sample and minimizing it with respect to S_0 gives

$$S_0 = \frac{S_s}{1 + \sqrt{a(T - T^*)L}/2g}. \tag{A.8}$$

For $2g \gg \sqrt{a(T - T^*)L}$ (e.g., close to the nematic-isotropic transition) S_0 approaches S_s and is essentially temperature-independent. If, on the contrary, $2g \ll \sqrt{a(T - T^*)L}$, one has [86]

$$S_0 \approx \frac{S_{00}}{2\sqrt{T/T^* - 1}}, \tag{A.9}$$

where $S_{00} = 4gS_s/\sqrt{aT^*L}$ has been introduced. The two limits will be referred to as a "temperature-independent model" and a 'temperature-dependent model.'

However, the above equations based on a continuum description sometimes do not adequately describe the experimental results. An improved interfacial surface-layer model has been proposed

and implemented in many systems [86]. The profile of the surface-induced nematic order is modified as

$$S(x) = \begin{cases} S_0, & 0 \leq x \leq l_0 \\ S_0 e^{-(x-l_0)/\xi}, & r > l_0 \end{cases} \tag{A.10}$$

where l_0 is the interfacial thickness of the surface layer, which is approximately on the order of molecular dimensions and is characterized by a constant degree of nematic order.

A.4.1 Ellipsoidal droplet

The stretched PDLC droplets can be represented as ellipsoids, as suggested by the SEM image (Figure A.1(b)). Figure A.6 introduces a suitable coordinate system: the z-axis is taken along the long axis of the droplet (which coincides with the bipolar axis of the nematic alignment) and r is the distance from the z-axis. Here we discuss the case in which the NMR magnetic field is directed along z. The droplet center is chosen at $z = 0$.

Splitting the ellipsoid into slices along z and following the approach used for cylindrical cavities presented in Ref. [86], one can adapt the results given in Eq. (A.10) and approximately describe S as in the ellipsoidal cavity

$$S(r,z) = \begin{cases} S_0, & R(z) \geq r \geq R(z) - l(z) \\ S_0 e^{-[(R(z)-l(z))-r]/\xi}, & R(z) - l(z) \geq r \geq 0. \end{cases} \tag{A.11}$$

Here $R(z)$ and $l(z)$, the radius and the interfacial thickness resulting along the r direction within a slice centered at z, are expressed as

$$R(z) = R_0\sqrt{1 - z^2/Z_0^2} \tag{A.12}$$

$$l(z) = \frac{l_0}{\cos\theta_B} \tag{A.13}$$

where R_0 and Z_0 are the length of the short axis and long axes, respectively. Figure A.7 shows

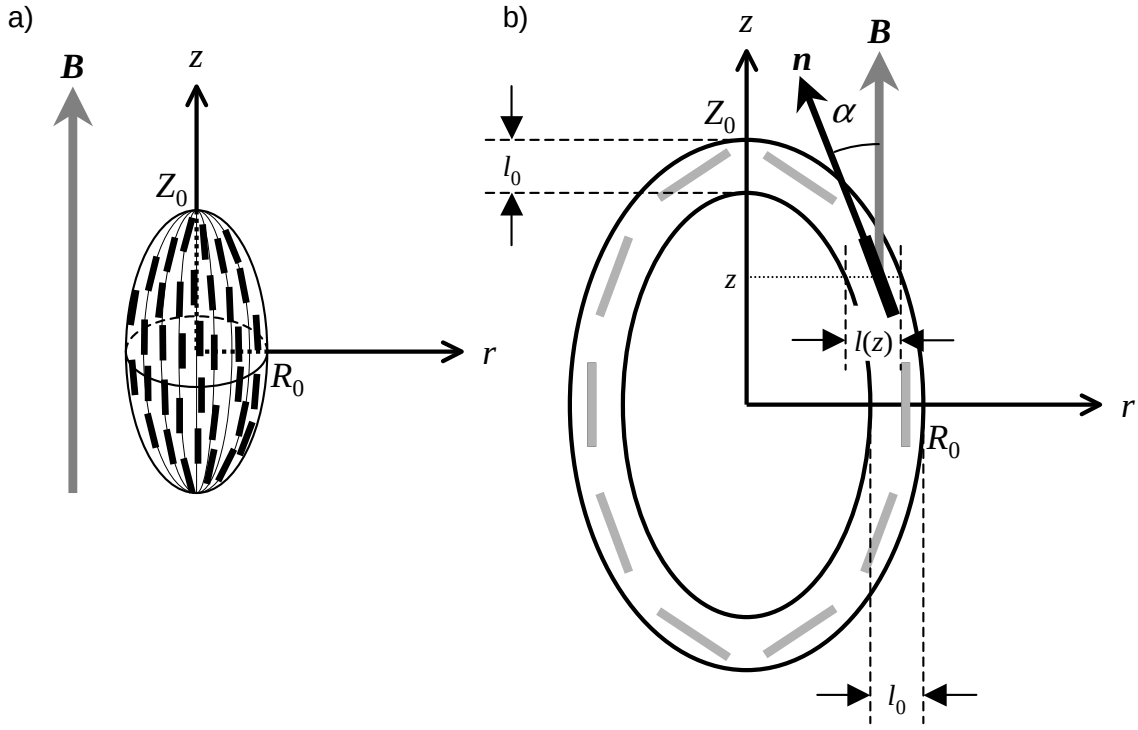

Figure A.6: Schematic diagram of an elliptical geometry: (a) Cylindrical coordinate system for elliptical geometry, and (b) surface molecule alignment with respect to the elliptical surface and the applied magnetic field.

$S(r,z)/S_0$ as a function of r/R_0 at different z: the ellipse is composed of cylindrical slices with diameters $R(z)$.

The $S(r,z)$ order parameter profile can now be used to predict the quadrupole splitting in the ^{2}H-NMR spectra. For tangential anchoring in ellipsoids with their major axis aligned parallel to the magnetic field, the director will change its relative direction to the magnetic field parametrized by the angle θ_B, as shown in Figure A.6. Assuming complete diffusional averaging, the quadrupole splitting will be a spatial average of (A.2), i.e.,

$$\begin{aligned} \langle \delta\nu \rangle &= \frac{\int_0^Z \int_0^{R(z)} r dr dz S(r,z) \left[\frac{3}{2}\cos^2\theta_B - \frac{1}{2}\right]}{\int_0^Z \int_0^{R(z)} r dr dz} \\ &= \frac{3\pi S_0 \xi}{8R} E_\xi(\rho) + \frac{3 S_0 l_0}{4R} E_l(\rho), \end{aligned} \tag{A.14}$$

introducing

$$\begin{cases} E_\xi(\rho) &= \dfrac{2\rho^2 + 4\rho - 1}{(\rho+1)^2}, \\ E_l(\rho) &= \dfrac{2\rho^2+1}{\rho(\rho^2-1)} + \dfrac{\rho(2\rho^2-5)}{(\rho^2-1)^{3/2}} \arcsin(\sqrt{1-\rho^{-2}}), \end{cases} \tag{A.15}$$

where ρ is the aspect ratio of the ellipse described by $\rho = Z/R$. At $\rho = 1$, where the sample is unstretched, $E_\xi(\rho)$ and $E_l(\rho)$ are equal to 5/4 and 2, respectively. As ρ increases, $E_\xi(\rho)$ and $E_l(\rho)$ increase monotonically and converge to 2 and π, respectively. Therefore, at large ρ, Eq. (A.14) reduces to

$$\langle \delta\nu \rangle = \frac{3\pi S_0 \xi}{4R} + \frac{3\pi S_0 l_0}{4R}. \tag{A.16}$$

ρ can be determined experimentally, or is deduced by using Eq. (**??**), to be

$$\rho = \frac{R_0(1+\epsilon)}{R_0(1+\epsilon)^{-1/2}} = (1+\epsilon)^{3/2}. \tag{A.17}$$

Finally, by combining Eqs. (A.2), (A.8) and (A.14), we obtain the two limiting expressions:

$$\langle \delta\nu \rangle = \frac{\delta\nu_B}{S_B}\left[\frac{A}{T-T^*} + \frac{B}{(T-T^*)^{1/2}}\right], \tag{A.18}$$

$$\langle \delta\nu \rangle = \frac{\delta\nu_B}{S_B}\left[\frac{A'}{(T-T^*)^{1/2}} + B'\right] \tag{A.19}$$

Eq. (A.18) is the limit for a temperature-dependent S_0 where

$$\begin{cases} A &= 3\pi\xi_0 S_{00} T^* E_\xi(\rho)/8R, \\ B &= 3 l_0 S_{00}\sqrt{T^*} E_l(\rho)/4R. \end{cases} \tag{A.20}$$

Eq. (A.19), on the other hand, is the limit for a temperature-independent S_0, which is obtained for large g, where

$$\begin{cases} A' &= 3\pi\xi_0 S_0\sqrt{T^*} E_\xi(\rho)/8R, \\ B' &= 3 l_0 S_0 E_l(\rho)/4R. \end{cases} \tag{A.21}$$

Especially at large extensions ρ, Eqs. (A.20) and (A.21) become

$$\begin{cases} A &= 3\pi\xi_0 S_{00} T^*/4R, \\ B &= 3\pi l_0 S_{00}\sqrt{T^*}/4R, \end{cases} \tag{A.22}$$

$$\begin{cases} A' &= 3\pi\xi_0 S_0\sqrt{T^*}/4R, \\ B' &= 3\pi l_0 S_0/4R. \end{cases} \tag{A.23}$$

These equations are independent of ρ and are identical to the results in the case where the liquid crystal molecules on the surface align parallel to the tensile axis. By fitting the experimental data of $\langle \delta\nu \rangle$ using Eq. (A.18), we can estimate A and B, then we can back-out the surface order parameter S_{00} and the interfacial thickness l_0 in an elliptical cavity using Eq. (A.20). Similarly, using Eq. (A.19) and (A.21), we can estimate the surface order parameter S_0 and the interfacial thickness l_0 in an elliptical cavity in the temperature-independent model.

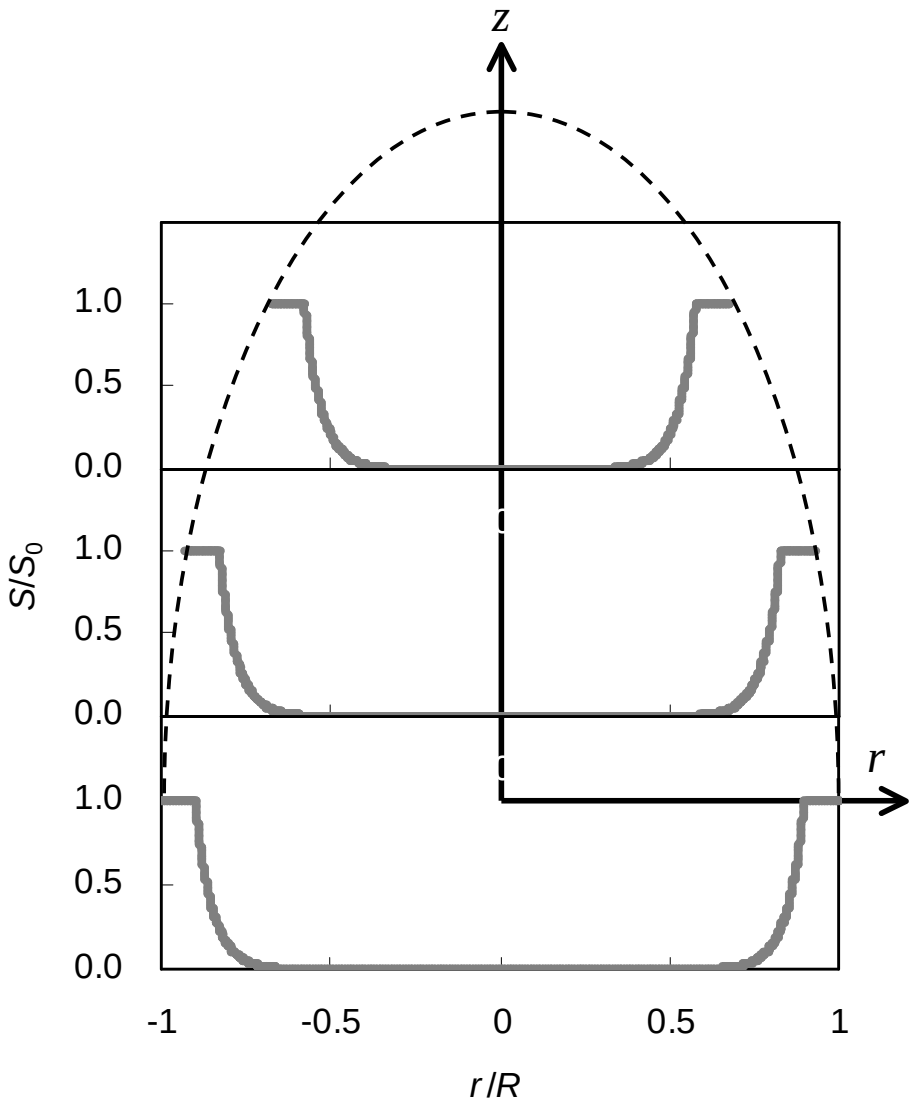

Figure A.7: The molecular orientational order parameter profile in an elliptical cavity at different z. Dashed line illustrates the surface of the elliptical cavity.

A.4.2 Surface-Induced Orientational Order of Stretched PDLCs in Isotropic Phase

We will now check which of the above limits (temperature-dependent or constant S_0) is suitable for our analysis. Figure A.8 shows the NMR spectra of 100% and 400% stretched PDLC films in the isotropic phase as a function of temperature. The quadrupolar line-splitting decreases as temperature increases in all samples; additionally, the quadrupole line-splitting increases as strain increases. From Eq. (A.17), ρ for a 400% stretched sample is $\sim$ 11 and large enough to apply to Eqs. (A.22) and (A.23). Figure A.9 shows the temperature dependence of S_{00} calculated from Eqs. (A.18) and (A.22), as well as S_0 calculated from Eqs. (A.19) and (A.23) where $\xi_0 = 6.5$ Å, $T_{NI} - T^* = 1.1$ K and $l_0 = 10$ Å to roughly estimate the temperature dependence of S_{00} and S_0 [86]. According to the assumption, both S_{00} and S_0 should be constant, but S_{00} increases with temperature. Since this result indicates that the temperature-dependent model is not valid for the stretched PDLC, we employed the temperature-independent model to analyze the surface order parameter in our particular system.

Figure A.10 shows the temperature dependence of the quadrupole splitting frequency for 5CB-αd_2 in 5%, 20%, 100% and 400% stretched PDLC films. The solid line in Figure A.10 is the best fit result for Eq. (A.19), and the values of S_0 and l_0 calculated from the best fit are shown as well. ρ is obtained from Eq. (A.17) and $E_\xi(\rho)$ and $E_l(\rho)$ are calculated from Eq. (A.15). R is estimated from Eq. (**??**) with $R_0 = 46$ nm, based on our SEM observation. ξ_0 is assumed to be 6.5 Å. The values of $S_0 = 0.007 - 0.024$ are smaller than the reported value of $S_0 = 0.021$ for 5CB in Anopore membranes with untreated surface, and the value of $l_0 = 0.0 - 11.3$ Å are also smaller than the reported value of $l_0 = 10.4 - 19.3$ Å for 5CB in Anopore membranes with various surface treatments [86]. Figure A.11 shows the strain dependence of S_0. S_0 increases quickly from 0% to 50% strain and then saturates during stretching. This behavior suggests the alignment of the liquid crystal molecules within droplets confined in the PVA polymer matrix is influenced by the

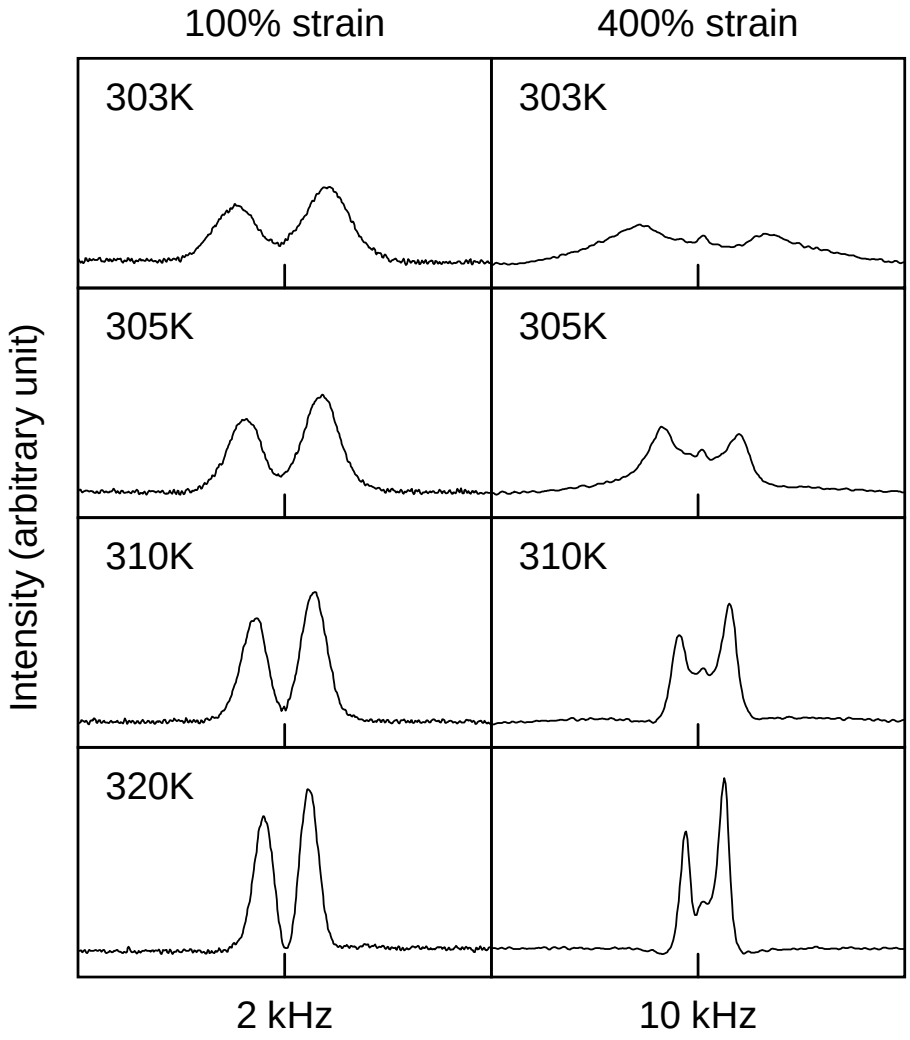

Figure A.8: ^{2}H-NMR spectra for 5CB-αd_2 of 100% and 400% stretched PDLC films in the isotropic phase. The magnetic field is parallel to the tensile axis (X-axis).

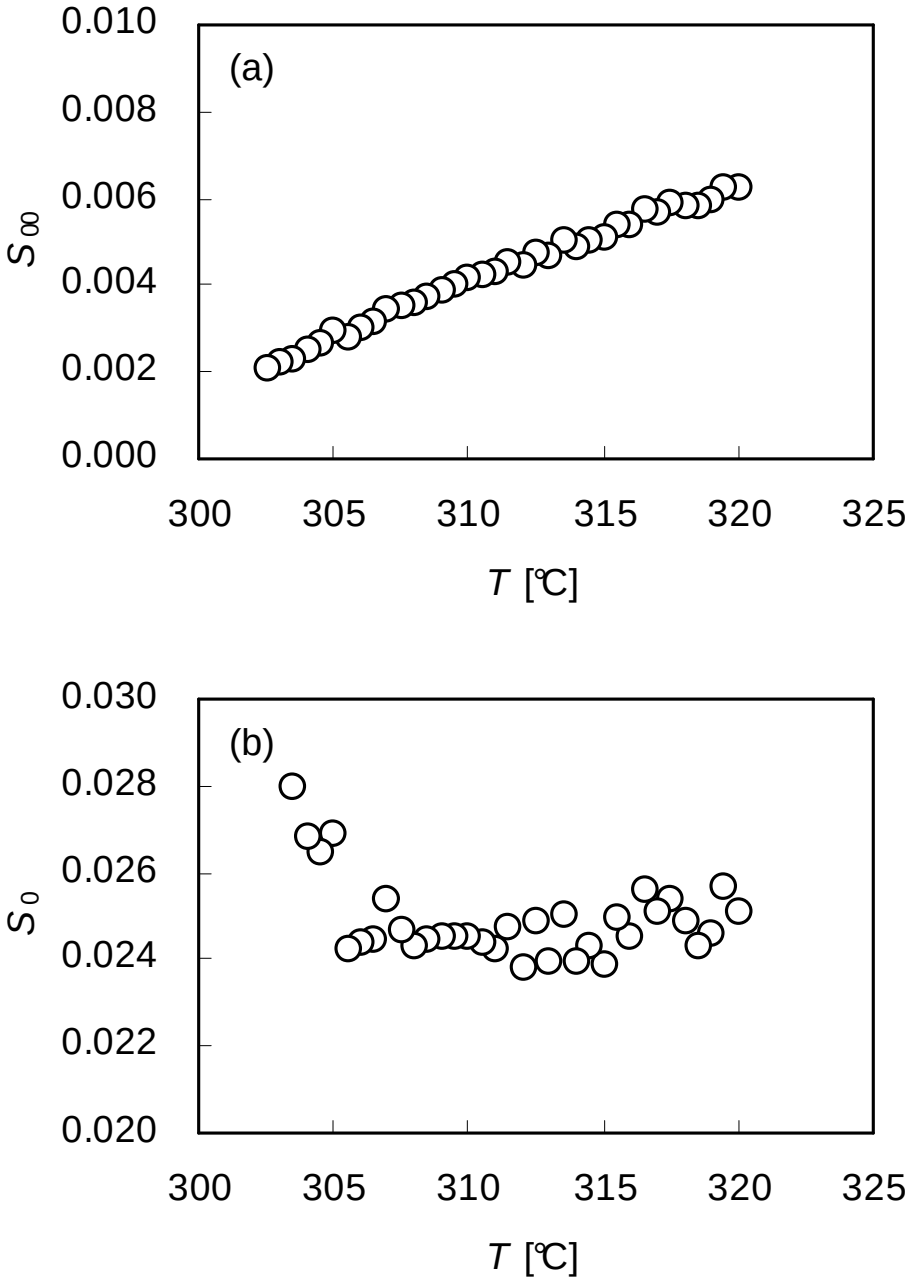

Figure A.9: (a) Temperature dependence of S_{00} calculated from Eqs. (A.18) and (A.22), and (b) S_0 calculated from Eqs. (A.19) and (A.23) with $\xi_0 = 6.5$ Å, $T_{NI} - T^* = 1.1$ K and $l_0 = 10$ Å.

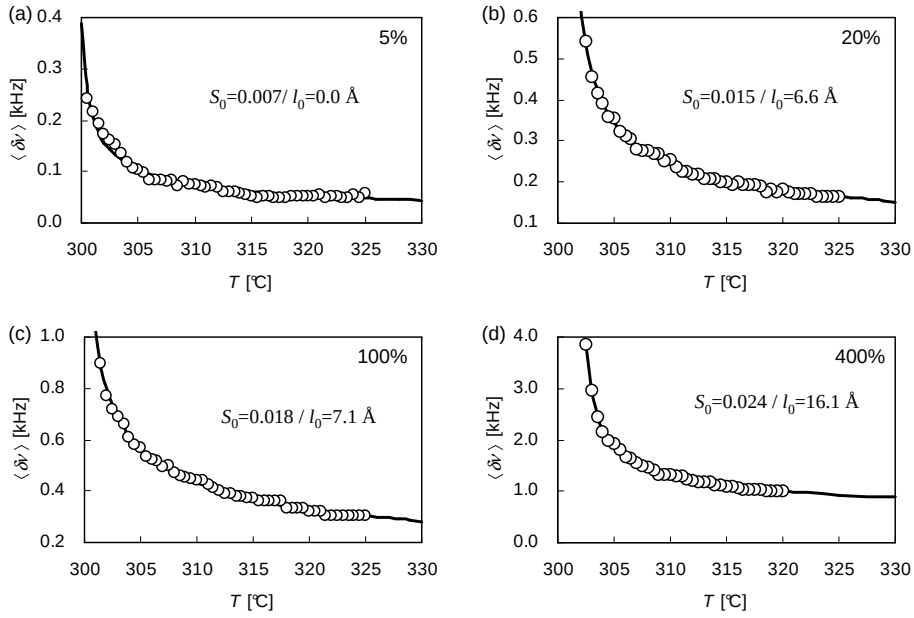

Figure A.10: Temperature dependence of the quadrupole splitting frequency $\langle\delta\nu\rangle$ of 5%, 20%, 100% and 400% stretched PDLCs in the isotropic phase. The solid curve in the figure is the best fit result for the temperature-independent model given by Eqs. (A.19) and (A.21). R and ρ are determined by Eq. (**??**) and Eq. (A.17), respectively. E_ξ and E_l are calculated by Eq. (A.15).

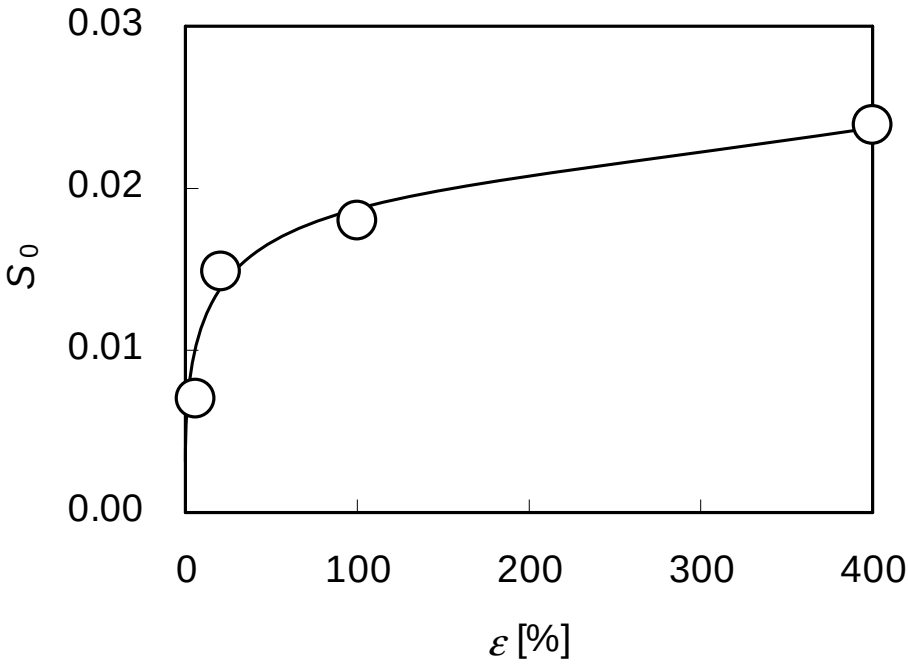

Figure A.11: The dependence of S_0 on the strain.

polymer chain alignment induced by uniaxial stretching, as already reported in Ref. [106]. According to the stress-strain curve of the PDLC film, the elastic region where the polymer chains have not disentangled appears between 0% and 7% strain, the disentanglement region appears from 7% to 35% strain, and the sliding regime appears greater than 35% strain. Therefore, NMR results indicate that the polymer chain orientation does influence the liquid crystal molecules on the polymer surface in the isotropic phase.

From the validity condition for the temperature-independent model one can estimate the two parameters that characterize the nematic coupling with the polymer substrate, g and S_s. For the coupling strength g one can derive the lower limit, i.e., $g \gg \frac{1}{2}\sqrt{a(T-T^*)L} \geq \frac{1}{2}\sqrt{a(T_{NI}-T^*)L}$, while for the surface-imposed degree of order S_s one has $S_s \approx S_0$. S_0, l_0, $T_{NI}-T^*$, and the limiting g are summarized in Table A.1, assuming $L = 1.7 \times 10^{-11}$ J/m and $a = 0.1319 \times 10^6$ J/m^{3}K [112].

Table A.1: Summary of interfacial parameters for 5CB-αd_2 confined in elliptical droplets of stretched PDLC films.

ϵ [%]	S_0 [-]	l_0 [Å]	$T_{NI}-T^*$ [K]	$\frac{1}{2}\sqrt{a(T_{NI}-T^*)L}$ $\times 10^{-4}$ [J/m^2]
5	0.007	0.0	0.64 ± 0.25	5.99 ± 1.19
20	0.015	6.6	1.29 ± 0.25	8.50 ± 0.83
100	0.018	7.1	1.30 ± 0.25	8.54 ± 0.83
400	0.024	16.1	0.33 ± 0.25	4.30 ± 1.79

A.5 Monte Carlo Simulations

In this section we briefly describe the Monte Carlo simulations of paranematic ordering in nematic droplets for a strained PDLC sample, where the deformation of the polymer matrix is assumed to result in an ellipsoidal droplet shape. There are several reasons for performing these MC simulations: (i) they avoid the simplifying assumptions used in the phenomenological part of the study, (ii) they provide direct insight into molecular ordering mechanisms, and (iii) they can be used to predict dynamic NMR spectra. Our simulations are based on the Lebwohl-Lasher (LL) lattice model [113]

in which uniaxial nematic molecules or close-packed molecular clusters are represented by unit vectors ("particles") $\mathbf{u}_i$. The particles are fixed onto sites of a cubic lattice whose lattice spacing p is estimated as 1 nm $\leq p \leq$ 5 nm assuming the molecular clusters contain up to 10^2 nematic molecules [99]. The standard N-particle LL Hamiltonian reads [99, 113]

$$U_N = -\sum_{\langle i<j \rangle} \epsilon \, P_2(\mathbf{u}_i \cdot \mathbf{u}_j), \tag{A.24}$$

where $P_2(x) = \frac{1}{2}(3x^2 - 1)$, $\epsilon > 0$ is a constant, and the sum runs over nearest-neighbor particles only. The Hamiltonian (A.24) promotes parallel alignment, which facilitates the formation of the nematic phase. The boundary conditions are determined by a layer of "ghost" particles, whose orientations are fixed during the simulation. In our case we choose perfect bipolar boundary conditions – appropriately rescaled for strained droplets – in agreement with the experimental observations reported in Sect. A.3. Moreover, the bipolar and the tensile axes are chosen to coincide. The interaction strength ϵ is assumed equal for nematic-nematic and nematic-ghost interactions, which implies strong anchoring, as already assumed in Sect. A.4.1.

Because of the strong confinement translational diffusion cannot be ignored in the simulation of the NMR experiment (see the estimate in Sect. A.2). The calculation of the ^{2}H-NMR spectra from the MC simulation output hence follows the procedure described in Refs. [100, 101], which is applicable in the presence of significant molecular motion. First, the free induction decay signal is generated in a reference frame rotating with the Larmor frequency, i.e.,

$$G(t) = \Big\langle \exp\big[i \int_0^t \Omega_Q^j(t') \, dt'\big] \Big\rangle_j, \tag{A.25}$$

and is then Fourier-transformed to yield the spectrum $I(\delta\nu) = \int \exp(i\, 2\pi\delta\nu t) G(t) dt$. In Eq. (A.25)

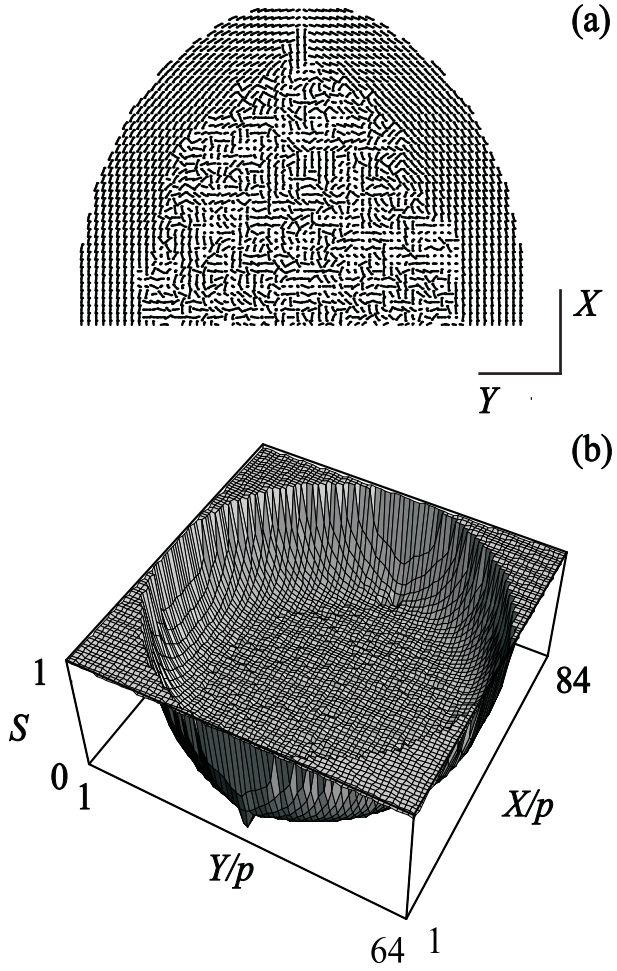

Figure A.12: Bipolar droplet with 20% strain: typical simulated director field (a) and nematic order parameter map (b) (half and whole XY cross section through droplet center, respectively), calculated by diagonalizing the MC-time averaged local ordering matrix $\mathsf{Q}(i) = \frac{1}{2}(3\langle \mathbf{u}_i \otimes \mathbf{u}_i \rangle - \mathsf{I})$ [1].

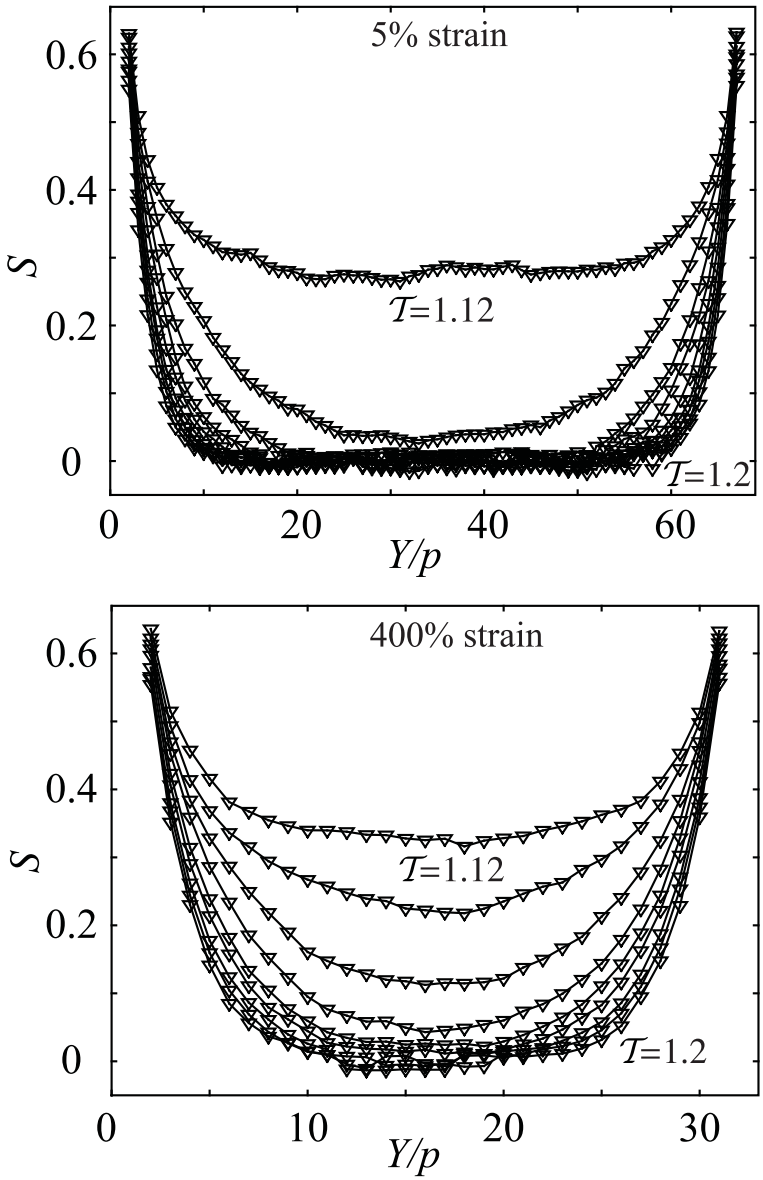

Figure A.13: Temperature scans of order parameter profiles plotted through the droplet center along the Y-axis: (a) 5% strain, (b) 400% strain; temperature range $\mathcal{T} = 1.12-1.20$ (curves top to bottom, step size 0.01). The subsurface degree of order S_0 shows no major temperature dependence and thus supports the temperature-independent model, Eq. (A.19).

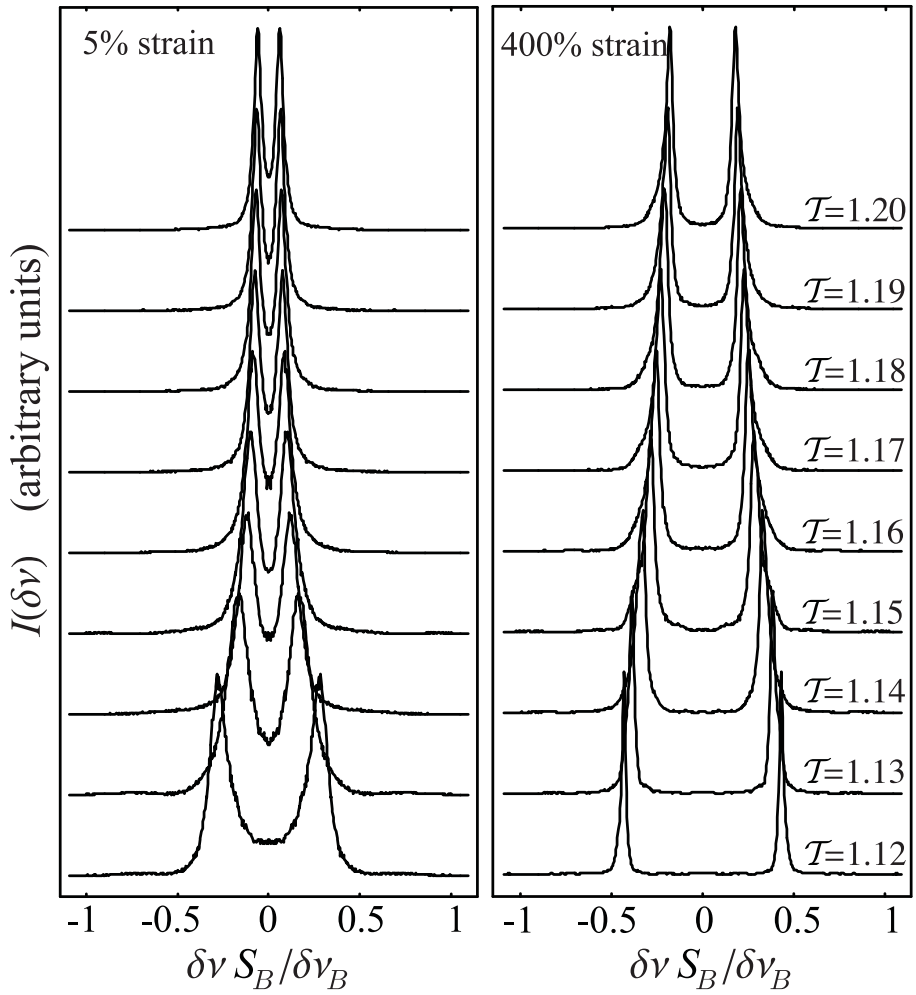

Figure A.14: Strained bipolar droplets: ^{2}H-NMR spectra; (a) 5% strain, (b) 400% strain. The quadrupole splitting decreases with temperature and increases with strain.

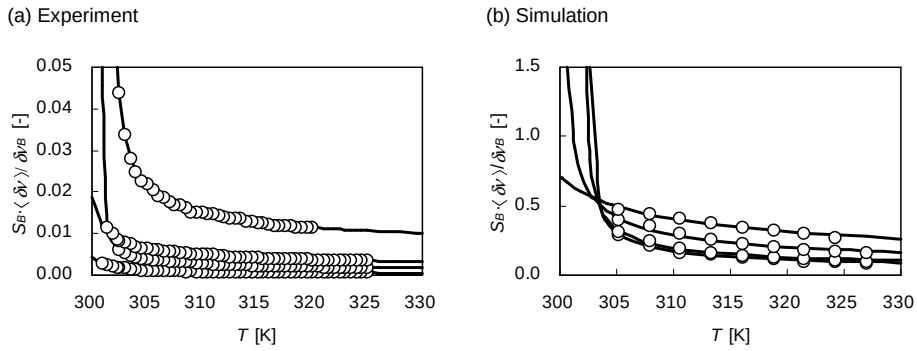

Figure A.15: Strained bipolar droplets: temperature dependence of the simulated quadrupolar splitting. Top to bottom: 400%, 100%, 20%, 5% strain, and no strain (for comparison only). Experimental (*left*) vs. simulated data (*right*). Bulk NI transition temperature for 5CB is 308 K, while for the LL model it is $\mathcal{T}_{NI} = 1.1232$.

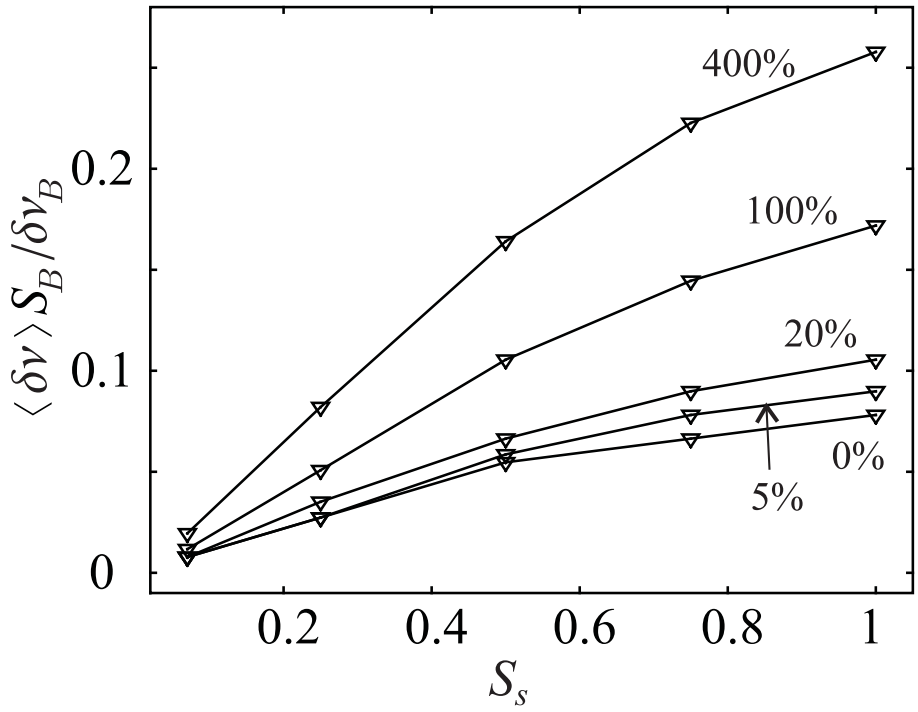

Figure A.16: Strained bipolar droplets: surface roughness dependence of the simulated quadrupolar splitting. Top to bottom: 400%, 100%, 20%, 5% strain, and no strain (for comparison only). On the abscissa the degree of surface-imposed order S_s is plotted. $\mathcal{T} = 1.16$ in all cases.

one has $\Omega_Q^j(t) = \pm\pi\delta\nu_B S_B^{-1}\left[3(\mathbf{u}_j \cdot \mathbf{b})^2 - 1\right]$, where $\mathbf{u}_j = \mathbf{u}_j(t)$ stand for the 'instantaneous' orientation of the jth particle, $\mathbf{b}$ represents a unit vector along the magnetic field of the NMR spectrometer, and $\langle ... \rangle_j$ denotes an ensemble average over all particles in the sample. The orientations $\mathbf{u}_j$ are obtained on the fly from the MC simulation, reproducing the effect of fluctuating molecular long axes. In addition, translational diffusion is simulated by an isotropic and homogeneous random walk process on the lattice [100, 101].

The simulation box size was set to $70 \times 70 \times 70$ particles, allowing us to study droplets of size $68p$ in diameter. This already approaches 92 nm, the average droplet size in our experiment (see the above estimate for p). In the case of strain, the simulation box dimensions were adjusted according to Eq. (A.1) to roughly maintain the volume of the droplet (approximately 172000 particles): $68 \times 68 \times 74$, $64 \times 64 \times 84$, $50 \times 50 \times 138$, and $32 \times 32 \times 342$ for 5%, 20%, 100%, and 400% strain, respectively. For each droplet geometry a separate temperature scan was performed, starting from a random configuration at $\mathcal{T} = k_B T/\epsilon = 1.2$ and then simulating a gradual cooling down to $\mathcal{T} = 1.12$ with a step of $\Delta\mathcal{T} = 0.01$ (recall that the NI transition in the bulk LL model occurs at $\mathcal{T}_{NI} \approx 1.1232$ [99]). At each temperature, 85000 MC cycles were performed for equilibration, followed by 265000 production cycles. During the acquisition of the FID signal, 1024 diffusion steps per NMR cycle were performed. This gives a root-mean-square molecular displacement of $32p$ per NMR cycle in the nematic phase [1] (and correspondingly more in the isotropic phase), which is already comparable to the unstrained droplet radius ($34p$) and thus approaches the fast diffusion limit. As in the experiment, the spectrometer's magnetic field was applied along the bipolar (tensile) axis, i.e., B parallel to X.

Figure A.12(a) shows the director field for the droplet with 20% strain. Bipolar paranematic ordering is well-pronounced only in the vicinity of the substrate, with molecules on average aligned along the droplet symmetry axis, while in the bulk the isotropic phase is restored. This surface-induced ordering is characterized by a nonzero nematic order parameter (see Figure A.12(b)) decaying to zero approximately exponentially as assumed in Sect. A.4, with a characteristic length

$\xi \sim 4p$ on moving away from the substrate. This is also obvious from Figure A.13, showing the nematic order parameter profiles for different temperatures, plotted along one of the short principal axes of the droplet. Further, one can clearly see the temperature dependence of the characteristic length ξ, and the subsurface value of the order parameter (S_0) exhibit a rather weak temperature dependence. The latter observation supports the use of the temperature-independent model given by Eq. (A.19). There is, however, no major strain dependence for S_0 values since in the simulation the stretching process is only taken to affect the droplet shape, while only perfect (i.e. smooth) boundary conditions are considered. Note also that for strongly strained droplets (e.g. 400%) the length of the short droplet axis is substantially reduced, which leads to a capillary condensation-like effect: due to the proximity of the opposing walls nematic order is restored throughout the droplet even at temperatures several percent above the bulk T_{NI} (Figure A.13).

Examples of the simulated ^{2}H-NMR spectra are shown in Figure A.14. Note that all of the spectra are double-peaked, with no additional structure, which indicates they are indeed highly diffusion-averaged. The temperature dependences of the quadrupolar splitting for all droplets (estimated from the peak-to-peak distance for each spectrum) are summarized in Figure A.15. One can readily observe the splitting decreases with increasing temperature and increases with strain, both of which are also seen experimentally. The former effect is mainly because of the decrease of ξ, i.e., the thickness of the paranematically ordered subsurface layer, while the latter is due to a more pronounced orientation of nematic molecules along the tensile axis (and the spectrometer magnetic field), as well as due to an increase of the droplet surface area upon stretching the polymer matrix. Note, however, that all of the simulated values of the quadrupole splitting are noticeably higher than the experimental ones. This is a consequence of the rather strong coupling between the nematic and ghost particles chosen in the simulation, resulting in an overestimate of the degree of paranematic order, including S_0. On the other hand, examining the relative increase of the quadrupole splitting upon stretching at a given temperature, one observes that at all temperatures the increase in the experimental value is significantly larger than those in simulation. Recall again that the simulations

presented so far were performed with perfectly smooth bipolar boundary conditions at the droplet surface, while the actual appearance of the polymer substrate is far from smooth. Imperfections of the polymer surface lead to a decrease of the subsurface degree of ordering S_0 [1], which in a real system seems to be the case especially for weakly strained droplets trapped within a fairly disordered polymer. Then, with increasing strain, polymer fibers disentangle, which is accompanied by an increase of S_0 (see Figure A.11). In the simulated model systems we have shown the increase of the quadrupolar frequency with stretching can be attributed solely to the change of droplet shape. In a real system this effect seems to be enhanced by the disentanglement process in the polymer matrix.

For this reason, a set of simulations for partially disordered droplet surfaces has also been performed. A perturbation of bipolar boundary conditions was generated following a P_2-type orientational distribution with a controllable degree of surface order S_s as in Ref. [1]. This modification indeed reduces the quadrupole splitting, as can be easily concluded from Figure A.16. However, if a realistic degree of subsurface order is to be approached, the magnitude of the resulting splitting already approaches the resolution of our spectra, which makes a more quantitative analysis rather impossible.

A.6 Conclusion

We reported on the alignment of 5CB-αd_2 in stretched PDLCs using ^{2}H-NMR measurement. We have directly observed the liquid crystal alignment along the tensile axis in the nematic phase. We have investigated the surface ordering behavior based on a Landau-de Gennes theory. We have proposed an elliptical model, which describes the surface ordering behavior of liquid crystal molecules confined in an elliptical cavity. The surface order parameter can be described by the temperature-independent model and the surface order parameters increases as the strain increases. The strain dependence of S_0 corresponded to the result from the optomechanical measurements [106]

that the polymer chain orientation surrounding liquid crystal molecules during stretching influenced the liquid crystal alignment. Experimental results were well correlated with the qualitative trends obtained from Monte Carlo simulations of paranematic ordering in elliptical droplets.

Bibliography

[1] C. Chiccoli, P. Pasini, G. Skacej, C. Zannoni, and S. Zumer. Polymer network-induced ordering in a nematogenic liquid: A monte carlo study. *Physical Review E*, 65(5), 2002. Part 1.

[2] F. Reinitzer. Beitrage zur kinntniss des cholesterins. *Monatshefte fur Chemie / Chemical Monthy*, 9(1):421–444, 1888.

[3] P. G. de Gennes and J. Prost. *The Physics of Liquid Crystals*. Claredon Press, Oxford, 1993.

[4] P. Collins and M. Hurd. *Introduction to Liquid Crystals*. Taylor and Francis, London, 1997.

[5] W. Maier and A. Saupe. *Z. Naturforsch*, 14(a):882, 1959.

[6] J. Chen, P. J. Bos, H. Vithana, and D. L. Johnson. An electrooptically controlled liquid-crystal diffraction grating. *Applied Physics Letters*, 67(18):2588–2590, 1995.

[7] S. Varghese, G. P. Crawford, C. W. M. Bastiaansen, D. K. G. de Boer, and D. J. Broer. Microrubbing technique to-produce high pretilt multidomain liquid crystal alignment. *Applied Physics Letters*, 85(2):230–232, 2004.

[8] S. Varghese, S. Narayanankutty, C. W. M. Bastiaansen, G. P. Crawford, and D. J. Broer. Patterned alignment of liquid crystals by mu-rubbing. *Advanced Materials*, 16(18):1600–+, 2004.

[9] M. Honma and T. Nose. Liquid-crystal reflective beam deflector with microscale alignment pattern. *Japanese Journal of Applied Physics Part 1-Regular Papers Short Notes Review Papers*, 43(12):8151–8155, 2004.

[10] M. Honma, K. Yamamoto, and T. Nose. Periodic reverse-twist nematic domains obtained by microrubbing patterns. *Journal of Applied Physics*, 96(10):5415–5419, 2004.

[11] C. Rosenblatt. *Molecular Crystals and Liquid Crystals*, 412:1727, 2004.

[12] W. M. Gibbons, P. J. Shannon, S. T. Sun, and B. J. Swetlin. Surface-mediated alignment of nematic liquid-crystals with polarized laser-light. *Nature*, 351(6321):49–50, 1991.

[13] M. Schadt, H. Seiberle, and A. Schuster. Optical patterning of multidomain liquid-crystal displays with wide viewing angles. *Nature*, 381(6579):212–215, 1996.

[14] B. Wen, R. G. Petschek, and C. Rosenblatt. Nematic liquid-crystal polarization gratings by modification of surface alignment. *Applied Optics*, 41(7):1246–1250, 2002.

[15] J. D. Jackson. *Classical Electrodynamics*. Wiley, New York, 1998.

[16] D. J. Griffiths. *Introduction to Electrodynamics*. Prentice Hall, New York, 1998.

[17] L. Nikolova and T. Todorov. Diffraction efficiency and selectivity of polarization holographic recording. *Optica Acta*, 31(5):579–588, 1984.

[18] P. Hariharan. *Optical Holography: Principles, Techniques, and Applications*. Cambridge University Press, New York, 1996.

[19] J. N. Eakin, Y. Xie, R. A. Pelcovits, and G. P. Crawford. Patterned alignment layers using holographic exposure technique. *SID Digest of Technical Papers*, XXXV:578–581, 2004.

[20] J. N. Eakin, Y. Xie, R. A. Pelcovits, M. D. Radcliffe, and G. P. Crawford. Zero voltage freedericksz transition in periodically aligned liquid crystals. *Applied Physics Letters*, 85(10):1671–1673, 2004.

[21] L. Komitov, G. P. Bryan-Brown, E. L. Wood, and A. B. J. Smout. Alignment of cholesteric liquid crystals using periodic anchoring. *Journal of Applied Physics*, 86(7):3508–3511, 1999.

[22] T. Shioda, B. Wen, and C. Rosenblatt. Step-wise freedericksz transition in a nematic liquid crystal. *Journal of Applied Physics*, 94(12):7502–7504, 2003.

[23] H. Sarkissian, J. B. Park, Z. B. Ya, and N. V. Tabirian. In *Abstract of the Confeerence on Lasers and Electro-Optics*, Baltimore, MD, 2005.

[24] H. Sarkissian, N. V. Tabirian, B. Park, and B. Zeldovich.

[25] D. J. Versteeg, C. W. M. Bastiaansen, and D. J. Broer. Influence of laser writing of polyimides on the alignment of liquid crystals. *Journal of Applied Physics*, 91(7):4191–4195, 2002.

[26] G. P. Sinha, C. Rosenblatt, and L. V. Mirantsev. Disruption of surface-induced smectic order by periodic surface corrugations. *Physical Review E*, 65(4), 2002. Part 1.

[27] B. W. Lee and N. A. Clark. Alignment of liquid crystals with patterned isotropic surfaces. *Science*, 291(5513):2576–2580, 2001.

[28] S. G. Cloutier, D. A. Peyrot, T. V. Galstian, and R. A. Lessard. Measurement of permanent vectorial photoinduced anisotropy in azo-dye-doped photoresist using polarization holography. *Journal of Optics a-Pure and Applied Optics*, 4(6):S228–S234, 2002.

[29] M. J. Escuti, C. Oh, C. Sanchez, C. W. M. Bastiaansen, and D. J. Broer. Simplified spectropolarimetry using reactive mesogen polarization gratings. *Proceedings of SPIE*, 6302:630207, 2006.

[30] G. P. Crawford, R. Ondriscrawford, S. Zumer, and J. W. Doane. Anchoring and orientational wetting transitions of confined liquid-crystals. *Physical Review Letters*, 70(12):1838–1841, 1993.

[31] M. J. Escuti and W. M. Jones. A polarization-independent liquid crystal spatial-light-modulator. *Proceedings of SPIE*, 6332:63320M, 2006.

[32] I. Janossy, A. Jakli, G. G. Nair, K. K. Raina, and T. Kosa. Optical control of the alignment of a liquid crystal in the smectic a phase. *Molecular Crystals and Liquid Crystals Science and Technology Section a-Molecular Crystals and Liquid Crystals*, 329:1119–+, 1999. Part 2.

[33] I. Janossy, A. Vajda, T. Paksi, and T. Kosa. Photoinduced surface alignment: The role of liquid-crystalline order. *Molecular Crystals and Liquid Crystals*, 359:477–486, 2001.

[34] I. Janossy. Photo-orientation at liquid crystal-polymer interfaces. *Pramana-Journal of Physics*, 61(2):435–445, 2003.

[35] G. S. He, T. C. Lin, V. K. S. Hsiao, A. N. Cartwright, P. N. Prasad, L. V. Natarajan, V. P. Tondiglia, R. Jakubiak, R. A. Vaia, and T. J. Bunning. Tunable two-photon pumped lasing using a holographic polymer-dispersed liquid-crystal grating as a distributed feedback element. *Applied Physics Letters*, 83(14):2733–2735, 2003.

[36] D. E. Lucchetta, L. Criante, O. Francescangeli, and F. Simoni. Wavelength flipping in laser emission driven by a switchable holographic grating. *Applied Physics Letters*, 84(6):837–839, 2004.

[37] D. E. Lucchetta, L. Criante, O. Francescangeli, and F. Simoni. Compact lasers based on hpdlc gratings. *Molecular Crystals and Liquid Crystals*, 441:97–109, 2005.

[38] S. J. Woltman, M. E. Sousa, H. Zhang, and G. P. Crawford. Survey of switchable lasing configurations using structures of liquid crystal and polymer dispersions. *Proceedings of SPIE*, 6135(6150B), 2006.

[39] J. Qi and G. P. Crawford. Holographically formed polymer dispersed liquid crystal displays. *Displays*, 25(5):177–186, 2004.

[40] J. Qi, M. E. Sousa, and G. P. Crawford. Reflective display configurations based on total internal reflection and grating-grating coupling of holographic polymer dispersed liquid crystals (h-pdlc). *Molecular Crystals and Liquid Crystals*, 433:267–277, 2005.

[41] C. C. Bowley and G. P. Crawford. Diffusion kinetics of formation of holographic polymer-dispersed liquid crystal display materials. *Applied Physics Letters*, 76(16):2235–2237, 2000.

[42] M. L. Ermold and A. K. Fontecchio. Electrically switchable holographic parabolic mirrors. *Journal of Applied Physics*, 99(9), 2006.

[43] H. L. Zhang, H. Q. Xianyu, J. H. Liang, Y. Betremieux, G. P. Crawford, J. Noto, and R. Kerr. Switchable circular-to-point converter based on holographic polymer-dispersed liquid-crystal technology. *Applied Optics*, 46(2):161–166, 2007.

[44] T. J. Bunning, L. V. Natarajan, V. Tondiglia, R. L. Sutherland, D. L. Vezie, and W. W. Adams. The morphology and performance of holographic transmission gratings recorded in polymer-dispersed liquid-crystals. *Polymer*, 36(14):2699–2708, 1995.

[45] T. J. Bunning, L. V. Natarajan, V. P. Tondiglia, and R. L. Sutherland. Holographic polymer-dispersed liquid crystals (h-pdlcs). *Annual Review of Materials Science*, 30:83–115, 2000.

[46] G. P. Crawford. Electrically switchable bragg gratings. *Optics and Photonics News*, 14(4):55–59, 2003.

[47] C. C. Bowley and G. P. Crawford. Improved reflective displays based on polymer-dispersed liquid crystals. *Journal of Optical Technology*, 67(8):717–722, 2000.

[48] L. V. Natarajan, C. K. Shepherd, D. M. Brandelik, R. L. Sutherland, S. Chandra, V. P. Tondiglia, D. Tomlin, and T. J. Bunning. Switchable holographic polymer-dispersed liquid crystal reflection gratings based on thiol-ene photopolymerization. *Chemistry of Materials*, 15(12):2477–2484, 2003.

[49] L. V. Natarajan, D. P. Brown, J. M. Wofford, V. P. Tondiglia, R. L. Sutherland, P. F. Lloyd, and T. J. Bunning. Holographic polymer dispersed liquid crystal reflection gratings formed by visible light initiated thiol-ene photopolymerization. *Polymer*, 47(12):4411–4420, 2006.

[50] G. Cipparrone, A. Mazzulla, and G. Russo. Diffraction gratings in polymer-dispersed liquid crystals recorded by means of polarization holographic technique. *Applied Physics Letters*, 78(9):1186–1188, 2001.

[51] M. J. Escuti, J. Qi, and G. P. Crawford. Two-dimensional tunable photonic crystal formed in a liquid-crystal/polymer composite: Threshold behavior and morphology. *Applied Physics Letters*, 83(7):1331–1333, 2003.

[52] M. J. Escuti, J. Qi, and G. P. Crawford. Tunable face-centered-cubic photonic crystal formed in holographic polymer dispersed liquid crystals. *Optics Letters*, 28(7):522–524, 2003.

[53] R. L. Sutherland, V. P. Tondiglia, L. V. Natarajan, S. Chandra, D. Tomlin, and T. J. Bunning. Switchable orthorhombic f photonic crystals formed by holographic polymerization-induced phase separation of liquid crystal. *Optics Express*, 10(20):1074–1082, 2002.

[54] S. P. Gorkhali, J. Qi, and G. P. Crawford. Electrically switchable mesoscale penrose quasicrystal structure. *Applied Physics Letters*, 86(1), 2005.

[55] S. P. Gorkhali, S. G. Cloutier, and G. P. Crawford. Two-dimensional vectorial photonic crystals formed in azo-dye-doped liquid crystals. *Optics Letters*, 31(22):3336–3338, 2006.

[56] M. De Sarkar, J. Qi, and G. P. Crawford. Influence of partial matrix fluorination on morphology and performance of hpdlc transmission gratings. *Polymer*, 43(26):7335–7344, 2002.

[57] M. De Sarkar, N. L. Gill, J. B. Whitehead, and G. P. Crawford. Effect of monomer functionality on the morphology and performance of the holographic transmission gratings recorded on polymer dispersed liquid crystals. *Macromolecules*, 36(3):630–638, 2003.

[58] K. K. Vardanyan, J. Qi, J. N. Eakin, M. De Sarkar, and G. P. Crawford. Polymer scaffolding model for holographic polymer-dispersed liquid crystals. *Applied Physics Letters*, 81(25):4736–4738, 2002.

[59] R. Caputo, A. Veltri, C. P. Umeton, and A. V. Sukhov. Characterization of the diffraction efficiency of new holographic gratings with a nematic film-polymer-slice sequence structure. *Journal of the Optical Society of America B-Optical Physics*, 21(11):1939–1947, 2004.

[60] G. Abbate, F. Vita, A. Marino, V. Tkachenko, S. Slussarenko, O. Sakhno, and J. Stumpe. New generation of holographic gratings based on polymer-lc composites: Policryps and poliphem. *Molecular Crystals and Liquid Crystals*, 453:1–13, 2006.

[61] A. d'Alessandro, R. Asquini, C. Gizzi, R. Caputo, C. Umeton, A. Veltri, and A. V. Sukhov. Electro-optic properties of switchable gratings made of polymer and nematic liquid-crystal slices. *Optics Letters*, 29(12):1405–1407, 2004.

[62] R. L. Sutherland, L. V. Natarajan, V. P. Tondiglia, S. Chandra, C. K. Shepherd, D. M. Brandelik, S. A. Siwecki, and T. J. Bunning. Polarization and switching properties of holographic polymer-dispersed liquid-crystal gratings. ii. experimental investigations. *Journal of the Optical Society of America B-Optical Physics*, 19(12):3004–3012, 2002.

[63] R. L. Sutherland. Polarization and switching properties of holographic polymer-dispersed liquid-crystal gratings. i. theoretical model. *Journal of the Optical Society of America B-Optical Physics*, 19(12):2995–3003, 2002.

[64] Y. J. Liu, B. Zhang, Y. Jia, and K. S. Xu. Improvement of the diffraction properties in holographic polymer dispersed liquid crystal bragg gratings. *Optics Communications*, 218(1-3):27–32, 2003.

[65] H. Molsen and H. S. Kitzerow. Bistability in polymer-dispersed ferroelectric liquid-crystals. *Journal of Applied Physics*, 75(2):710–716, 1994.

[66] H. S. Kitzerow, H. Molsen, and G. Heppke. Linear electrooptic effects in polymer-dispersed ferroelectric liquid-crystals. *Applied Physics Letters*, 60(25):3093–3095, 1992.

[67] H. S. Kitzerow. Polymer-dispersed liquid-crystals - from the nematic curvilinear aligned phase to ferroelectric-films. *Liquid Crystals*, 16(1):1–31, 1994.

[68] J. W. McMurdy, G. P. Crawford, and G. D. Jay. Monolithic microspectrometer using tunable ferroelectric liquid crystals. *Applied Physics Letters*, 89(8), 2006.

[69] R. Karapinar and M. O'Neill. Electro-optical switching properties of a polymer dispersed ferroelectric liquid crystal device. *Journal of Physics D-Applied Physics*, 31(7):900–905, 1998.

[70] S. J. Woltman, J. N. Eakin, G. P. Crawford, and S. Zumer. Holographic diffraction gratings using polymer-dispersed ferroelectric liquid crystals. *Optics Letters*, 31(22):3273–3275, 2006.

[71] J. N. Eakin, G. P. Crawford, and M. D. Radcliffe. Morphological studies of holographically formed polymer dispersed ferroelectric liquid crystals using elevated temperature exposure. *Molecular Crystals and Liquid Crystals*, 439:1889–+, 2005.

[72] J. N. Eakin, G. P. Crawford, and M. D. Radcliffe. Morphological studies of holographically formed polymer dispersed ferroelectric liquid crystals. *Molecular Crystals and Liquid Crystals*, 429:277–+, 2005.

[73] C. M. Leader, W. Zheng, J. Tipping, and H. J. Coles. Shear aligned polymer-dispersed ferroelectric liquid-crystal devices. *Liquid Crystals*, 19(4):415–419, 1995.

[74] J. Qi, M. E. Sousa, A. K. Fontecchio, and G. P. Crawford. Temporally multiplexed holographic polymer-dispersed liquid crystals. *Applied Physics Letters*, 82(11):1652–1654, 2003.

[75] G. Cipparrone, A. Mazzulla, M. V. Kozlovsky, S. P. Palto, S. G. Yudin, and L. M. Blinov. Polarization gratings in photosensitive langmuir-blodgett films and chiral liquid crystalline polymers. *Molecular Materials*, 12(4):359–376, 2000.

[76] J. Tervo and J. Turunen. Paraxial-domain diffractive elements with 100polarization gratings. *Optics Letters*, 25(11):785–786, 2000.

[77] W. Y. Zhang, S. P. Bian, S. I. Kim, and M. G. Kuzyk. High-efficiency holographic volume index gratings in dr1-dye-doped poly(methyl methacrylate). *Optics Letters*, 27(13):1105–1107, 2002.

[78] M. J. Escuti, C. Oh, C. Sanchez, C. W. M. Bastiaansen, and D. J. Broer. Simplified spectropolarimetry using reactive mesogen polarization gratings. *Proceedings of SPIE*, 6302:630207, 2006.

[79] P. Sheng. Boundary-layer phase-transition in nematic liquid-crystals. *Physical Review A*, 26(3):1610–1617, 1982.

[80] T.J. Sluckin and A. Poniewierski. Chapter 5. In *Fluid Interfacial Phenomena*. Wiley, New York, 1986.

[81] G. P. Crawford, R. J. OndrisCrawford, and J. W. Doane. Systematic study of orientational wetting and anchoring at a liquid-crystal-surfactant interface. *Physical Review E*, 53(4):3647–3661, 1996. Part B.

[82] K. Miyano. Surface-induced ordering of a liquid-crystal in the isotropic-phase. *Journal of Chemical Physics*, 71(10):4108–4111, 1979.

[83] R. Barberi and G. Durand. Order parameter of a nematic liquid-crystal on a rough-surface. *Physical Review A*, 41(4):2207–2210, 1990.

[84] W. Chen, L. J. Martinezmiranda, H. Hsiung, and Y. R. Shen. Orientational wetting behavior of a liquid-crystal homologous series. *Physical Review Letters*, 62(16):1860–1863, 1989.

[85] G. P. Crawford, D. K. Yang, S. Zumer, D. Finotello, and J. W. Doane. Ordering and self-diffusion in the 1st molecular layer at a liquid-crystal polymer interface. *Physical Review Letters*, 66(6):723–726, 1991.

[86] G. P. Crawford, R. Stannarius, and J. W. Doane. Surface-induced orientational order in the isotropic-phase of a liquid-crystal material. *Physical Review A*, 44(4):2558–2569, 1991.

[87] P. Ziherl, M. Vilfan, N. Vrbancic-Kopac, S. Zumer, R. J. Ondris-Crawford, and G. P. Crawford. Substrate-induced order in the isotropic phase of a smectogenic liquid crystal: A deuteron nmr study. *Physical Review E*, 61(3):2792–2798, 2000.

[88] T. Jin, G. P. Crawford, R. J. Crawford, S. Zumer, and D. Finotello. Surface ordering transitions at a liquid crystal-solid interface above the isotropic smectic-a transition. *Physical Review Letters*, 90(1):015504, 2003.

[89] G. S. Iannacchione, G. P. Crawford, S. Zumer, J. W. Doane, and D. Finotello. Randomly constrained orientational order in porous-glass. *Physical Review Letters*, 71(16):2595–2598, 1993.

[90] G. S. Iannacchione, G. P. Crawford, S. Qian, J. W. Doane, and D. Finotello. Nematic ordering in highly restrictive vycor glass. *Physical Review E*, 53(3):2402–2411, 1996.

[91] G. S. Iannacchione, S. H. Qian, G. P. Crawford, S. S. Keast, M. E. Neubert, J. W. Doane, D. Finotello, L. M. Steele, P. E. Sokol, and S. Zumer. Liquid crystal order in a highly restrictive porous glass. *Molecular Crystals and Liquid Crystals Science and Technology Section a-Molecular Crystals and Liquid Crystals*, 262:13–23, 1995.

[92] S. Kralj, G. Lahajnar, A. Zidansek, N. Vrbancickopac, M. Vilfan, R. Blinc, and M. Kosec. Deuterium nmr of a pentylcyanobiphenyl liquid-crystal confined in a silica aerogel matrix. *Physical Review E*, 48(1):340–349, 1993.

[93] D. Finotello, H. Zeng, B. Zalar, and G. S. Iannacchione. Nematic structures in randomly interconnected porous hosts. *Molecular Crystals and Liquid Crystals*, 358:237–250, 2001.

[94] B. Zalar, R. Blinc, S. Zumer, T. Jin, and D. Finotello. Behavior of mesogenic molecules deposited at the alumina-air interface: A deuteron nmr study. *Physical Review E*, 65(4), 2002. Part 1.

[95] G. P. Crawford and S. Zumer, editors. *Liquid Crystals in Complex Geometries*. Taylor and Francis, London, 1996.

[96] A. Golemme, S. Zumer, D. W. Allender, and J. W. Doane. Continuous nematic-isotropic transition in submicron-size liquid-crystal droplets. *Physical Review Letters*, 61(26):2937–2940, 1988.

[97] I. Vilfan, M. Vilfan, and S. Zumer. Orientational order in bipolar nematic microdroplets close to the phase-transition. *Physical Review A*, 40(8):4724–4730, 1989.

[98] M. Vilfan, N. Vrbancic-Kopac, B. Zalar, S. Zumer, and G. P. Crawford. Measurement of the surface-induced order in polymer dispersed liquid crystals: An approach by nmr relaxometry. *Physical Review E*, 59(5):R4754–R4757, 1999. Part A.

[99] P. Pasini and C. Zannoni, editors. *Advances in the Computer Simulations of Liquid Crystals*. Dordrecht, 2000.

[100] C. Chiccoli, P. Pasini, G. Skacej, C. Zannoni, and S. Zumer. Nmr spectra from monte carlo simulations of polymer dispersed liquid crystals. *Physical Review E*, 60(4):4219–4225, 1999. Part B.

[101] C. Chiccoli, P. Pasini, G. Skacej, C. Zannoni, and S. Zumer. Dynamical and field effects in polymer-dispersed liquid crystals: Monte carlo simulations of nmr spectra. *Physical Review E*, 62(3):3766–3774, 2000. Part B.

[102] R. K. Bharadwaj, T. J. Bunning, and B. L. Farmer. A mesoscale modelling study of nematic liquid crystals confined to ellipsoidal domains. *Liquid Crystals*, 27(5):591–603, 2000.

[103] I. Amimori, J. N. Eakin, G. P. Crawford, N. V. Priezjev, and R. A. Pelcovits. Optical and mechanical properties of stretchedpdlc films for scattering polarizers. *SID International Symposium Digest of Technical Papers*, XXXIII:834–837, 2002.

[104] P. S. Drzaic, editor. *Liquid Crystal Dispersions*. World Scientific, Sinapore, 1995.

[105] O. A. Aphonin, Y. V. Panina, A. B. Pravdin, and D. A. Yakovlev. Optical-properties of stretched polymer-dispersed liquid-crystal films. *Liquid Crystals*, 15(3):395–407, 1993.

[106] I. Amimori, N. V. Priezjev, R. A. Pelcovits, and G. P. Crawford. Optomechanical properties of stretched polymer dispersed liquid crystal films for scattering polarizer applications. *Journal of Applied Physics*, 93(6):3248–3252, 2003.

[107] P. S. Drzaic. Polymer dispersed nematic liquid-crystal for large area displays and light valves. *Journal of Applied Physics*, 60(6):2142–2148, 1986.

[108] B. G. Wu, J. H. Erdmann, and J. W. Doane. Response-times and voltages for pdlc light shutters. *Liquid Crystals*, 5(5):1453–1465, 1989.

[109] L.H. Sperling. *Introduction to Physical Polymer Science*. John Wiley Sons, New York, 2nd edition, 1992.

[110] M. Vilfan, V. Rutar, S. Zumer, G. Lahajnar, R. Blinc, J. W. Doane, and A. Golemme. Proton spin-lattice relaxation in nematic microdroplets. *Journal of Chemical Physics*, 89(1):597–604, 1988.

[111] P. G. de Gennes. *Molecular Crystals and Liquid Crystals*, 12:193, 1971.

[112] H. J. Coles. Laser and electric-field induced birefringence studies on cyanobiphenyl homologs. *Molecular Crystals and Liquid Crystals*, 49(3):67–74, 1978.

[113] P.A. Lebwohl and G. Lasher. *Physical Review A*, 6:426, 1972.